ulm university universität ulm

Annual Report 2007

Institute of Optoelectronics

Cover photo:
Semipolar facet LED structure grown on sapphire wafer during electroluminescence test measurements, see the article on p. 67.

Contents

1: Peter Unger
2: Stephan Schwaiger
3: Christine Bunk
4: Fernando Rinaldi
5: Dietmar Wahl
6: Frank Lipski
7: Rainer Blood
8: Ihab Kardosh
9: Rudolf Rösch
10: Jürgen Mähnß
11: Georgi Stareev
12: Josef Theisz
13: Rainer Michalzik
14: Ferdinand Scholz
15: Joachim Hertkorn
16: Andrea Kroner
17: Gerlinde Meixner
18: Hildegard Mack
19: Sarad B. Thapa
20: Abdel-Sattar Gadallah
21: Wolfgang Schwarz
22: Frank Demaria
23: Hendrik Roscher

Missing in the picture:

Karl J. Ebeling, Susanne Menzel, Sükran Kilic, Thomas Wunderer

Institute of Optoelectronics
Ulm University

Albert-Einstein-Allee 45, 89081 Ulm, Germany
URL: http://www-opto.uni-ulm.de
Fax: +49–731/50–2 60 49
Phone: +49–731/50–

Head of Department			
Prof. Dr.	Peter Unger	–2 60 54	peter.unger@uni-ulm.de
Deputy Head			
Prof. Dr.	Ferdinand Scholz	–2 60 52	ferdinand.scholz@uni-ulm.de
President of the University of Ulm			
Prof. Dr.	Karl Joachim Ebeling	–2 60 51	karl.ebeling@uni-ulm.de
Senior Research Assistant			
Dr.-Ing.	Rainer Michalzik	–2 60 48	rainer.michalzik@uni-ulm.de
Cleanroom Management			
Dr.-Ing.	Jürgen Mähnß	–2 60 53	juergen.maehnss@uni-ulm.de
Secretaries			
	Christine Bunk	–2 60 50	christine.bunk@uni-ulm.de
	Sükran Kilic	–2 60 59	suekran.kilic@uni-ulm.de
	Hildegard Mack	–2 60 59	hildegard.mack@uni-ulm.de
Guest Scientist			
Electron. Eng.	Safanov, Ivan M.*	–2 60 39	ivan.safonov@uni-ulm.de
Research Staff			
Dipl.-Ing.	Peter Brückner*	–2 60 35	peter.brueckner@uni-ulm.de
Dipl.-Phys.	Frank Demaria	–2 60 46	frank.demaria@uni-ulm.de
M.Sc.	Abdel-Sattar Gadallah	–2 60 36	abdel-sattar.gadallah@uni-ulm.de
Dipl.-Ing.	Joachim Hertkorn	–2 61 95	joachim.hertkorn@uni-ulm.de
Dipl.-Ing.	Ihab Kardosh	–2 60 36	ihab.kardosh@uni-ulm.de
Dipl.-Ing.	Alexander Kern	–2 60 37	alexander.kern@uni-ulm.de
Dipl.-Ing.	Andrea Kroner	–2 60 38	andrea.kroner@uni-ulm.de
Dipl.-Phys.	Frank Lipski	–2 60 35	frank.lipski@uni-ulm.de
Dr.-Ing.	Steffen Lorch*	–2 60 39	steffen.lorch@uni-ulm.de
Dipl.-Ing.	Michael C. Riedl*	–2 60 36	michael.riedl@uni-ulm.de
Dipl.-Phys.	Fernando Rinaldi	–2 60 46	fernando.rinaldi@uni-ulm.de
Dipl.-Ing.	Hendrik Roscher	–2 60 44	hendrik.roscher@uni-ulm.de
Dipl.-Phys.	Stephan Schwaiger	–2 6056	stephan.schwaiger@uni-ulm.de
Dipl.-Ing.	Wolfgang Schwarz	–2 60 38	wolfgang.schwarz@uni-ulm.de
Dipl.-Ing.	Martin Stach*	–2 60 37	martin.stach@uni-ulm.de
Dr.-Ing.	Georgi Stareev	–2 64 53	georgi.stareev@uni-ulm.de
M.Sc.	Sarad Bahadur Thapa	–2 61 95	sarad.thapa@uni-ulm.de
Dipl.-Phys.	Dietmar Wahl	–2 60 36	dietmar.wahl@uni-ulm.de
Dipl.-Ing.	Thomas Wunderer	–2 64 54	thomas.wunderer@uni-ulm.de

Technical Staff

	Rainer Blood	–2 60 44	`rainer.blood@uni-ulm.de`
	Gerlinde Meixner	–2 60 41	`gerlinde.meixner@uni-ulm.de`
	Susanne Menzel	–2 60 41	`susanne.menzel@uni-ulm.de`
	Josef Theisz	–2 60 30	`josef.theisz@uni-ulm.de`

* Member has left the Institute meanwhile

Preface

The year 2007 was again very fruitful for the Institute of Optoelectronics. Research concentrated on optical interconnect systems, vertical-cavity surface-emitting lasers (VCSELs), GaN-based electronic and optoelectronic devices, and semiconductor disk lasers.

The VCSELs and Optical Interconnects Group has continued to work on novel GaAs-based VCSELs and two-dimensional arrays, new-generation transceiver chips for full-duplex bidirectional optical interconnects, polarization-stable surface grating VCSELs, and VCSEL-based sensing and particle manipulation in microfluidic chips. For the first time, blue light could be generated by intracavity frequency doubling with an efficient electrically pumped VECSEL.

In the GaN Group, much effort has been put into optimization of the electrical properties of nitride-based heterostructures. Besides doping studies of HVPE-grown thick GaN layers, we investigated doping superlattices for improved high-power LEDs and Si doping of AlN for ultra-high band gap electronics. Heteroepitaxial growth studies of GaN on ZnO may eventually lead to novel hetero-nanorod applications. The emission wavelength of our semipolar facet LEDs could be shifted towards the green spectral range.

In the High-Power Semiconductor Laser Group, an optically-pumped semiconductor disk laser with intracavity second-harmonic generation has been realized, emitting 407 mW of continuous output power at a wavelength of 485 nm.

Together with our friends and cooperation partners from the Universities of Regensburg, Stuttgart and Ulm, many members of the Institute joined our hiking workshop in the Söllerhaus (Kleines Walsertal) in October, where the scientific topics presented in short seminar talks were further discussed while climbing some of the local mountains.

Two members of the Institute, namely Philipp Gerlach and Johannes Michael Ostermann, and two external students, namely Tony Albrecht and Michael Furitsch, received their Ph.D. degrees. Furthermore, 10 Diploma or Master Theses and 8 Semester Projects have been carried out in 2007. Thomas Wunderer's Diploma Thesis about electroluminescence of facet quantum wells finished in 2006 was awarded by the VDI Donau-Iller as an outstandingly good Diploma Thesis.

In Oct. 2007, Rainer Michalzik was awarded the Cooperation Prize between Science and Industry of Ulm University together with Johannes Michael Ostermann, Pierluigi Debernardi from the IEIIT National Research Center in Torino, Italy, and U-L-M photonics for the development and commercialization of polarization-stable VCSELs. Many million lasers of this kind are already used in highest performance optical computer mice.

Rainer Michalzik
Ferdinand Scholz
Peter Unger

Ulm, May 2008

Compositional Profile of Graded VCSEL DBRs

Fernando Rinaldi and Dietmar Wahl

The compositional profile of graded distributed Bragg reflectors (DBRs) in vertical-cavity surface-emitting lasers (VCSELs) is investigated. Molecular flux measurements allow to determine small differences between the nominal profile and the epitaxially grown structures. These small differences explain completely the suppression of the higher-order satellites in the HRXRD (high-resolution x-ray diffraction) spectra.

1. Introduction

One of the key components of a VCSEL are the DBRs. The simplest Bragg reflector consists of alternating layers of two semiconductors with different refractive indices. It is known that the electrical resistance is drastically reduced by introducing graded composition layers instead of abrupt interfaces in order to avoid band discontinuities [1]. Although this is necessary for electrically pumped devices, such a layer design considerably increases the complexity of the grown structures. It is in the nature of epitaxial growth processes that small deviations between the nominal and the actually grown structures are present. In case of MBE (molecular beam epitaxy), this is mainly caused by the dynamics of the effusion cells. The aim of this work is the detailed measurement of those deviations and their influences on the HRXRD spectra.

2. Actual Compositional Profile

A detailed plot of the nominal composition profile of a DBR period is given in Fig. 1 for the n-doped side. Starting from the first silicon δ-doping sheet (marked with an arrow), one gallium and two aluminum cells are opened together in order to grow $Al_{0.27}Ga_{0.73}As$. Then the composition is ramped linearly with the thickness until $Al_{0.47}Ga_{0.53}As$ is reached. This is done by increasing the aluminum and decreasing the gallium cell temperatures linearly with time. By shutting all the cells, except the one for silicon, a second δ-doping sheet is obtained. In the same way, a ramp from $Al_{0.47}Ga_{0.53}As$ to $Al_{0.90}Ga_{0.10}As$ is followed by the third δ-doping. When the cells are opened again, their temperature is kept constant and an $Al_{0.90}Ga_{0.10}As$ layer of constant composition is grown. After that, the AlAs/AlGaAs fraction is symmetrically ramped down, but without introducing δ-doping, until an aluminum fraction of 20 percent is reached and kept constant for 37 nm. The cells are then shut for δ-doping and the cycle starts again.

As will be shown in detail in the following, the HRXRD spectra of grown VCSELs show evidence that the compositional profile of the DBRs differs from the nominal one. There

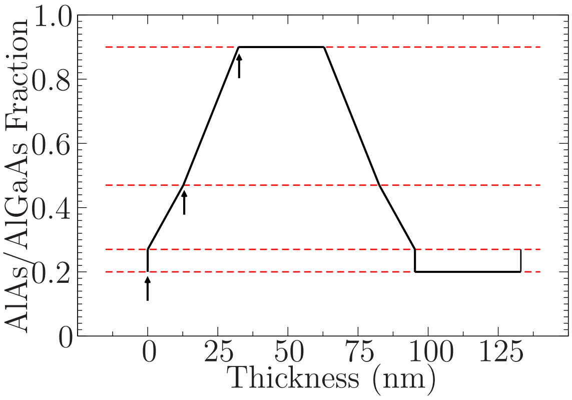

Fig. 1: Nominal compositional profile of a n-doped DBR period in a 850 nm VCSEL. The arrows represent δ-doping. Four linearly graded layers per period are present.

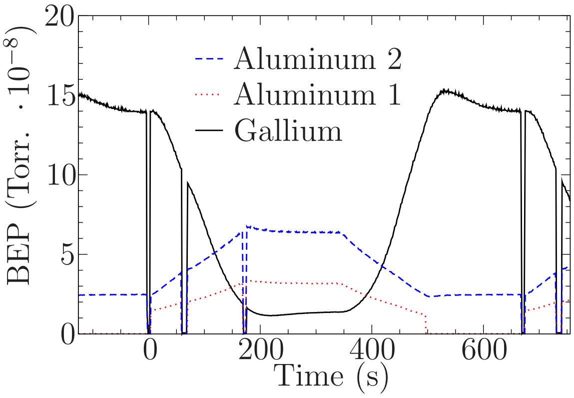

Fig. 2: Measured fluxes from the three effusion cells used to grow the nominal structure shown in Fig 1. One DBR period is grown in approximately 670 s.

are several causes for this behavior, considering that during the ramps, the cells are programmed to change their temperature linearly with time. In fact, the fluxes are not linear functions of the temperature, and the effusion cells have a certain response time and a specific dynamic behavior.

One has to mention that in the VCSEL design, there is no particular reason to choose linearly graded profiles, and so there is also no reason to try to correct the real compositional profile in order to better match the one shown in Fig. 1. In fact, the specific profile influences the maximum reflectivity and the width of the stop-band, which is always present as long as the periodicity of the structure is maintained. Small deviations of the profile do not affect the optical reflectivity spectrum significantly. It follows that one can accidentally grow graded DBRs with high reflectivity at the design wavelength using wrong growth rates for the different cells. But this can cause unintentional detuning of the laser cavity or affect other features of the structure.

Precise data of the profile can be obtained by measuring the fluxes of each effusion cell involved in the growth process when these are driven in the same way as during growth. For these measurements, a Bayard–Alpert ionization gauge [2] was located at the substrate position. The growth rate, that is proportional to the measured beam equivalent pressure (BEP), can be acquired as a function of time for each cell separately. The resulting fluxes from the gallium and the two aluminum cells were successively measured. The data, expressed in BEP, are plotted in Fig. 2, where one can recognize the occurrence of the three δ-doping sheets, when all the cells are shut and the BEPs drop to zero. Those flux drops can be used to synchronize the three data sets and display them in the diagram according to the growth recipe. To achieve the desired grading of the aluminum concentration, the gallium flux increases while the aluminum fluxes decrease and vice versa. Unlike the aluminum cells, the gallium cell shows a big flux overshoot approximately 530 s after the period has started. This proves that relevant effects are arising from the response of the cells to the transients. Using the calibration table, it is possible to convert the fluxes into growth rates. The AlAs/AlGaAs fraction c as a function of time is given by

$$c(t) = \frac{G_{\mathrm{Al1}}(t) + G_{\mathrm{Al2}}(t)}{G_{\mathrm{Al1}}(t) + G_{\mathrm{Al2}}(t) + G_{\mathrm{Ga}}(t)}\,, \tag{1}$$

where $G(t)$ represent the growth rates of AlAs or GaAs as a function of time for a specific cell. Integrating the total growth rate over time, one gets the grown thickness d at a specific time t as

$$d(t) = \int_0^t (G_{\mathrm{Al1}}(t') + G_{\mathrm{Al2}}(t') + G_{\mathrm{Ga}}(t'))\,\mathrm{d}t'\ . \tag{2}$$

Eliminating t from (1) and (2), one gets the compositional profile $c(d)$, which is shown in Fig. 3 in comparison with the nominal one. The $c(d)$ measured for four periods are shown in Fig. 4, where the layer reproducibility and so the periodicity of the DBR are strictly confirmed. A simplified sample made of 34 n-doped periods was grown to analyze the periodic structure in detail. The HRXRD spectra are shown in Fig. 6. One can see that the simulation based on the linearly graded compositional profile shows high-order satellite peaks that are not present in the measurements. From the kinematical theory of scattering, the satellite peaks are related to the Fourier components of the electron density of the periodic superlattice; they represent its structure factor. The suppression of the satellites is caused by the smoother profile. Despite almost all VCSELs have graded composition profiles to reduce the electrical resistance, the HRXRD spectra of the DBRs are seldom analyzed in literature. The problem is marginally treated in [3] and in more detail in [4], where the idea to mimic smooth profiles by a biparabolic function is introduced.

The biparabolic profile is defined as

$$c(x) = c_1 + \frac{(c_2 - c_1)(x - d_1)^2}{(d_2 - d_1)^2} \qquad \text{for} \qquad d_1 \le x \le d_2 \tag{3}$$

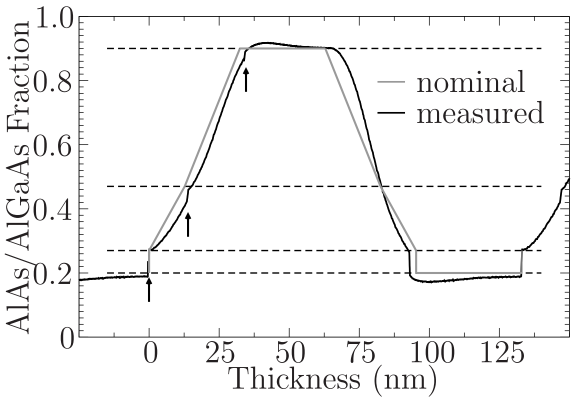

Fig. 3: Comparison between the nominal and measured compositional profiles in a 850 nm VCSEL DBR period. The arrows represent δ-doping. The experimental profile is obtained by flux measurements.

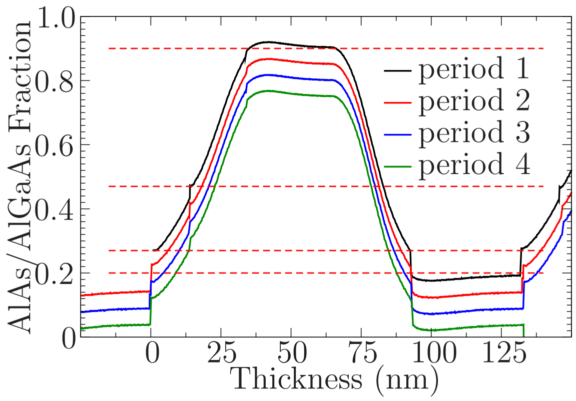

Fig. 4: Comparison between the profiles of four adjacent DBR periods obtained from flux measurements. For clarity, the profiles are shifted by 5 % each.

and

$$c(x) = c_3 + \frac{(c_2 - c_3)(x - d_3)^2}{(d_3 - d_2)^2} \qquad \text{for} \qquad d_2 \le x \le d_3 \ , \tag{4}$$

where the indices 1 and 3 refer to the starting and final points, respectively, and the index 2 refers to the junction point of the two parabolas, as can be seen in Fig. 5. The continuity of the profile is directly given by (3) and (4), and six parameters are necessary to define the curve. The continuity of the first derivative reduces the free parameters to five and requires

$$\frac{c_3 - c_2}{d_3 - d_2} = \frac{c_2 - c_1}{d_2 - d_1} \ . \tag{5}$$

In Figs. 6, 7, and 8, the measured and simulated HRXRD spectra for the test sample and for a complete VCSEL structure are plotted. In both cases one can see that the linearly graded nominal profile is not adequate to fit the spectra. From Fig. 1, it is inferred that, because of its symmetry, 8 parameters are needed to fit the nominal profile. Using a biparabolic profile, like in Fig. 5, also 8 parameters are needed to fit the complete profile, which is also considered symmetric. In fact, condition (5) was not used here. The comparisons in Figs. 7 and 8 indicate that at least 15 lamellae are needed for a satisfactory fit. As seen in Fig. 5, a good approximation of the measured profile is then obtained.

It is important to point out that it is impractical to obtain the compositional profile by flux measurements before the growth of each sample. As shown, this can be extracted by HRXRD, giving precise information that can be used for the next growth run.

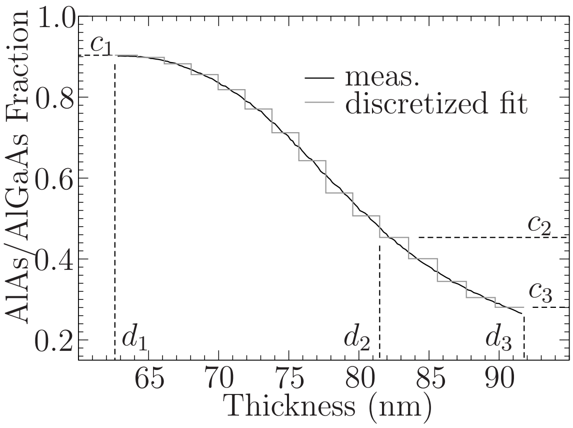

Fig. 5: Discretized biparabolic composition profile used to fit the VCSEL spectra in Figs. 7 and 8, as well as the profile obtained by flux measurements. The number of used lamellae is 15.

3. Acknowledgement

We thank Shunyi Li for his help with the HRXRD measurements and the spectra fits using a commercial x-ray diffraction dynamic theory simulation tool.

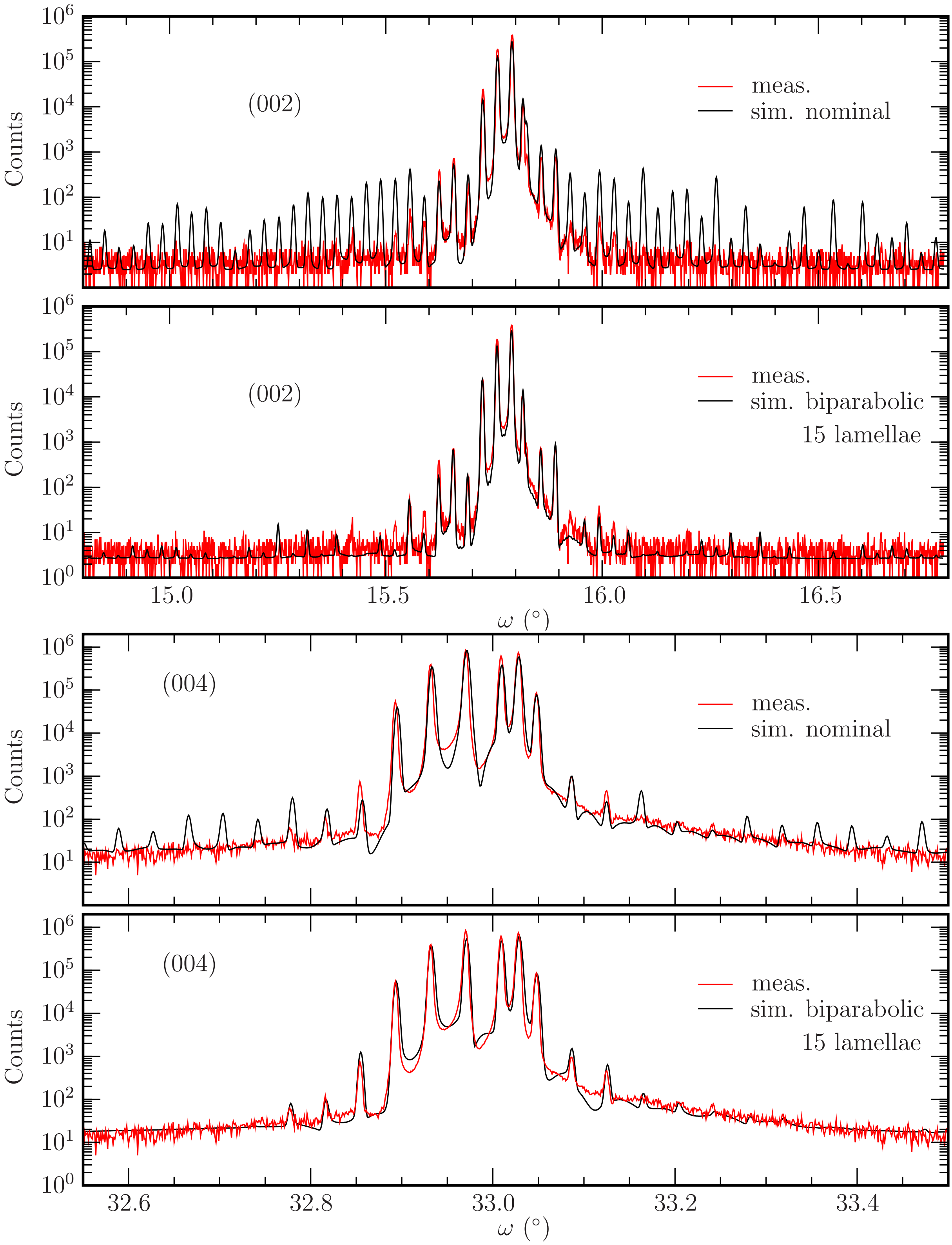

Fig. 6: HRXRD (002) and (004) spectra of the 34 periods n-doped DBR. The corresponding simulations are made both with nominal (linearly graded) and discretized biparabolic profiles.

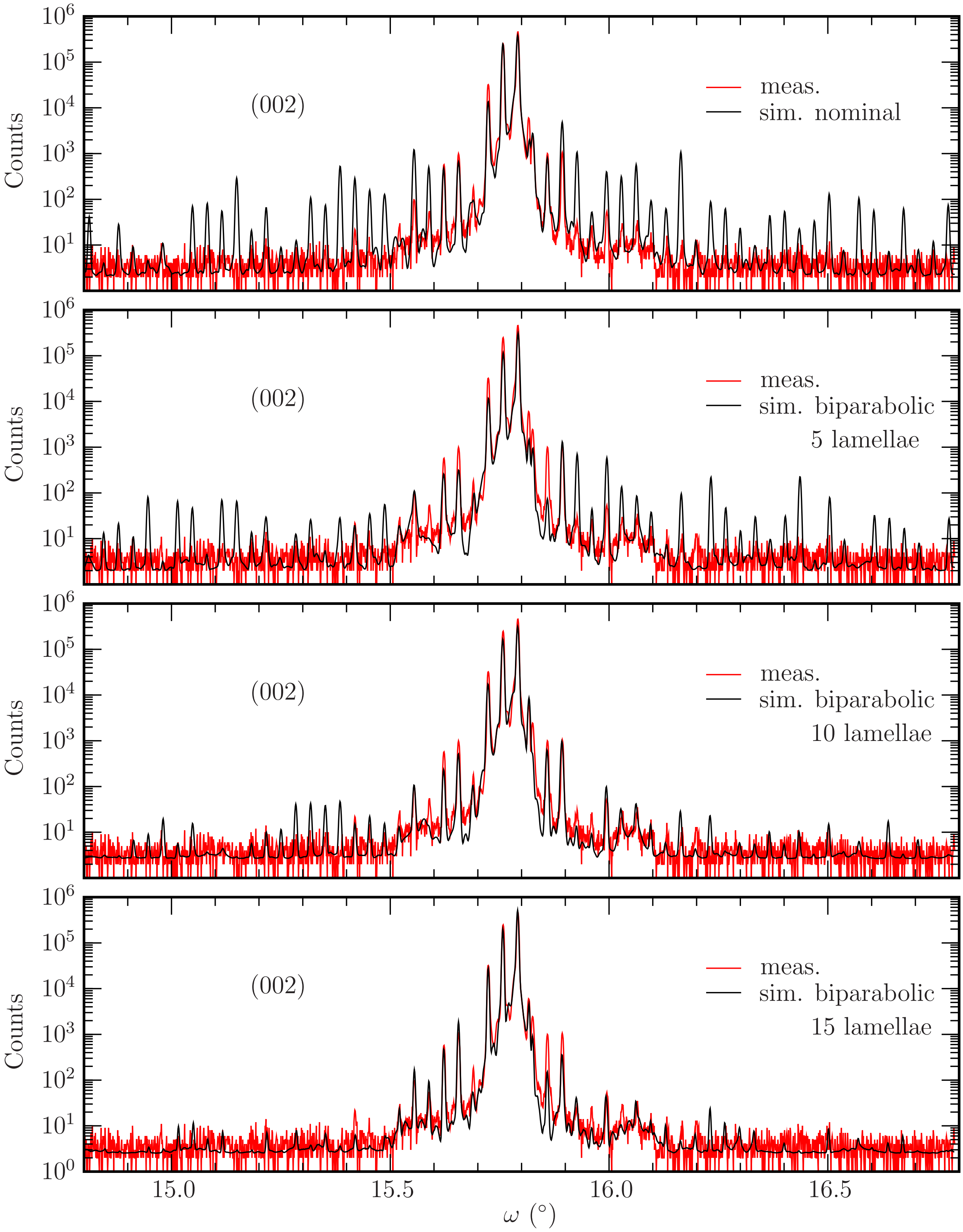

Fig. 7: HRXRD (002) spectra of a complete 850 nm VCSEL structure. The corresponding simulations use nominal (linearly graded) and biparabolic profiles with 5, 10, and 15 lamellae.

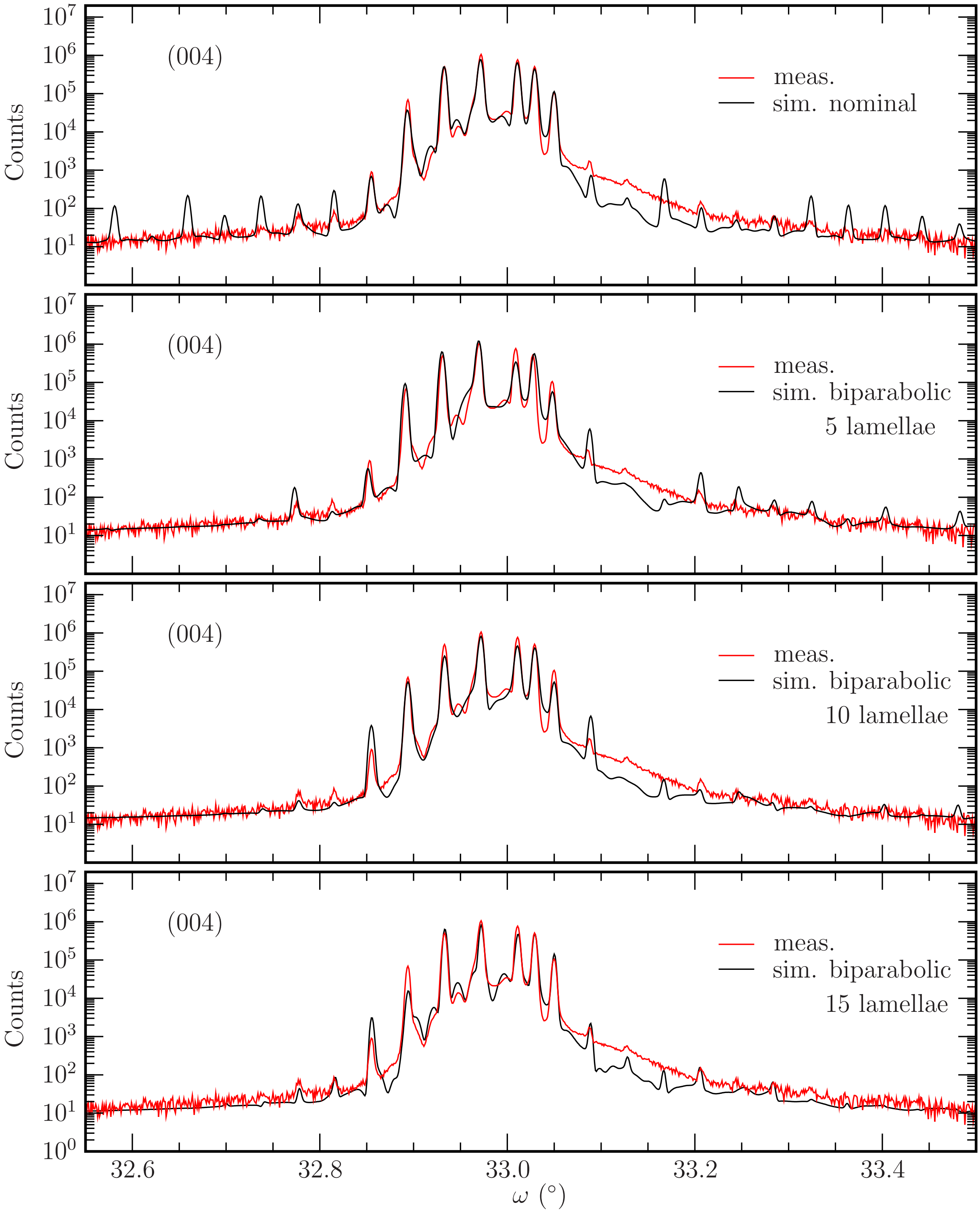

Fig. 8: Same as Fig. 7, here referring to the HRXRD (004) reflection.

References

[1] K. Tai, L. Yang, Y.H. Wang, J.D. Wynn, and A.Y. Cho, "Drastic reduction of series resistance in doped semiconductor distributed Bragg reflectors for surface-emitting lasers", *Appl. Phys. Lett.*, vol. 56, pp. 2496–2498, 1990.

[2] R.K. Fitch, "Total pressure gauges", *Vacuum*, vol. 37, pp. 637–641, 1987.

[3] P. Kidd, "Investigation of the precision in x-ray diffraction analysis of VCSEL structures", *J. Mat. Sci.: Mat. Electron.*, vol. 14, pp. 541–550, 2003.

[4] S.G. Patterson, G.S. Petrich, R.J. Ram, and L.A. Kolodziejski, "X-ray diffraction analysis of bandgap-engineered distributed Bragg reflectors", *J. Electron. Mat.*, vol. 28, pp. 1081–1083, 1999.

Sensitivity of Surface Grating VCSELs to Externally Induced Anisotropic Strain

Johannes Michael Ostermann, Pierluigi Debernardi†, and Andrea Kroner

Linearly polerized surface grating vertical-cavity surface-emitting lasers (VCSELs) are exposed to externally applied anisotropic stress. Their behavior is compared to that of a nominally identical standard VCSEL without a surface grating. The VCSEL chips are bent in a well-defined way. The induced anisotropic in-plane strain leads to a polarization switch of the standard VCSEL for rather moderate strain. In contrast, the polarization of the surface grating VCSELs is fixed by the grating and remains unchanged despite a high strain which causes a wavelength splitting of the two polarization modes of about 130 pm. Such result is of high practical relevance, since strain is unavoidably induced during VCSEL fabrication and mounting and counteracts any method applied for polarization control.

1. Introduction

The influence of strain on the polarization properties of standard VCSELs has been studied in detail [1–5]. Since strain is linked to the complex refractive indices of the different layers inside a VCSEL structure through the strain-optic tensor, it influences the polarization properties of VCSELs via the elasto-optic effect. A modified imaginary part of the complex refractive indices alters gain and absorption and a modified real part causes birefringence in addition to the birefringence already present in VCSELs due to the electro-optic effect [6]. Frequently, the consequence of strain is thus a polarization switch.

Strain in VCSELs can result either from a mismatch of the lattice constants of two layers or from defects introduced during growth and processing. It can also be caused by unintentional stress applied during the mounting and bonding processes. Even if a VCSEL is polarization-stable when tested on wafer, the strain induced during mounting and bonding can be such that the VCSEL exhibits a polarization switch afterwards. Strain can also be induced intentionally to study the polarization properties. This was done by focusing a laser beam to a small spot close to a VCSEL to create a localized heat source [1] or permanent crystal defects [2]. Alternatively, strain in VCSELs can be caused by bending a VCSEL chip mechanically [3].

In recent years, surface gratings have proven to control the polarization of VCSELs very reliably [7, 8]. In this paper, we study whether the polarization control resulting from a surface grating is strong enough to guarantee a stable polarization even under severe externally applied stress.

†Pierluigi Debernardi is with the IEIIT-CNR c/o Politecnico di Torino, Torino, Italy

2. Measurement Setup

The setup used for the investigations is shown in Fig. 1. Similar to [3] it is based on a mechanical deflection of the VCSEL chip, which is placed on a baseplate with an edge. The sample is clamped with a plate and a screw on one side. A seesaw driven by a micrometer screw on the other side of the sample bends the sample over the edge in the baseplate. The width of the seesaw exceeds the width of the sample to introduce a uniform strain along the direction defined by the edge. All three VCSELs investigated in the paper are located along one row parallel to the $[\bar{1}10]$ crystal axis on the sample. Consequently, they can be aligned simultaneously along the edge of the baseplate, so that the strain induced along the [110] crystal axis is the same in all three VCSELs, although its magnitude is not exactly known. The value Δx stated in the following is the deflection of the seesaw on the side of the sample in a distance of about 6 mm from the edge in the baseplate, as indicated in Fig. 1. However, the amount of strain is not directly proportional to Δx, since the zero point was chosen such that the seesaw does not touch the sample and thus does not induce any strain for $\Delta x = 0$.

To allow a rough estimation of the strain introduced in the VCSELs through the bending and to make the experiments comparable to others reported in the literature [3–5], polarization-resolved spectra are recorded close to threshold to measure the wavelength splitting between the two polarization modes for different deflections.

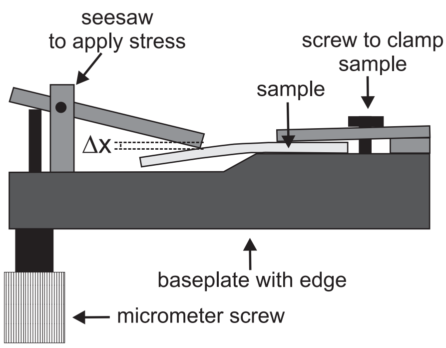

Fig. 1: Schematic drawing of the sample holder used for the investigations of the polarization properties of VCSELs under externally applied stress.

3. Investigated VCSELs

All three VCSELs investigated in this paper are on the same sample with a wafer thickness of 350 µm. They are nominally identical except for the different surface modifications. Their wavelengths vary slightly around 915 nm due to a variation of the thickness of the epitaxial layers over the sample. All three VCSELs have an active diameter of about 4 µm. The two grating VCSELs are adjacent to each other, separated by only 250 µm. Their surface gratings have orthogonal orientations, a period of 0.8 µm, and a depth of 57 nm. The outer diameter of the grating is limited to 3.6 µm to form a grating relief to achieve higher single-mode output powers [7, 9, 10]. The area outside the relief is etched to the same depth as the grating grooves. The mirror reflectivity outside the relief is consequently strongly reduced, which suppresses higher-order transverse modes. Therefore, the grating relief VCSELs are single-mode up to thermal rollover, while higher-order modes start to lase in the standard VCSEL at a current of about three times the threshold current. However, the grating relief causes an overall reduced mirror reflectivity, which explains the higher threshold current of the grating VCSELs compared to the standard VCSEL.

4. Standard VCSEL With Externally Induced Strain

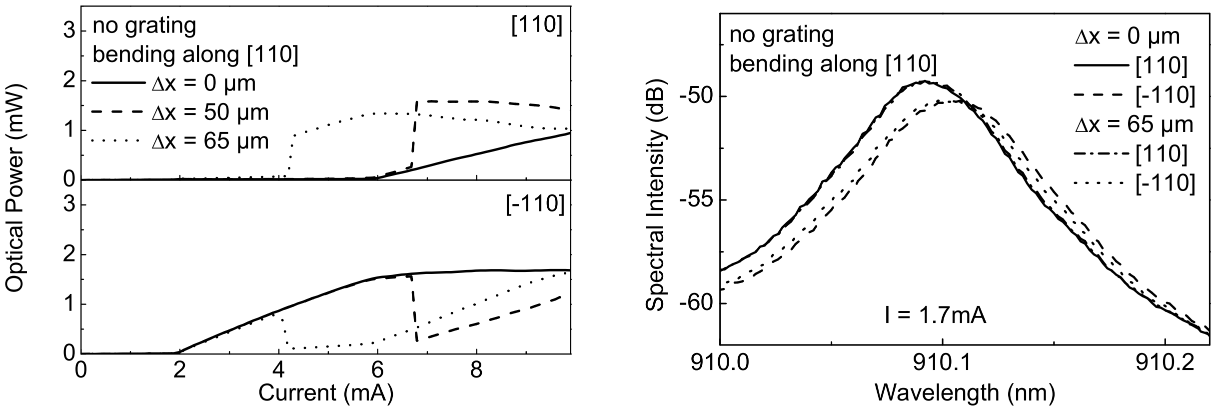

Fig. 2: PR-LI characteristics (left) and polarization-resolved spectra (right) of a standard VCSEL with an active diameter of 4 μm under varying externally applied stress.

Without strain, the fundamental mode of the standard VCSEL is polarized along the $[\bar{1}10]$ crystal axis, while the first higher-order mode, which starts to lase at around 5.8 mA, is polarized along the [110] crystal axis, as can be seen from the polarization-resolved light–current (PR-LI) characteristics of this VCSEL shown in the left graph of Fig. 2. However, the fundamental mode of the standard VCSEL and also the higher-order mode exhibit a polarization switch as soon as the sample is bent over the edge of the baseplate. The strain that causes such polarization switches is quite small, since it does not even change the emission wavelengths of the two polarization modes significantly, which is concluded from the polarization-resolved spectra in the right graph of Fig. 2. The current at which the polarization switch occurs is decreasing with increasing bending. These measurements are just intended to illustrate the influence of the externally introduced strain on the polarization properties of standard VCSELs, since similar results were found before by other researchers [3–5]. Here, they serve to quantitatively illustrate the different behaviors of a standard VCSEL and surface grating VCSELs.

5. Surface Grating VCSELs With Externally Induced Strain

In this section we repeat the experiments from Sect. 4 while using grating VCSELs. The grating grooves of the VCSEL in the left (right) graph of Figs. 3 and 4 are oriented along the [110] ($[\bar{1}10]$) crystal axis. Since both grating VCSELs are polarized parallel to

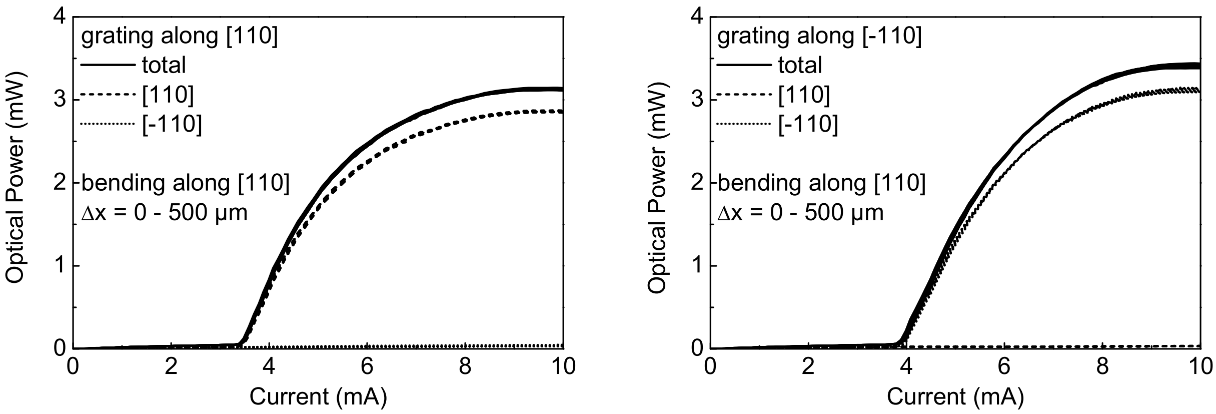

Fig. 3: PR-LI characteristics of grating VCSELs with their grating grooves oriented along the [110] crystal axis (left) and the $[\bar{1}10]$ axis (right) under varying externally applied stress. The bending Δx of the sample is varied between 0 and 500 µm in steps of 50 µm. VCSEL parameters are described in Sect. 3.

their grating grooves without externally induced strain (see Fig. 3), they are orthogonally polarized with respect to each other. Consequently, the polarization of one of the two VCSELs is destabilized by the externally applied stress along the [110] crystal axis independent of whether the bending favors the mode parallel or orthogonal to the bending direction. However, even for a deflection exceeding the one causing a polarization switch in the standard VCSEL by a factor of ten, the LI characteristics of the grating VCSELs remain unchanged. Therefore the eleven curves for different bendings are almost indistinguishable in Fig. 3.

The polarization-resolved spectra of the [110]-oriented grating VCSEL in Fig. 4 (left), which are recorded close to threshold, show a birefringence of -20 pm (peak spectral positions of 920.78 and 920.80 nm for the [110] and $[\bar{1}10]$ directions, respectively) without bending. It results from a combination of the electro-optic effect and the birefringence induced by the grating itself. For a deflection of $\Delta x = 500\,\mu$m, this value has changed to $+100$ pm (peaks at 920.85 and 920.75 nm for the [110] and $[\bar{1}10]$ directions, respectively) owing to the contribution from the elasto-optic effect. Thus the emission wavelengths of the two polarization modes experience a relative shift of about 120 pm due to the induced strain.

In case of the $[\bar{1}10]$-oriented grating VCSEL in Fig. 4 (right), the birefringence changes from $+10$ pm to $+140$ pm for the same amount of bending, corresponding to a relative shift of 130 pm, which is very similar to that in the neighboring device. The observed wavelength shifts indicate an induced maximum strain level comparable to those reported in [3–5]. In all three previous studies using standard VCSELs without a surface grating, such strain causes a change of the polarization orientation by 90°. In contrast, the grating VCSELs remain polarization-stable.

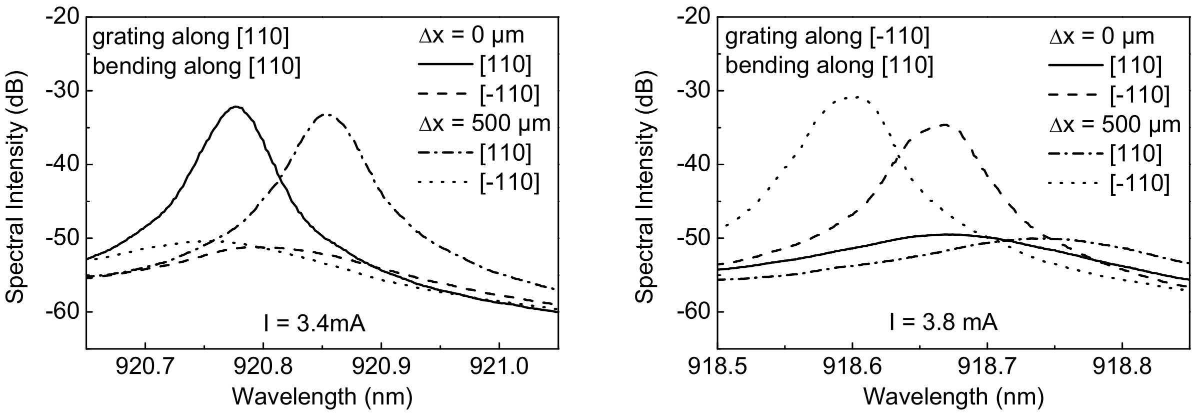

Fig. 4: Polarization-resolved spectra of the grating VCSELs from Fig. 3 close to threshold for the two extreme values of deflection Δx.

6. Conclusion

We have shown that surface gratings are able to control the polarization of VCSELs even for strong externally induced anisotropic in-plane strain, while a nominally identical standard VCSEL exhibits a polarization switch already for a fraction of this strain. The splitting of about 130 pm between the wavelengths of the polarization modes of the grating VCSELs, induced by the applied stress, is fully comparable to the ones reported in the literature [3–5], which inevitably caused polarization switches. This proves the high degree of reliability of the polarization control obtained by means of surface gratings. One can conclude from the measurements presented here that the polarization control of surface gratings is strong enough to outbalance the influence of any strain typically introduced during the fabrication process of VCSELs. To the best of our knowledge, this is the first successful study of VCSEL polarization control under strain conditions.

7. Acknowledgment

The authors would like to acknowledge the help of Matthias Golling, Christof Jalics, and Yakiv Men in the fabrication of the sample and the fruitful discussions with Markus Sondermann. Ulm University gratefully acknowledges the partial funding of this work by the German Research Foundation (DFG).

References

[1] A.K. Jansen van Doorn, M.P. van Exter, and J.P. Woerdman, "Elasto-optic anisotropy and polarization orientation of vertical-cavity surface-emitting semiconductor lasers", *Appl. Phys. Lett.*, vol. 69, pp. 1041–1043, 1996.

[2] A.K. Jansen van Doorn, M.P. van Exter, and J.P. Woerdman, "Tailoring the birefringence in a vertical-cavity semiconductor laser", *Appl. Phys. Lett.*, vol. 69, pp. 3635–3637, 1996.

[3] K. Panajotov, B. Nagler, G. Verschaffelt, A. Georgievski, H. Thienpont, J. Danckaert, and I. Veretennicoff, “Impact of in-plane anisotropic strain on the polarization behavior of vertical-cavity surface-emitting lasers”, *Appl. Phys. Lett.*, vol. 77, pp. 1590–1592, 2000.

[4] M. Peeters, K. Panajotov, G. Verschaffelt, B. Nagler, J. Albert, H. Thienpont, I. Veretennicoff, and J. Danckaert, “Polarisation behavior of vertical-cavity surface-emitting lasers under the influence of in-plane anisotropic strain”, in *Vertical-Cavity Surface-Emitting Lasers VI*, C. Lei and S.P. Kilcoyne (Eds.), Proc. SPIE 4649, pp. 281–291, 2002.

[5] G. Van der Sande, M. Peeters, I. Veretennicoff, J. Danckaert, G. Verschaffelt, and S. Balle, “The effects of stress, temperature, and spin flips on polarization switching in vertical-cavity surface-emitting lasers”, *IEEE J. Quantum Electron.*, vol. 42, pp. 898–906, 2006.

[6] M.P. van Exter, A.K. Jansen van Doorn, and J.P. Woerdman, “Electro-optic effect and birefringence in semiconductor vertical-cavity lasers”, *Phys. Rev. A*, vol. 56, pp. 845–853, 1997.

[7] J.M. Ostermann, P. Debernardi, C. Jalics, A. Kroner, M.C. Riedl, and R. Michalzik, “Surface gratings for polarization control of single- and multi-mode oxide-confined vertical-cavity surface-emitting lasers”, *Optics Communications*, vol. 246, pp. 511–519, 2005.

[8] P. Debernardi, J.M. Ostermann, M. Feneberg, C. Jalics, and R. Michalzik, “Reliable polarization control of VCSELs through monolithically integrated surface gratings: a comparative theoretical and experimental study”, *IEEE J. Select. Topics Quantum Electron.*, vol. 11, pp. 107–116, 2005.

[9] P. Debernardi and G.P. Bava, “Coupled mode theory: a powerful tool for analyzing complex VCSELs and designing advanced device features”, *IEEE J. Select. Topics Quantum Electron.*, vol. 9, pp. 905–917, 2003.

[10] J.M. Ostermann, P. Debernardi, C. Jalics, and R. Michalzik, “Polarization-stable oxide-confined VCSELs with enhanced single-mode output power via monolithically integrated inverted grating reliefs”, *IEEE J. Select. Topics Quantum Electron.*, vol. 11, pp. 982–989, 2005.

Analysis of Higher-Order Mode Selection in Rectangular-Shaped VCSELs

A. Gadallah and A. Kroner

We report on the theoretical analysis of a novel type of vertical-cavity surface-emitting laser (VCSEL) that provides selection of a certain higher-order transverse mode. This selection is based on a spatial variation of the threshold gain by adding an antiphase layer with an etched relief structure. The field intensity profile emitted from this laser is calculated numerically as well as with an analytical approach. The main factors that control the selected mode such as the threshold gain, the confinement factor, and the phase parameter are calculated as a function of the active aperture, aiming to achieve single higher-order transverse mode emission. For a given aspect ratio of a rectangular oxide aperture, the threshold gain difference between the selected and neighboring modes is maximized via the relief diameter and the size of the aperture.

1. Introduction

VCSELs have attracted considerable interest due to their low divergence and nonastigmatic beam characteristics as well as low-cost manufacturing, testing and packaging. Besides, the ability of single-mode operation in longitudinal and transverse directions is one of the most distinguished advantages of these lasers. Single-mode VCSELs offer different applications ranging from data transmission to optical sensing [1], [2]. While single-longitudinal mode operation is inherent to the short cavity design of VCSELs, the transverse mode behavior depends on the size of the active aperture as well as the layer structure. To select the fundamental mode, the active aperture of the VCSEL has to be small. This deteriorates the performance of the device by increasing both the thermal resistance and the ohmic series resistance. Moreover, the device lifetime is decreased and mass production is made more difficult due to tight aperture tolerances.

In this report, we introduce a theoretical analysis of VCSELs with rectangular-shaped apertures that allow operation on a certain higher-order transverse mode. The larger aperture size of this VCSEL offers low series resistances as well as potentially increased lifetimes. Another interest of operation on a higher-order transverse mode is in multiple optical trapping [3] and potentially in optical data storage [4].

2. Description of the Device and Theoretical Basics

A schematic drawing of a VCSEL with an etched surface relief is shown in Fig. 1. The layer structure consists of 23 C-doped GaAs/AlGaAs p-distributed Bragg reflector (DBR)

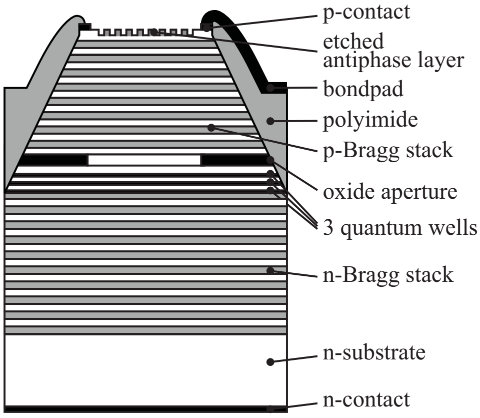

Fig. 1: Schematic representation of a surface-structured VCSEL.

pairs as top mirror (plus the topmost GaAs quarter-wave layer), 38.5 Si-doped n-DBR pairs as the bottom mirror, and three 8 nm thick GaAs quantum wells for laser emission around 850 nm wavelength. The shallow surface relief [1] is utilized to allow operation on a certain higher-order transverse mode. There are two main differences between this specially designed VCSEL and a standard one. Firstly, concerning the layer structure, a quarter-wavelength antiphase layer is added in order to induce a decrease in top mirror reflectivity. This layer is then selectively removed by means of wet-chemical etching. The second point concerns the shape of the mesa and thus of the oxide aperture. It is no longer of circular shape, instead it is rectangular, where one side of the rectangle is much longer than the other. Current confinement is achieved through thermal oxidation of an AlAs layer placed just above the one-wavelength thick inner cavity. Wet etching is used to reach this layer. N- and p- type metalization processes are applied, followed by polyimide passivation. Finally, bondpad metalization is carried out for electrical contacting. In order to investigate the modes that can be excited in such VCSELs, we introduce two different approaches. The first one is based on solving the Helmholtz equation numerically and the second is an analytical solution using the Marcatili approach [5]. For solving the Helmholtz equation numerically, we assume a rectangular core of refractive index n_1, which corresponds to the non-oxidized cross-sectional area of the cavity, is immersed in a cladding layer of refractive index $n_2 < n_1$ [6]. The indices n_1 and n_2 are interpreted as average quantaties in the longitudinal cavity direction. The index difference $\Delta n = n_1 - n_2$ is related to the cavity resonance shift $\Delta\lambda_{\mathrm{ox}}$ as [7]

$$\Delta n = n_1 \Delta\lambda_{\mathrm{ox}}/\lambda \ , \tag{1}$$

where λ is the lasing wavelength. The parameter $\Delta\lambda_{\mathrm{ox}}$ is easily determined from two calculations with the transfer matrix method [7] as the difference in resonance wavelengths in the non-oxidized and oxidized parts of the cavity. With known indices n_1 and n_2, we then numerically solve the Helmholtz equation in the transverse plane while applying the Dirichlet boundary conditions, i.e., the electric field diminishes at the boundary of the calculation window. The result is a usually large number of guided transverse modes. In order to solve the problem analytically and obtain the modes, we refer to Fig. 2, where the active aperture of refractive index n_1 is surrounded by a lower refractive index $n_2 =$

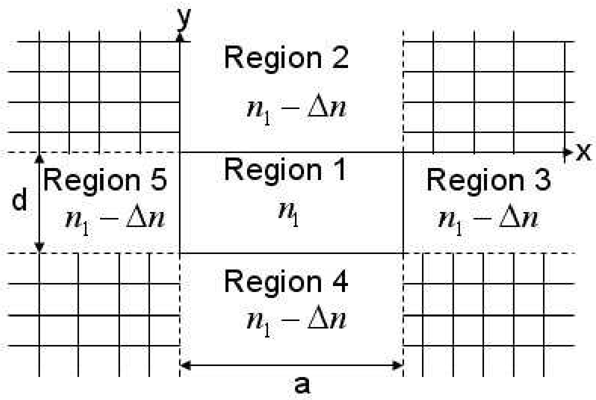

Fig. 2: Approximation of the active aperture of a rectangular-shaped VCSEL with refractive index n_1 surrounded by a lower refractive index medium $n_2 = n_1 - \Delta n$.

$n_1 - \Delta n$, and the fields in the corner regions are neglected according to the Marcatili approximation. The transverse components of the electric or magnetic fields have to satisfy the reduced wave equation

$$\partial^2\psi/\partial x^2 + \partial^2\psi/\partial y^2 + (n_m^2 k^2 - \beta^2)\psi = 0 \ , \tag{2}$$

where ψ is either E_x, E_y, H_x, or H_y and n_m is the refractive index in region m. The propagation constant is $\beta = kn_{\text{eff}}$ with the wavenumber $k = 2\pi/\lambda$ and the effective refractive index in the longitudinal direction n_{eff}. There are two types of modes that such a structure can support, namely E^y_{pq} and E^x_{pq}, where the integers p, q stand for the number of extrema in x- and y-directions, respectively. E^y_{pq} modes are predominantly polarized in y-direction and consist mainly of E_y and H_x. Correspondingly, E^x_{pq} modes are mainly x-polarized with dominant E_x and H_y. The field components E_y and H_x of the modes E^y_{pq} that satisfy (2) in the m-th region in Fig. 2 are given by ([8], p. 49)

$$E_{ym}(x,y) = H_{xm}(x,y) \cdot \begin{cases} (n_1^2k^2 - k_y^2)/(\omega\epsilon_0 n_1^2\beta) & \text{for} \quad m = 1, \\ (n_2^2k^2 - k_{y2}^2)/(\omega\epsilon_0 n_2^2\beta) & \text{for} \quad m = 2, \\ (n_2^2k^2 - k_y^2)/(\omega\epsilon_0 n_2^2\beta) & \text{for} \quad m = 3, \\ (n_2^2k^2 - k_{y2}^2)/(\omega\epsilon_0 n_2^2\beta) & \text{for} \quad m = 4, \\ (n_2^2k^2 - k_y^2)/(\omega\epsilon_0 n_2^2\beta) & \text{for} \quad m = 5 \end{cases} \tag{3}$$

and

$$H_{xm}(x,y) = \begin{cases} M_1 \cos(k_x x + \alpha)\cos(k_y y + \varphi) & \text{for } m = 1, \\ M_2 \cos(k_x x + \alpha)\exp(-\mathrm{i}k_{y2}y) & \text{for } m = 2, \\ M_3 \cos(k_y y + \varphi)\exp(-\mathrm{i}k_{x3}x) & \text{for } m = 3, \\ M_4 \cos(k_x x + \alpha)\exp(\mathrm{i}k_{y2}y) & \text{for } m = 4, \\ M_5 \cos(k_y y + \varphi)\exp(\mathrm{i}k_{x3}x + \gamma) & \text{for } m = 5, \end{cases} \tag{4}$$

where the refractive index and the propagation constant in region m are related by

$$k_{xm}^2 + k_{ym}^2 + \beta^2 = n_m^2 k^2 \ . \tag{5}$$

M_m are the field amplitudes, ω is the angular frequency, and ϵ_0 is the permittivity in free space. The angles α, φ locate the field maxima and minima in region 1, and γ equals to

0° or 90°. For matching the fields at the boundaries between region 1 and regions 2 and 4, we have assumed in (3), (4) that

$$k_{x1} = k_{x2} = k_{x4} = k_x \tag{6}$$

and similarly

$$k_{y1} = k_{y3} = k_{y5} = k_y \tag{7}$$

to match the fields between regions 1, 3, and 5. From (3) and (4), the field in region 1 is sinusoidal and decays exponentially in the other regions. Some of the guided transverse

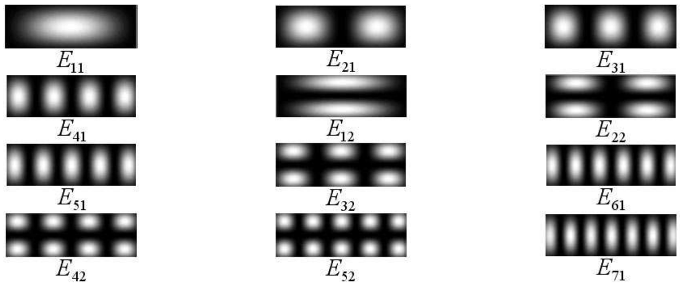

Fig. 3: Intensity profiles of the several guided modes and their designations in a VCSEL with $a = 3d = 30\,\mu m$, $\lambda = 850\,nm$, $n_1 = 3.3$, and $\Delta n = 2 \cdot 10^{-3}$.

modes of such a structure with their mode designations are illustrated in Fig. 3. The corresponding BV diagrams of such a structure generated from the analytical and the numerical solutions for an aspect ratio of 3 are shown in Fig. 4, respectively. The frequency parameter V and the phase parameter B are defined as

$$V = (2\pi/\lambda) d \sqrt{n_1^2 - n_2^2}\ , \tag{8}$$

$$B = (n_{\text{eff}}^2 - n_2^2)/(n_1^2 - n_2^2)\ , \tag{9}$$

where d is the aperture width. From Fig. 4 it is seen that even the fundamental mode E_{11} has a cut-off frequency. Furthermore, the cut-off frequencies of the numerical solutions are smaller than the analytical solutions. As the aspect ratio increases from 3 to 10, the separation between modes on the V-axis decreases, as shown in Fig. 5. In addition, the order of appearance of the modes changes as the aspect ratio changes. The BV diagram for circular aperture VCSELs with the same structure is displayed in Fig. 6. In this case, the parameter d in (8) is identified with the *radius* of the oxide aperture to be consistent with the literature on optical fiber theory. The number of guided modes is low due to the fact that the aspect ratio is equal to one. It is plotted in Fig. 6 (right) as a function of the aperture area. In order to select the oscillation of a certain mode in this VCSEL, for example the mode E_{81}, a shallow one-dimensional relief with 8 circular spots is etched through the entire antiphase layer, such that the centers of the spots coincide with the positions of the extrema of the field profile. Here we assume that the relief does not perturb the field. The selection of the lasing mode of such a structure depends on the confinement factors Γ of the modes and the threshold gains, where

$$\Gamma = P_{\text{p}}/P_{\text{t}} \tag{10}$$

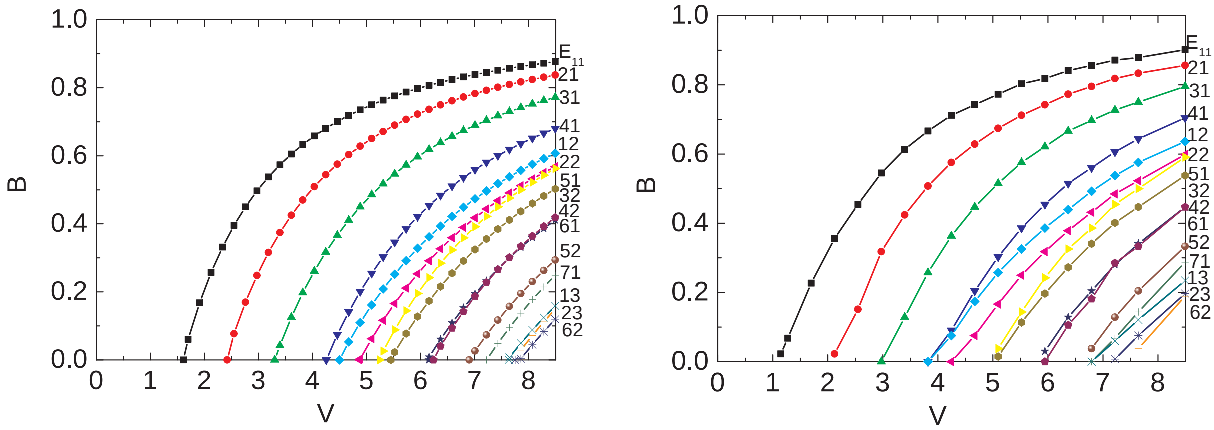

Fig. 4: BV diagram of rectangular-shaped VCSELs obtained from analytical solutions (left) and numerical solutions (right). The aspect ratio is 3.

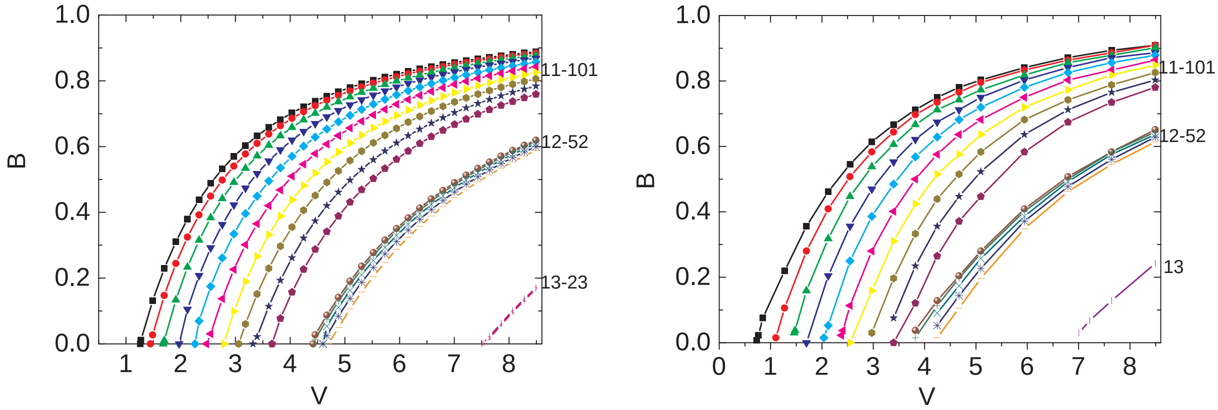

Fig. 5: BV diagram equivalent to Fig.4 for an aspect ratio of 10.

with P_p and P_t as the power in area of the etch pattern and the total power of the mode, respectively. The corresponding threshold gain of the mode depends on this confinement factor as well as on the threshold gains inside and outside the spot area, namely g_in and g_out, respectively, where $g_\mathrm{in} < g_\mathrm{out}$. These threshold gains are calculated for the given structure using the transfer matrix method [7]. The threshold gain of the particular mode is then given by

$$g_\mathrm{th} = \Gamma g_\mathrm{in} + (1 - \Gamma) g_\mathrm{out} \ . \tag{11}$$

An important parameter to assess the degree of selection of the desired mode is the difference between its threshold gain and that of the most competitive mode. With the confinement factors of the selected and the competitive mode, Γ_s and Γ_c, respectively, it is written as

$$\Delta g_\mathrm{th} = (\Gamma_\mathrm{s} - \Gamma_\mathrm{c}) \cdot (g_\mathrm{out} - g_\mathrm{in}) \ . \tag{12}$$

For an 8-spot relief, the most competitive mode of the E_{81} is the $E_{12\,1}$ mode. The confinement factors of both modes decrease with increasing aperture width, as shown in Fig. 7 (top left) for aspect ratios of 8 and 10. The corresponding threshold gains for these modes on the other hand increase with increasing aperture width, as seen in Fig. 7 (top right), for $g_\mathrm{in} = 850\,\mathrm{cm}^{-1}$ and $g_\mathrm{out} = 3575\,\mathrm{cm}^{-1}$, structure number 1. However, the threshold gain

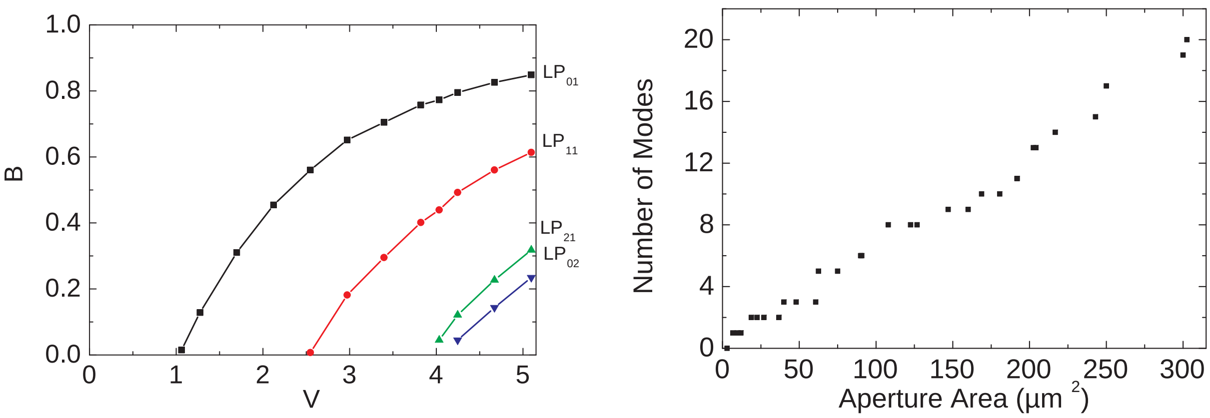

Fig. 6: Numerically calculated BV diagram of circular-shaped VCSELs (left) and the number of modes as a function of the aperture area (right).

difference tends to decrease as the aperture increases. This is shown in Fig. 7 (bottom) for an aspect ratio of 10. In case of a ratio of 8, a slight maximum appears for aperture widths of $d \approx 7\,\mu\text{m}$. From (12) it is understood that mode selection is the better, the higher is the difference in threshold gains inside and outside the etched regions. For this purpose, another structure (number 2) has been utilized with $g_{\text{in}} = 1401\,\text{cm}^{-1}$ and $g_{\text{out}} = 6318\,\text{cm}^{-1}$. The threshold gains of the modes as well as their difference are plotted in Fig. 8 (left). In practice, the higher thresholds of the modes in this structure prevented lasing entirely, and we had to pre-etch the antiphase layer by 16 nm to reduce g_{out} from $6318\,\text{cm}^{-1}$ to $3025\,\text{cm}^{-1}$. The results for this structure (number 3) are shown in Fig. 8 (right). Experimentally, in order to identify the main laser mode, we have performed a spectrally resolved near-field measurement by scanning a lensed fiber tip over the output aperture with high resolution. The obtained pattern is shown in Fig. 9 (left). There are eight intensity maxima in x-direction and one maximum in y-direction, as expected for the E_{81} mode. There is a certain non-uniformity among the peak intensities, however, selection of the lasing pattern. The simulated intensity of this mode is shown in Fig. 9 (right).

3. Conclusions

Using two different approaches, we have investigated the guided modes in oblong-shaped VCSELs. The BV diagrams of such structures are calculated for different aspect ratios. The parameters that control which modes can lase, namely the confinement factors, the threshold gains of the modes, and the gain difference are determined as a function of the aperture width. Three different structures have been utilized to promote operation of a targeted higher-order transverse mode and a first successful experimental demonstration has been made.

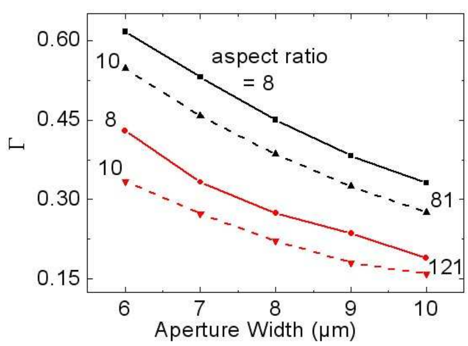

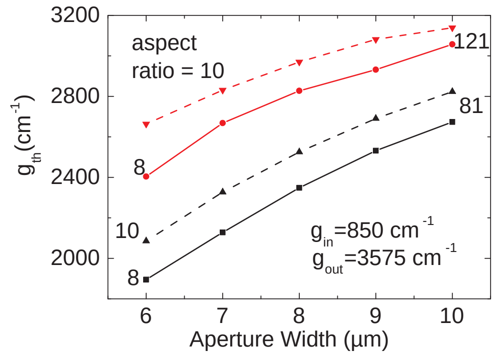

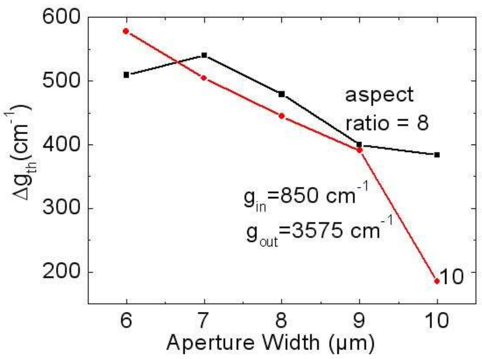

Fig. 7: Dependence of the confinement factor Γ (top left), the threshold gain g_{th} (top right), and the gain difference Δg_{th} (bottom) between the E_{81} and E_{121} modes on the aperture width d for structure number 1. Aspect ratios a/d are both 8 and 10. The individual diameter of an etch spot is 4 µm.

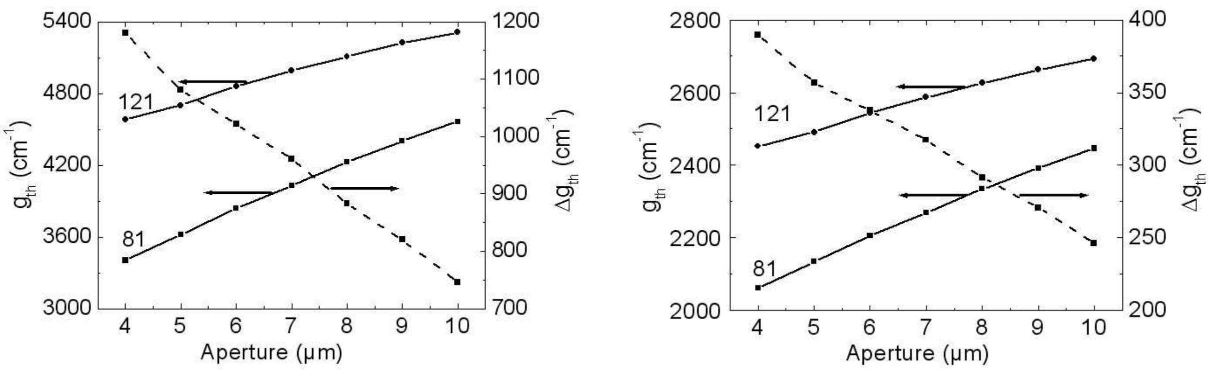

Fig. 8: The threshold gains and their difference in VCSELs with layer structure 2 (left) and structure 3 (right) as a function of the aperture width d for the modes E_{81} and E_{121}. Aperture length and width are related by $a - d = 62$ µm, i. e., the aspect ratio is not constant here.

Acknowledgments

The authors thank U-L-M photonics GmbH for providing the wafer material for some of the studies. Thanks are also due to Ivan Safanov who helped with some useful calculations.

References

[1] H.J. Unold, S.W.Z. Mahmoud, R. Jäger, M. Grabherr, R. Michalzik, and K.J. Ebeling,“Large area single-mode VCSELs and the self-aligned surface relief”, *IEEE J. Select. Topics Quantum Electron.*, vol. 7, no. 2, pp. 386–392, 2001.

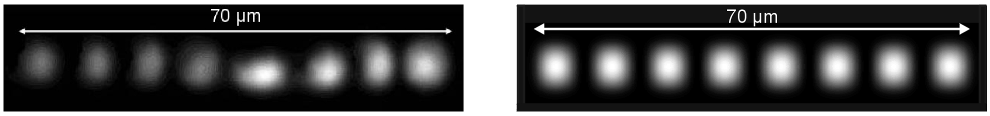

Fig. 9: Measured near-field intensity profile of 8-spot relief VCSELs recorded at 33 mA for structure 1 (left), and the corresponding simulated intensity profile of the selected E_{81} mode (right). The active aperture area is $8 \times 70\,\mu m^2$.

[2] D. Wiedenmann, M. Grabherr, R. Jäger, and R. King, "High volume production of single-mode VCSELs", in *Vertical-Cavity Surface-Emitting Lasers X*, C. Lei, K.D. Choquette (Eds.), Proc. SPIE 6132, pp. 1–12, 2006.

[3] A. Kroner, F. Rinaldi, R. Rösch, and R. Michalzik, "Optical particle manipulation by application-specific densely packed VCSEL arrays", *Electron. Lett.*, vol. 44, 2008, in press.

[4] P.R. Claisse, W. Jiang, P.A. Kiely, B. Gable, and B. Koonse, "Single high order mode VCSEL", *Electron. Lett.*, vol. 34, no. 7, pp. 681–682, 1998.

[5] E.A.J. Marcatili, "Dielectric rectangular waveguide and directional coupler for integrated optics", *Bell Syst. Tech. J.*, vol. 148, pp. 2071–2102, 1969.

[6] R. Michalzik and K.J. Ebeling, "Generalized BV diagrams for higher order transverse modes in planar vertical-cavity laser diodes", *IEEE J. Quantum Electron.*, vol. 31, no. 8, pp. 1371–1379, 1995.

[7] R. Michalzik and K.J. Ebeling, "Operating Principles of VCSELs", Chap. 3 in *Vertical-Cavity Surface-Emitting Laser Devices*, H. Li and K. Iga (Eds.), pp. 53–98. Berlin: Springer-Verlag, 2003.

[8] S.A. Schecanoff, *Electromagnetic Waves*, New York : D. Van Nostrand, p. 94, 1943.

Intrapixel Health Monitoring by Coupled Spontaneous Emission in Small-Pitch Flip-Chip-Bonded 10-Gbit/s 2-D VCSEL Arrays

Hendrik Roscher

In an effort to create architectures of high element-count vertical-cavity surface-emitting laser (VCSEL) arrays that are forgiving of a limited number of device failures, we have demonstrated pixel designs with redundancy of sources. The new pixel consists of three identical, individually addressable lasers that are flip-chip bonded directly to the device mesas. All VCSELs in a pixel share some mirror layers that serve to couple a fraction of spontaneous emission between them. Spontaneous emission is a function of carrier density, and carrier density above threshold a measure of the total losses in the structure. The generated photocurrent in idle devices of the same pixel can hence be employed to detect degradation in the transmitting laser. This is a novel scheme of efficient transmitter-side monitoring in individual channels without intercepting coherent emission, and without integration of extra monitor photodiodes that would jeopardize compactness and low-cost fabrication.

We have implemented a redundant pixel architecture for 850 nm wavelength, 10-Gbit/s serial data rate, two-dimensional (2-D) VCSEL arrays [1] as a possible cost-efficient solution to VCSEL reliability concerns in increasingly emerging high element-count array applications [2], [3]. Following a sparing strategy, the new pixel consists of three identical lasers instead of one. The additional VCSELs are there to monitor the transmitting laser, and to expeditiously replace it in case of failure or undue degradation.

Redundancy is a powerful method to improve reliability. Yet, with alternative laser sources available in each channel, the arising question is how a VCSEL failure can be detected. The driver circuit should be able to respond to a failure by permanently switching to one of the backup VCSELs held in reserve in each channel. An apparent but perhaps less elegant solution is to employ a separate feedback channel over which the receiver signals the non-functioning channel to the transmitter. Clearly, there is a need for VCSEL health monitoring directly on the transmitter side of an optical data link.

External monitor diodes are generally used for dynamic power stabilization in solitary devices, but cannot distinguish between individual channels of high-density arrays. There have been several publications of monolithic integration of monitor diodes with VCSEL structures, both as extra-cavity structures intercepting the light output [4] or as intracavity quantum well absorbers [5]. However, the integration of absorbing elements with the laser structure interferes with its optical properties and entails a more complex fabrication (growth of additional epitaxial layers and extra fabrication steps) of these three-terminal devices. Another possibility is to flip-chip bond the VCSEL array to a corresponding array of photodiodes to monitor the residual back emission [6]. This, however, precludes direct-mesa bonding needed for thermal management.

All the aforementioned implementations aim for a linear photocurrent response to the coherent laser emission as a direct measure of the output power, for instance, to insure that eye safety limits are not exceeded. However, to a greater or lesser extent, the detectors are also sensitive to the spontaneous emission, and the recorded signals need to be corrected for this in order to give an accurate measure of the output power.

The present pixel design follows a different approach: Instead of measuring the coherent output we access internal data, namely the carrier density via spontaneous emission. As one of the key internal parameters for lasing operation, this will provide just as valuable status information concerning degradation. The excess carrier density in the active region of a laser diode above threshold assumes a value that corresponds to the total losses in the structure. It may hence be used as a measure of degradation.

To this end, we have implemented a pixel structure that allows mutual monitoring between equal VCSELs by coupled spontaneous emission. Figure 1 displays the pixel in a schematic cross-section that includes two of three VCSELs. The three-laser pixels are hybridized onto a silicon development platform via flip-chip bonding to emulate a typical configuration where optical sources are mated with, e.g., CMOS compatible electronics. While the fabrication details are explained elsewhere [1], this technology relies on the following capabilities: self-aligned top contact formation, dry etching to produce vertical mesa sidewalls of marginal roughness, lateral oxidation for current confinement, a flip-chip process utilizing non-planar bond pads along with elongated and compressed bumps to prevent shorts, and, eventually, complete substrate removal to define the outcoupling facets.

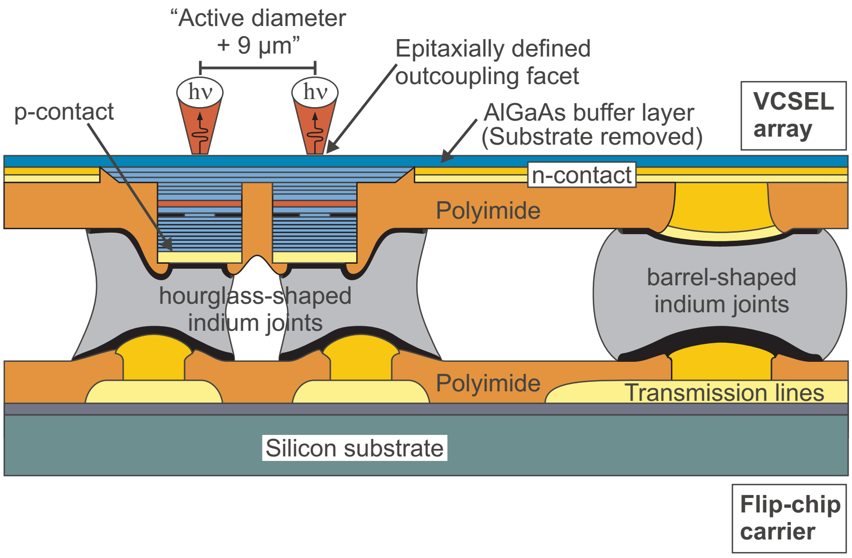

Fig. 1: Schematic cross-section of the complete pixel, including densely packed direct-mesa bonded VCSELs with common n-type mesa and solder joints of reduced cross-section preventing electrical shorts between individually addressable lasers [1].

This last step also produces a structure resembling a planar waveguide that is composed of stacked epitaxial mirror and current injection layers of about 5 to 6 µm total thickness. The lasers are connected by this waveguide in the lateral direction just beneath the inner cavities. The structure of separate close-spaced top mesas sitting on a shared bottom mesa is essentially a structure of pn-junctions coupled to a film waveguide. Without substrate, a major source of thermal crosstalk is eliminated. However, these devices now lack a natural heat spreader that distributes dissipated heat over a large surface area from where it can then be removed by convection.

The design aims at closest possible center-to-center distances for mesa-isolated VCSELs while maintaining good thermal and dynamic characteristics. For device thermal management, the solder balls are placed over the mesas to create alternate paths for outflow of heat, allowing high-current VCSEL operation without excessive internal heating. Tight thermal coupling of each laser via the solder joints to the adjacent substrate also diminishes the parasitic thermal coupling caused by the shared planar waveguide whose actual function is optical coupling of spontaneous emission.

The measurements displayed in Fig. 2 show that the idle backup VCSELs in the pixel receive a fraction of incoherent radiation coming from the emitting laser. The photocurrent behavior in one of the two unbiased VCSELs against the laser current of the operating VCSEL resembles the expected behavior of the carrier density inside the laser. The light–current–voltage (LIV) curves were independently recorded with a computer-controlled setup. The photocurrent curve is obtained by manually taking the values from an ampere meter every 0.5 mA. In this case, the recording of those values was stopped at roll-over of

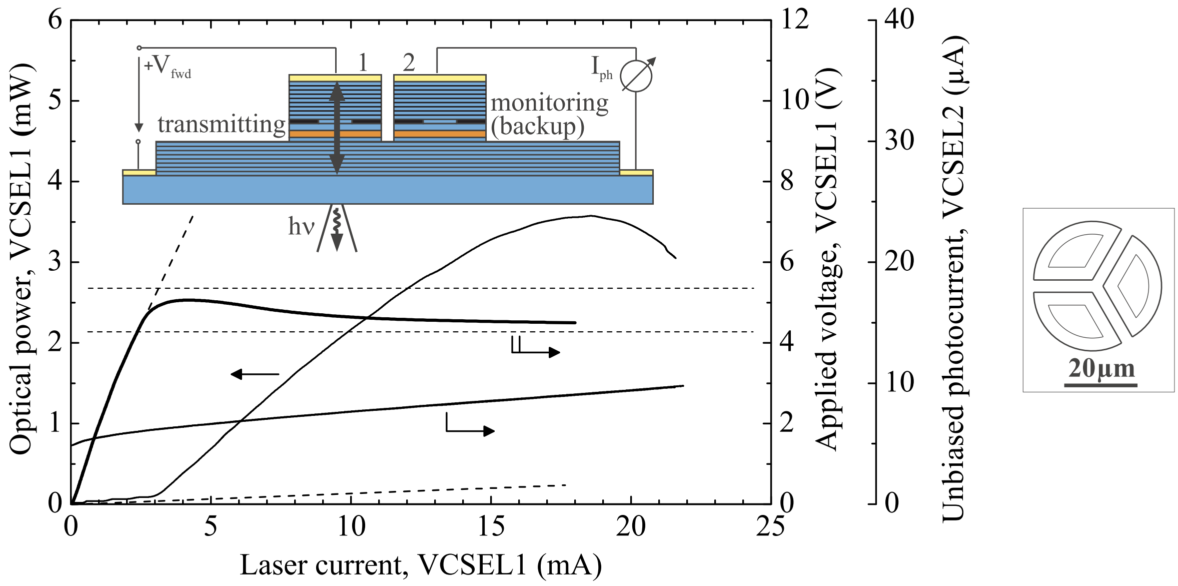

Fig. 2: LIV curves of VCSEL 1 and corresponding unbiased photocurrent I_{ph} of VCSEL 2 of the same pixel. These VCSELs are wedge-shaped with active areas of about 84 µm^2, mesas are separated in this case by a 3.3 µm wide trench. The schematic on the right is a true-to-scale representation of this pixel. A more detailed description of wedge VCSELs is provided in [7]. The dashed lines are explained in the text.

the LI curve since this fully covers the practically relevant operation range of the VCSELs.

While the total rate of recombination processes below threshold is directly proportional to current density, the actual increase in excess carrier densities with current density is slower than linear because the lifetime of carriers becomes ever shorter as their numbers grow. Spontaneous emission is what ignites lasing. In a perfect gain region of a laser, all injected carriers are turned into suitable photons through bimolecular recombination (which is predominantly radiative in a direct bandgap semiconductor). There are, however, unwanted competing recombination channels that consume part of the carriers and eventually only add to heat generation rather than providing optical gain. Non-radiative multi-particle processes such as Auger recombination by nature become more likely as particle densities go up. Hence they take away an ever greater portion of the injected current as it is increased.

The photocurrent reading is a result only of the wanted radiative recombination, and the fact that an increasing part of the current flows through non-radiative channels as threshold is approached expresses itself in a continuous decline of the slope. It should be mentioned that part of the spontaneous emission is likely to come from the barrier layers surrounding the active quantum wells which to some extend will escape fundamental absorption (with the possibility of subsequent recycling) in lower bandgap mirror layers. In Fig. 2, the photocurrent below threshold shows, however, only a relatively minor deviation from a straight line which indicates a high internal efficiency of the device.

The total recombination rate $R_{\mathrm{tot}} \propto j$ is the sum of radiative and non-radiative processes, $R_{\mathrm{tot}} = R_{\mathrm{r}} + R_{\mathrm{nr}}$, where $R_{\mathrm{r}} \propto n^2$ (two-particle process) and $R_{\mathrm{nr}} \propto n^3$ (three-particle Auger process), j is the current density and n the excess carrier density. The latter proportionality is true when non-radiative recombination via traps (intermediate level states) is neglected. Recombination via traps possesses a lifetime that is linked to the trap nature and is thus independent of carrier density, leading to a linear increase of both carrier density and recombination rate with current density.

It is noted that this analysis assumes there are no geometric effects to alter the received portion of spontaneous emission through spatial redistribution of carrier densities while the current is being increased up to threshold. Below threshold this seems reasonable, since current crowding effects should be negligible at low currents, and there is also no spatially varying mode pattern to interact with the carrier distribution. Furthermore, within the limited current range under consideration, the carrier injection efficiency is assumed constant. Reference [8] provides a more in-depth treatment how nonradiative recombination can be investigated through lateral spontaneous emission.

The situation changes on reaching threshold, where onset of lasing provides an extremely efficient mechanism to instantly convert additionally injected carriers into photons of the lasing modes. The carrier density is thereby effectively pinned to the value that corresponds to the total amount of optical losses in the laser. A combination of several factors may cause the decline of photocurrent beyond threshold that is nevertheless observed in Fig. 2. One mechanism is the positive temperature coefficient of the mirror contrast, namely the refractive index step between alternating distributed Bragg reflector layers in the mirrors, $\partial\Delta\bar{n}/\partial T > 0$. It works to reduce the mirror losses and hence the carrier density above threshold when the internal temperature rises.

However, other temperature-dependent properties like the gain-to-resonance detuning and carrier heating may also interfere. Especially for multimode VCSELs, the modal structure will change considerably with laser current. Its interplay with the spatial and spectral carrier distributions will alter the number of carriers contributing to spontaneous emission. And after all there is no certainty whether the sensing device receives a constant portion of the total emitted incoherent radiation. A spatial variation of the charge distribution caused, for instance, by current crowding and spatial hole burning might well lead to a varying degree of radiation shielding by the trench between devices.

Figure 3 demonstrates in the right hand part how the spontaneous emission is distributed within a pixel. The bright spot in the center is surface-normal emission from the outcoupling facet of the forward-biased VCSEL. It is driven below threshold here, so the weak lateral radiation can be observed. On the left, the figure shows the mesa structure that is, in a flipped-over position according to Fig. 1, on the underside of that pixel. This scan is prior to flip-chip packaging and substrate removal. The three small mesas define the substrate-side emitting VCSELs, dry-etched through the active layers to a depth of 6 μm and separated by 1.5 μm at the smallest distance.

There is weak radiation from the edges of the shared epitaxial layers that gives evidence of guided spontaneous emission. Apparently, the wet-etched bottom mesa with its epitaxial layers is acting as a waveguide in the lateral direction. Wave propagation inside a similarly layered structure has already been reported in [9]. The observed emission from the edges of the large bottom mesa suggests that this sensor function could work over larger device-to-device spacings than implemented in this work. The two especially dark circular areas adjacent to the bright spot of the emitting VCSEL in Fig. 3 reveal the position of the two unbiased VCSELs where the radiation is leaking from the shared waveguide in the vertical direction going into the plane of the paper. This generates a photocurrent in the pn-junctions of those backup VCSELs.

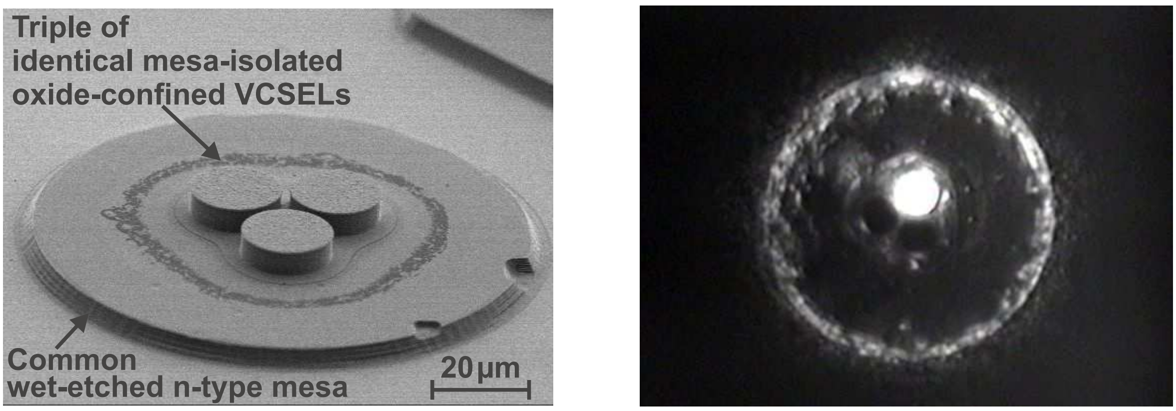

Fig. 3: Scanning electron micrograph (SEM) showing the multi-mesa structure on the underside of a pixel prior to flip-chip packaging and substrate removal (left), and CCD image showing a pixel from the emission side, one VCSEL forward biased far below threshold to demonstrate the distribution of spontaneous emission (right).

We envision that through this behavior, the health of the operating VCSEL can be monitored by at least one of the backup VCSELs in the same pixel. Evaluation of the photocurrent signal will allow to judge whether the transmitting laser is operating within specified parameters. This function is provided with no added complexity to the VCSEL structure and no interference with the coherent emission.

The detection of spontaneous lateral emission has been reported in [10] and [11] with top-emitting VCSEL structures. The detector in [10] is etched through all epitaxial layers to the substrate, so detector and VCSEL do not share any layers. The substrate is not removed and there is a much larger, 30 µm-wide gap between the one VCSEL in the center and a dedicated detector ring enclosing it. The photocurrent of this detector does not saturate and only shows a small slope change at threshold. Besides onset of lasing only in a small portion of the active region there could also be scattering from the sidewalls of those early air-post VCSELs or even from the backside of the substrate such that a fraction of stimulated emission is also detected. Reference [11] in contrast exploits in-plane waveguiding of spontaneous emission in the cavity section for long-range monitoring. The active layers connect VCSELs here over distances of 250 µm.

In the present design, the operating and monitor VCSELs are connected by a thin stack of epitaxial layers immediately below the active regions. In this respect, the configuration is similar to [8]. The active layers are fully separated by etching through to the first layers of the bottom Bragg mirror. It is believed that complete substrate removal of these substrate-side-emitting devices also contributes to the suppression of coherent optical crosstalk while the sharing of most of the n-type Bragg layers sufficiently couples the spontaneous emission to result in a photocurrent signal strong enough for monitoring purposes.

It is unclear at this point to what degree the close proximity of the semiconductor–air interface contributes to the lateral coupling or waveguiding. In the absence of total internal reflection at this interface, the distributed Bragg reflector layers could still offer sufficient Bragg reflection for rays incident under an appropriate range of angles. Then this scheme could also be used with on-substrate VCSELs. Coherent crosstalk via the distant semiconductor–air interface at the backside of the substrate should then probably be suppressed by an antireflection coating which is advisable in any case for through-substrate backside emission to avoid the external resonator. A broader band multi-layer antireflection coating might be in order to account for the beam divergence and prevent reflections into laterally displaced backup VCSELs besides the prevention of direct feedback of perpendicular rays into the emitting laser.

In any case, after proper calibration, the excess carrier density in the active region of the operating laser can be observed along with the threshold current. Both are measures of the optical losses in the laser and should give a good indication of its status. Defect formation, diffusion processes of doping species in the Bragg mirrors, facet damage, or simply device failure are examples that would alter the excess carrier density and/or threshold current. In connection with information about the laser current, other problems such as incomplete current injection or current leakage can also be detected.

We suggest that if the photocurrent leaves a predefined band such as indicated in Fig. 2, it can be concluded that the operating VCSEL reached its end of life. In case a laser fails to lase but still produces spontaneous emission, it essentially works as an LED and there will be no gain clamping. In this case, the carrier density and hence the spontaneous emission will not saturate but continue to increase with the laser current beyond threshold. The photocurrent curve will then leave the predefined band through the top boundary. This is indicated by the dashed line extending the subthreshold part of the photocurrent curve in Fig. 2. At this point, one of the two backup lasers ought to be invoked by the electronics to continue transmission over the affected channel.

Besides detecting VCSEL failure, this function may also provide a means of in-situ monitoring of changes in optical feedback, for instance from the fiber endface, since feedback effectively changes the reflectivity of the outcoupling mirror, hence altering the carrier density. In a real transceiver package, the feedback level may change on a slow time scale, for instance with temperature fluctuations or otherwise induced mechanical stress. Due to their "temporal signature", isolation of the feedback-related changes might be possible. If feedback sensitivity is an issue, the sensor function could proof useful in assessing fiber-pigtailed packages in this respect.

Before deployment in a real transceiver, extensive tests will of course be needed for calibration of the sensor function. Data need to be acquired on how the photocurrent reacts to what mechanism of device aging or failure. Here, we merely demonstrate the principle and explain the potential we see for it. Apart from the described use, another mode of operation is conceivable where all three VCSELs in a pixel are simultaneously transmitting the same signal with a large enough power budget to keep the channel operational as long as one of the VCSELs is still functioning. This approach is attractive in that it largely avoids the added capabilities needed in the driver circuitry to monitor and manage the VCSELs within a pixel, although other difficulties such as synchronization or difference frequency generation at the photodetector might arise.

Thought has to be given to problems such as area-correlated failures in dense arrays which have an impact on the expected extension of lifetime achieved through provisioning of backup devices. We believe that the low power densities in the VCSELs during sensing will not contribute much to their aging, despite the elevation of temperature they undergo because of intra-pixel thermal crosstalk.

Acknowledgment

Special thanks are due to Andrea Kroner and Philipp Gerlach for stimulating discussions regarding the sensor functionality.

References

[1] H. Roscher, F. Rinaldi, and R. Michalzik, "Small-pitch flip-chip bonded VCSEL arrays enabling transmitter redundancy and monitoring in 2-D 10-Gbit/s space-parallel fiber transmission", *IEEE J. Select. Topics Quantum Electron.*, vol. 13, pp. 1279–1289, 2007.

[2] J.E. Cunningham, D.K. McElfresh, L.D. Lopez, D. Vacar, and A.V. Krishnamoorthy, "Scaling vertical-cavity surface-emitting laser reliability for petascale systems", *Appl. Opt.*, vol. 45, pp. 6342–6348, 2006.

[3] N. Mukoyama, H. Otoma, J. Sakurai, N. Ueki, and H. Nakayama, "VCSEL array-based light exposure system for laser printing", in *Vertical-Cavity Surface-Emitting Lasers XII*, C. Lei, J.K. Guenter (Eds.), Proc. SPIE 6908, pp. 69080H-1–11, 2008.

[4] G. Hasnain, K. Tai, Y.H. Wang, J.D. Wynn, K.D. Choquette, B.E. Weir, N.K. Dutta, and A.Y. Cho, "Monolithic integration of photodetector with vertical cavity surface emitting laser", *Electron. Lett.*, vol. 27, pp. 1630–1632, 1991.

[5] G. Steinle, D. Wolf, M. Popp, and K.J. Ebeling, "Vertical-cavity surface-emitting laser monolithically integrated with intracavity monitor diode with temperature-insensitive responsivity", *Electron. Lett.*, vol. 37, pp. 34–36, 2001.

[6] K.W. Goossen, J.E. Cunningham, and A.V. Krishnamoorthy, "1 × 12 VCSEL array with optical monitoring via flip-chip bonding", *IEEE Photon. Technol. Lett.*, vol. 18, pp. 1219–1221, 2006.

[7] H. Roscher, P. Gerlach, F.N. Khan, A. Kroner, M. Stach, A. Weigl, and R. Michalzik, "Toward more efficient fabrication of high-density 2-D VCSEL arrays for spatial redundancy and/or multi-level signal communication", in *Micro-Optics, VCSELs, and Photonic Interconnects II: Fabrication, Packaging, and Integration*, H. Thienpont, M.R. Taghizadeh, P. Van Daele, J. Mohr (Eds.), Proc. SPIE 6185, pp. 61850V-1–12, 2006.

[8] J.-H. Shin and Y.H. Lee, "Determination of nonradiative recombination coefficients of vertical-cavity surface-emitting lasers from lateral spontaneous emission", *Appl. Phys. Lett.*, vol. 67, pp. 314–316, 1995.

[9] A.Y. Cho, A. Yariv, and P. Yeh, "Observation of confined propagation in Bragg waveguides", *Appl. Phys. Lett.*, vol. 30, pp. 471–472, 1977.

[10] K.D. Choquette, N. Tabatabaie, and R.E. Leibenguth, "Detector-enclosed vertical-cavity surface emitting lasers", *Electron. Lett.*, vol. 29, pp. 466–467, 1993.

[11] C. Bringer, V. Bardinal, E. Daran, T. Camps, Y.G. Boucher, G. Almuneau, O. Gauthier-Lafaye, P. Dubreuil, J.-B. Doucet, and C. Fontaine, "Detection of lateral spontaneous emission for VCSEL monitoring", in *Micro-Optics, VCSELs, and Photonic Interconnects*, H. Thienpont, K.D. Choquette, M.R. Taghizadeh (Eds.), Proc. SPIE 5453, pp. 209–216, 2004.

Full-Duplex Bidirectional Optical Data Transmission over 50 μm-Core Graded-Index Multimode Fiber with Monolithically Integrated Transceiver Chips

Martin Stach

We present bidirectional data transmission experiments in half- and full-duplex mode at 1 Gbit/s data rate over 500 m graded-index multimode fiber with VCSELs and MSM photodiodes as parts of a novel GaAs-based monolithically integrated transceiver chip.

1. Introduction

For a wide range of interconnect applications, bidirectional optical data transmission in the Gbit/s range is very desired. Monolithically integrated transceiver (Tx/Rx) chips for 850 nm wavelength operation have recently been presented [1], which consist of a vertical-cavity surface-emitting laser diode (VCSEL) and a metal–semiconductor–metal photodiode (MSM PD) and are suited for coupling to a 100 μm core diameter fiber. Nevertheless, owing to the applied lithographic process, they are not well suited for standard graded-index multimode fibers (MMFs) with smaller core. A new generation of chips (Fig. 1) presented in this article is based on a completely revised and simplified process technology. Due to a significant reduction of the VCSEL diameter, the detection area is increased and a centered laser diode can be realized for Tx/Rx chips with 110 μm diameter, which drastically enhances coupling tolerances between chip and fiber. Even quasi error-free full-duplex 1 Gbit/s bidirectional data transmission over a 500 m-long MMF with 50 μm core diameter is possible and shows the high potential of the given approach for various low-cost datacom applications.

2. Transceiver Chip Fabrication

The monolithically integrated transceiver chip contains all layers necessary for signal generation and reception. The MSM PD layer structure includes a 1 μm-thick GaAs absorption layer and is grown on top of the VCSEL layers. More information on the layer sequence is available in [2]. To access the highly p-doped cap layer of the VCSEL, the detector layers within the resist-protected photodiode area are selectively removed by citric acid solutions. The process is terminated at an AlAs etch-stop layer which is subsequently removed by hydrofluoric acid. A dry-etch process is applied to define the VCSEL mesa, during which the photodiode is protected by photoresist. The new design allows the photodiode metallization on a planar surface. Since edge effects are avoided, the device spacing can be reduced and decreased finger width as well as narrower interdigital spacing are more feasible. The circular trench in Fig. 1 separates VCSEL and photodiode and is subsequently filled with polyimide. Only one metallization step is required to contact both the p-side of the VCSEL and to put bondpads on the surface. A small polyimide stripe from the previous lithographic step provides a resistance of several 10 MΩ between VCSEL and photodiode top metallization. The PD diameter equals 110 µm. It is well suited for fibers with up to 100 µm core diameter which shall be centered in front of the device. Tx/Rx chips with both centered and off-centered VCSELs have been processed.

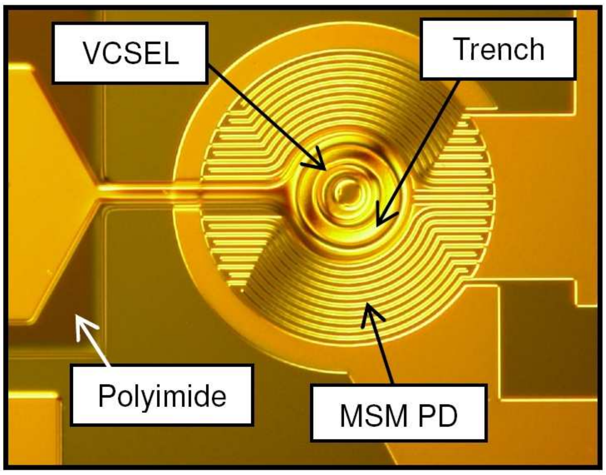

Fig. 1: New-generation transceiver chip with 110 µm diameter containing a centered VCSEL. The 1 µm PD fingers are separated by 2 µm interdigital spacings [3].

3. Effective Responsivity and Coupling Efficiency

We investigate the conditions for butt coupling to a MMF with 50 µm core diameter and a numerical aperture of 0.2. As indicated in Fig. 2, the MMF is scanned in y-direction over a PD with 1.5 µm finger width and 2.5 µm spacing, at a constant distance between fiber and PD of $\Delta z = 50$ µm. The effective responsivity reaches values of as high as 0.35 A/W for ±40 µm lateral offset, where the fiber almost entirely faces the PD area (see inset). With a centered fiber, the effective responsivity is much increased with higher distance between fiber and chip. As seen in Fig. 3, a peak value of 0.26 A/W is found at 380 µm displacement.

The VCSEL-to-fiber coupling efficiency amounts to approximately 70 % for a centered laser diode, where Fresnel losses are included. The 3-dB decay occurs at $\Delta z = 150$ µm. At a constant distance of 50 µm between VCSEL and fiber, the 3-dB decay is found at ±20 µm lateral displacement. Thus, using butt coupling, a tradeoff exists between high input coupling and high effective responsivity.

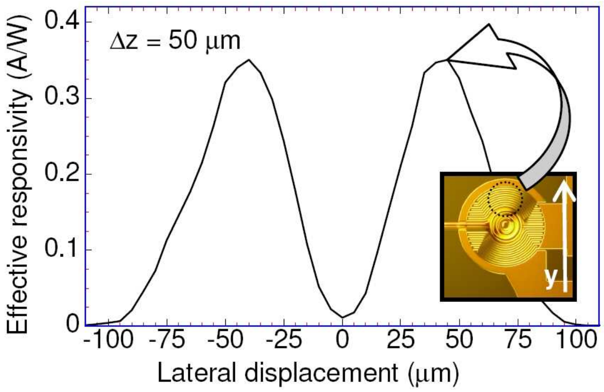

Fig. 2: Effective responsivity of a Tx/Rx chip with a centered VCSEL under lateral displacement of a butt-coupled ($\Delta z = 50\,\mu$m) MMF with 50 µm core diameter.

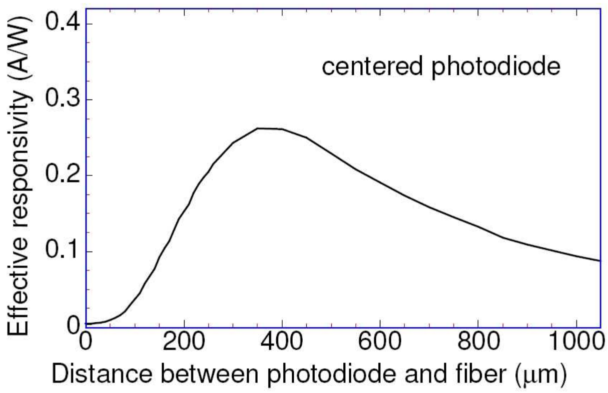

Fig. 3: Effective responsivity for a variation of the distance between PD and MMF, corresponding to 0 µm lateral displacement in Fig. 2.

4. Digital Data Transmission

For bidirectional data transmission, one butt-coupled Tx/Rx chip at each fiber end is used, i.e., there are no optics between chip and fiber and the distance is about 50 µm. Each transceiver chip consists of a 110 µm MSM PD with 1.5 µm finger width and 2.5 µm spacing and an oxide-confined VCSEL with a 3-dB bandwidth exceeding 5 GHz. For data transmission experiments in half-duplex mode, one VCSEL is modulated, while the other one is biased above threshold. Optimum alignment is achieved if the photocurrent at each side is maximized. To control the received AC signals simultaneously, the "data" and "data-not" outputs of the pattern generator are used and both PD signals are monitored on an oscilloscope. Low-pass filters with $f_{3\,\mathrm{dB}} = 1100\,\mathrm{MHz}$ are employed at each side during all experiments. The half-duplex eye diagrams have been recorded by turning off one of the modulation signals. Regarding the coupling efficiencies, the position of the VCSEL was somewhat off-center with respect to the fiber axis. At this position, the effective responsivity of the PD was 0.1 A/W, indicating a loss of about 5 dB at each PD side. The eye diagrams for transmission of a non-return-to-zero pseudo random bit sequence of $2^7 - 1$ word length at 1 Gbit/s data rate over 500 m MMF with 50 µm core diameter show a large eye opening, indicating error-free transmission (Figs. 4a and b). The eye diagrams slightly differ in shape since the VCSELs have different active diameters. Even in full-duplex mode at 1 Gbit/s, error-free data transmission is enabled (Fig. 4c). The reduced eye opening and increased noise are mainly due to electrical crosstalk on the same chip and reflections from the opposite chip, producing far-end optical crosstalk.

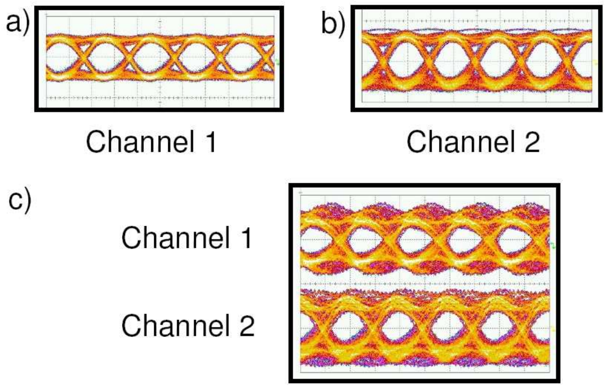

Fig. 4: Eye diagrams for bidirectional data transmission at 1 Gbit/s data rate over 500 m of 50 µm core diameter MMF in half-duplex mode (a and b) and full-duplex mode (c).

5. Conclusion

We have developed a new generation of 850 nm wavelength transceiver chips. Centered VCSEL placement allows direct butt coupling or the use of, e.g., simple ball lens optics. With butt coupling conditions, 1 Gbit/s data have been sent over 500 m of 50 µm MMF even in full-duplex mode. Future generations of smaller chips are targeted to provide improved coupling tolerances.

References

[1] M. Stach, F. Rinaldi, A. Gadallah, S. Lorch, I. Kardosh, P. Gerlach, and R. Michalzik, "1 Gbit/s bidirectional data transmission over 100 m graded-index glass optical fiber with monolithically integrated transceiver chips", in Proc. *32nd Europ. Conf. on Opt. Commun., ECOC 2006*, vol. 3, pp. 493–494. Cannes, France, Sept. 2006.

[2] M. Stach, F. Rinaldi, M. Chandran, S. Lorch, and R. Michalzik, "Bidirectional optical interconnection at Gb/s data rates with monolithically integrated VCSEL–MSM transceiver chips", *IEEE Photon. Technol. Lett.*, vol. 18, pp. 2386–2388, 2006.

[3] M. Stach, F. Rinaldi, D. Wahl, D. Rimpf, S. Lorch, and R. Michalzik, "1 Gbit/s full-duplex bidirectional optical data transmission over 500 m of 50 µm-core graded-index multimode fiber with novel monolithically integrated transceiver chips", in Proc. *33rd Europ. Conf. on Opt. Commun., ECOC 2007*, vol. 5, pp. 127–128. Berlin, Germany, Sept. 2007.

Feedback-Dependent Threshold of Electrically Pumped VECSELs

Wolfgang Schwarz

We present the investigation of the feedback-dependent threshold of an 822 nm wavelength electrically pumped vertical-external-cavity surface-emitting laser (VECSEL). The setup is capable of resolving micrometer-size features on the laser surface, while demanding highly accurate alignment. Modified design criteria are developed, which address this issue, and approaches for the fabrication of miniaturzied devices are outlined.

1. Introduction

In biochemical analysis, the trend to smaller systems has progressed to the detection of volumes in the sub-femtoliter range [1,2]. Such small volumes allow the observation of single molecules together with an economic utilization of the investigated substances. Unlike an integrated sensing scheme, which makes use of single-pass excitation [3], the detection limit can be improved when the detected particle is located inside an optical resonator. The advantages of using vertical-cavity surface-emitting lasers (VCSELs) in such an arrangement are electrical pumping with low operating currents, the potential for low cost, and the circular output beam with the ease of building a stable resonator. The latter has been demonstrated in electrically and optically pumped devices with high efficiencies [4] and even for intra-cavity frequency doubling [5], where a strong field enhancement is required. In intra-cavity sensing, this enhancement is desired as well.

A stable two-mirror resonator incorporating a plane mirror, namely the VCSEL aperture, and an external curved mirror with the radius of curvature ρ supports a laser beam with a spot size w_0, where $w_0^2 = M^2\lambda\sqrt{L\,(\rho - L)}/\pi$ with λ as the wavelength, L as the resonator length, and M^2 as the beam propagation factor [6, 7]. The beam waist is located on the plane mirror. The beam propagation factor describes the diffraction angle of the actual beam in comparison to a Gaussian beam with $M^2 = 1$. Real beams show $M^2 \geq 1$, which reflects the fact that for a given spot size, propagating Gaussian beams broaden the least. The beam spot size is plotted in Fig. 1 versus the resonator length for different beam propagation factors and radii of curvature of 10.3 mm and 250 µm. It is apparent from the diagrams that the beam size scales with the radius of curvature and amounts to about 30 µm for the long resonator and 5 µm for the short resonator. Hence a small beam waist is only attainable with a small radius of curvature. In Fig. 2, the length of stable resonators is depicted for both configurations. If the resonator length approaches the radius of curvature of the external mirror, the beam propagation factor becomes infinitely large, which means high diffraction and higher aperture losses. Stable operation of the long resonator with a spot size of 5 µm can only occur if its length differs by not more than a fraction of a micrometer from the maximum stable length. This requirement is much relaxed in the short resonator. Here the same spot size is attainable by varying the resonator length within 40 µm. These calculations show that the longitudinal alignment of the longer cavity is extremely critical and that for a hybrid fabrication approach, a shorter resonator is favorable.

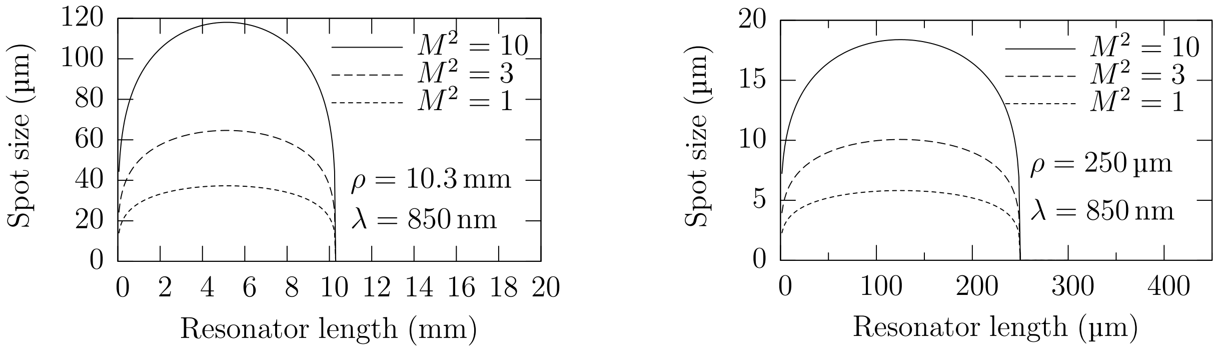

Fig. 1: Calculated beam spot size at the plane mirror versus the length of a plano-convex resonator with radii of curvature of 10.3 mm (left) and 250 µm (right) and different beam propagation factors.

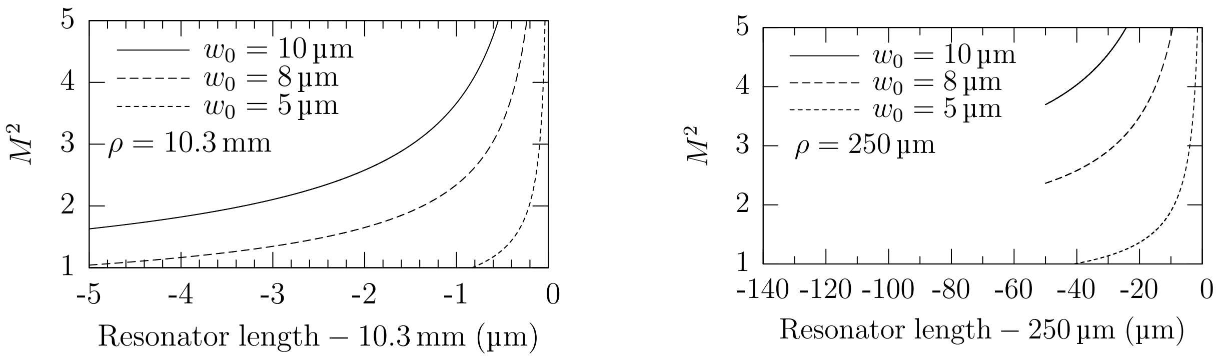

Fig. 2: Calculated beam propagation factor M^2 for different resonator lengths and beam spot sizes. Curved mirrors with $\rho = 10.3$ mm (left) and 250 µm (right) are assumed. The wavelength is 850 nm.

2. Setup and Device Fabrication

The properties of lasers may change significantly when optical feedback is introduced. A shift of the threshold current as well as a modified mode pattern and polarization are typically observed, the latter two particularly in VCSELs [8]. The present investigation is limited to the threshold behavior. A laser is a resonant device, whose resonance condition is dependent on the phase and amplitude of the back-reflected field. In the investigated regime, the external roundtrip delay time is of the same order (in the present case of $L = 10.3$ mm about 68 ps) as the inverse of the relaxation oscillation frequency of the laser. Here, small changes of the resonator length result in an alteration of the phase condition and of the laser threshold.

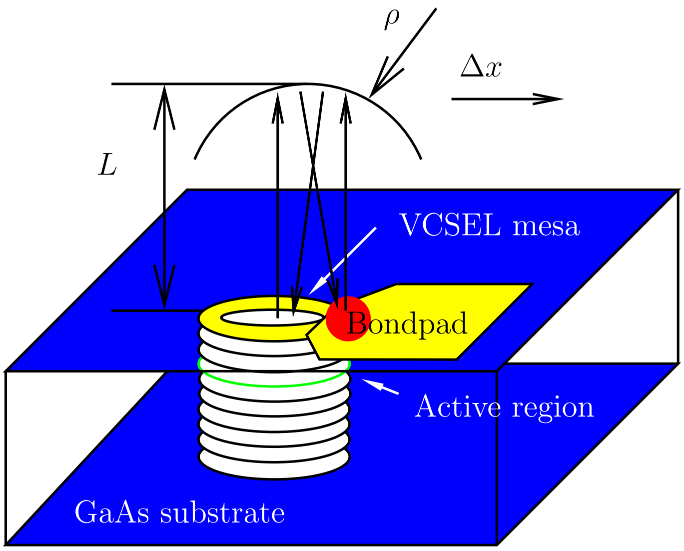

Fig. 3: Schematic drawing of the experimental setup used for the feedback investigations and simplified ray paths for a lateral displacement of the external mirror by an amount Δx.

Figure 3 shows a schematic of the setup. The system comprises a top-emitting VCSEL grown by molecular beam epitaxy. The 822 nm emission wavelength was detuned from the gain peak in the applied GaAs/AlGaAs material system. The active zone of the laser consists of three 8 nm thick quantum wells embedded in 10 nm thick barriers. The active diameter was defined by wet etching of the mesa and subsequent selective oxidation to a diameter of 10 µm. The resonator mirrors consist of 38 n-doped and 23 p-doped distributed Bragg reflector (DBR) pairs. The external mirror made of BK7 glass was coated by plasma-enhanced chemical vapor deposition (PECVD) at 300°C with 8 pairs of Si_3N_4/SiO_2 in order to achieve a reflectivity of 80 % at the operation wavelength. To assess the surface quality, the coating was also applied on a silicon wafer piece. Atomic force microscopy measurements revealed a surface roughness R_s of 4.3 nm root mean square (RMS) resulting from this procedure in comparison with uncoated silicon with $R_s = 0.2$ nm.

At a rough surface with a Gaussian height distribution, the calculated ratio between total scattered and incident light is approximately $1 - \exp\{-(\pi R_s/\lambda)^2\}$ [9]. In the present case, the ratio amounts to $2.5 \cdot 10^{-4}$ and appears negligible when compared with the mirror transmittivity of about 20 %.

The external mirror was mounted on a three-axes positioning system, which was operated unidirectionally for minimum backlash. The plano-concave coated side with a radius of curvature of 10.3 mm faced the VCSEL aperture. During the experiment, the laser was electrically contacted with a needle, which was placed on the bondpad next to the VCSEL mesa.

3. Experimental Results

The threshold of a real laser resonator depends on several parameters such as material absorption, aperture losses, surface scattering, alignment tilt, as well as lateral and longitudinal confinement factors. This contribution investigates the feedback-dependent threshold of a VCSEL.

The light–current (LI) characteristics at power levels close to the VCSEL threshold was recorded (Fig. 4). It was difficult to align the external mirror in a manner that a shift of the threshold current could be observed. The distance between VCSEL mesa and external mirror was slightly smaller than the radius of curvature of the external mirror and had to be kept within a range of less than one micrometer in order to maintain the conditions for low threshold. For mapping the spatial dependence of the feedback on the threshold, the external mirror was displaced laterally and the LI characteristics were recorded in the vicinity of the threshold. The threshold currents were determined by linear regression and are depicted in Fig. 5. The spatially resolved laser threshold clearly represents losses in the resonator. As sketched in Fig. 3, the resonator mode experiences scattering at the etched mesa when the mirror is displaced radially by about half a mesa radius. The actual mode will not shift laterally by twice the displacement, but rather find a position with lower losses. A model as proposed in [10] could predict this loss mechanism more in detail. The setup is even capable of resolving the footprint of the bondpad, where scattering also occurs. The shift in laser threshold ranges from 2.65 mA without feedback to 2.4 mA with feedback. A transfer matrix model predicts a shift in threshold gain from about 4500 cm^{-1} to 2600 cm^{-1} and a related shift in threshold current from 2.1 to 0.5 mA for the given structure and reflectivities, assuming a current–gain dependence from [11] and an internal absorption in the DBR mirrors of 100 cm^{-1}, where gain detuning as well as internal heating are not considered.

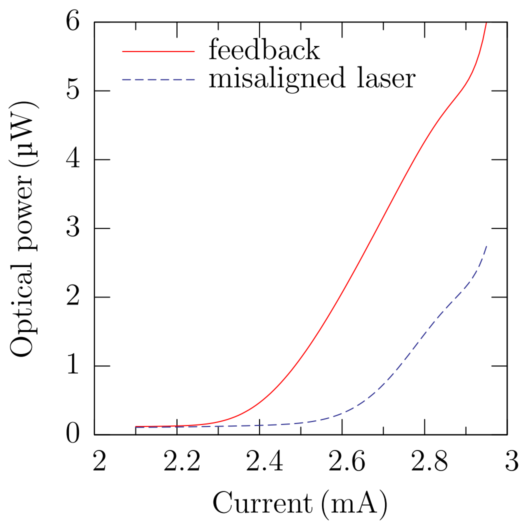

Fig. 4: LI characteristics of the investigated VCSEL with and without optical feedback. Feedback was suppressed by intentionally misaligning the resonator. The optical power was measured through the external mirror, such that just a fraction of the total power was detected.

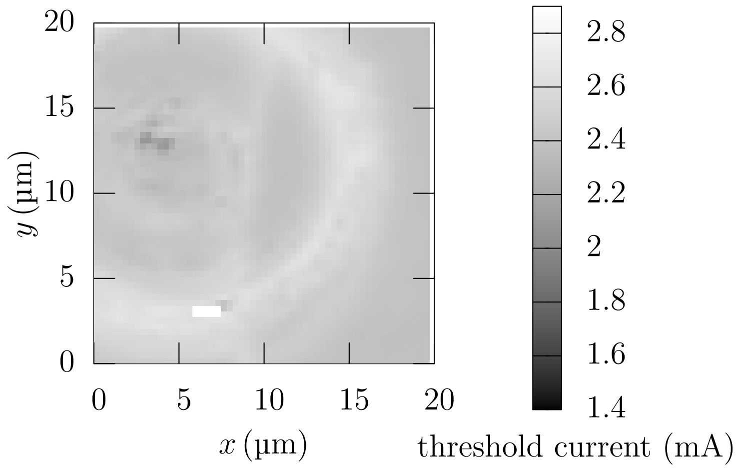

Fig. 5: Two-dimensional map of the VCSEL threshold current at different lateral displacements of the external mirror.

4. Conclusion

A setup for the determination of the feedback-dependent threshold of a vertical-cavity surface-emitting laser facing a curved external mirror is introduced. The setup is very sensitive to misalignment, in accordance with a prediction from a wave-optical model. A 80 % reflective external mirror produced about 10 % relative change in threshold current, which somewhat deviates from the change predicted by a simplified gain model. The relatively low modulation of the threshold current may be attributed to an unidentified loss mechanism. Possible candidates could be an unexpectedly high scattering loss in the external mirror, fundamental absorption in the topmost GaAs layer in the VCSEL aperture, or the critical alignment with possible scattering loss from higher-order mode excitation.

Devices with a shorter cavity are to be considered for a hybrid-integration approach. These devices are less prone to longitudinal resonator length misalignment. Preferably, the lateral alignment of such devices has to be provided by self-alignment features. In this case, the alignment can be achieved with photolithographic precision, which is a prerequisite for low resonator losses.

5. Acknowledgement

The author would like to thank Andrea Kroner for providing the investigated VCSEL and Rudolf Rösch for the PECVD support.

References

[1] A. Manz, N. Graber, and H.M. Widmer, "Miniaturized total chemical analysis systems: a novel concept for chemical sensing", *Sensors and Actuators B*, vol. 1, pp. 244–248, 1990.

[2] S. Nie and R.N. Zare, "Optical detection of single molecules", *Annual Review of Biophysics and Biomolecular Structure*, vol. 26, pp. 576–596, 1997.

[3] E. Thrush, O. Levi, W. Ha, G. Carey, L.J. Cook, J. Deich, S.J. Smith, W.E. Moerner, and J.S. Harris, Jr., "Integrated semiconductor vertical-cavity surface-emitting lasers and pin photodetectors for biomedical fluorescence sensing", *IEEE J. Quantum Electron.*, vol. 40, pp. 491–498, 2004.

[4] E.M. Strzelecka, J.G. McInerney, A. Mooradian, A. Lewis, A.V. Shchegrov, D. Lee, J.P. Watson, K.W. Kennedy, G.P. Carey, H. Zhou, W. Ha, B.D. Cantos, W.R. Hitchens, D.L. Heald, V.V. Doan, and K.L. Lear, "High power, high brightness 980 nm lasers based on extended cavity surface emitting lasers concept", in *High-Power Fiber and Semiconductor Lasers*, M. Fallahi, J.V. Moloney (Eds.), Proc. SPIE 4993, pp. 57–67, 2003.

[5] T. Kim, J. Yoo, K. Kim, S. Lee, S. Lim, G. Kim, J. Kim, S. Cho, J. Lee, and Y. Park, "2 W continuous wave operation of optically pumped blue VECSEL with frequency doubling", in *Vertical-Cavity Surface-Emitting Lasers X*, C. Lei, K.D. Choquette (Eds.), Proc. SPIE 6132, pp. 61320K-1–7, 2006.

[6] A.E. Siegman, "Defining, measuring, and optimizing laser beam quality", in *Laser Resonators and Coherent Optics: Modeling, Technology, and Applications*, A. Bhowmik (Ed.), Proc. SPIE 1868, pp. 2–12, 1993.

[7] B.E.A. Saleh and M.C. Teich, *Fundamentals of Photonics*. New York: John Wiley & Sons, 1991.

[8] C. Masoller and M.S. Torre, "Influence of optical feedback on the polarization switching of vertical-cavity surface-emitting lasers", *IEEE J. Quantum Electron.*, vol. 41, pp. 483–489, 2005.

[9] J.H. Rakels, "Influence of the surface height distribution on the total integrated scatter (TIS) formula", *Nanotechnology*, vol. 7, pp. 43–46, 1996.

[10] A.G. Fox and T. Li, "Computation of optical resonator modes in laser resonators", *IEEE J. Quantum Electron.*, vol. 4, pp. 460–465, 1968.

[11] L.A. Coldren and S.W. Corzine, *Diode Lasers and Photonic Integrated Circuits*. New York: Wiley & Sons, 1995.

Blue Light Emitting Electrically Pumped VECSELs with Optical Powers in the Milliwatt Range

Ihab Kardosh

We report on intracavity frequency doubling of electrically pumped vertical-extended cavity surface-emitting lasers (VECSELs), establishing a blue light source emitting near 485 nm wavelength. The VECSELs have an InGaAs/GaAs gain region and incorporate a nonlinear optical crystal for frequency doubling. Continuous-wave optical output powers of more than 1.5 mW are achieved.

1. Introduction

In the last few years, VECSELs have become an attractive laser source for various applications. Due to favorable features, such as high output power and good beam quality, optically pumped semiconductor VECSELs (OPS-VECSELs) [1] can be used, e.g., in laser printing, absorption spectroscopy or as a pump laser in the near-infrared spectral range. Furthermore, the extended cavity configuration gives the possibility to use a nonlinear optical crystal for second-harmonic generation (SHG) in the visible spectral range. This approach has recently received an increasing interest in applying such OPS-VECSELs in projection television and laser displays. Output powers up to several watts have been demonstrated over a wide spectral range from blue light ($\sim$460–488 nm) [2] to green-yellow ($\sim$555–580 nm) [3,4] and orange near 610 nm [5]. Much more challenging than optical pumping is the electrical pumping concept due to demanding issues such as current spreading in doped layers, ohmic heating, processing and device mounting. Electrically pumped VECSELs (EP-VECSELs) have been first reported by Hadley et al. [6]. Output powers of a few milliwatts in continuous-wave (CW) operation from InGaAs-based devices emitting near 985 nm were demonstrated at that time. In recent years, optical output powers of over 900 mW in multi-mode operation have been achieved from EP-VECSELs with active diameters of 150 µm [7]. Intracavity frequency doubling at 490 nm emission wavelength with output powers of 5–40 mW has been also demonstrated by Novalux [8], where unfortunately, rather few device details are known. To our knowledge, no other group has reported blue-emitting EP-VECSELs with output powers in the milliwatt range. In this paper, we present blue light generation by intracavity frequency doubling in substrate-removed EP-VECSELs with high round-trip gain.

2. Device Structure

The layer structures are grown by solid-source molecular beam epitaxy and are designed for emission wavelengths near 980 nm. The active region contains two stacks of three

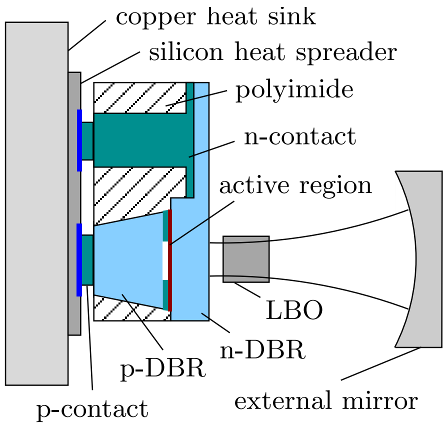

Fig. 1: Schematic VECSEL cross-section.

8 nm thick InGaAs/GaAs quantum wells (with half-wavelength distance) surrounded by two 30 nm thick GaAsP layers for strain compensation. The active diameter is defined by selective oxidation of a 30 nm thick AlAs layer above the active region, located in a node of the standing-wave pattern. Intracavity n-contacts with electroplated gold posts are applied on the epitaxial side. Polyimide is used for chip planarization, as schematically illustrated in Fig. 1. The bottom-emitting laser contains a 30 pairs p-doped distributed Bragg reflector (DBR) and a 5 pairs n-doped DBR for wavelength selection. For laser operation, an external curved mirror with a radius of curvature approximately equal to the extended cavity length provides sufficient optical feedback and controls the output transverse modes. This dielectric mirror is coated for high reflectivity in the near-infrared range and is transparent for blue light emission. A lithium triborate (LBO) nonlinear optical crystal is inserted into the extended cavity close to the laser chip for frequency doubling. The VECSEL chip has dimensions of $1.7 \times 1.7\,\mathrm{mm}^2$ and is indium-soldered up-side down on a semi-insulating silicon heat spreader with metal traces for current supply. The heat spreader is soldered on a copper heat sink with indium as well. The applied mounting technique facilitates individual addressing of different lasers on one chip. Complete GaAs substrate removal significantly reduces the optical round-trip loss.

3. Measurement Results

The laser chips were first characterized in the infrared regime. Room temperature light–current–voltage curves of a EP-VECSEL with 68 µm active diameter are shown in Fig. 2. The external mirror has 10 mm radius of curvature and a reflectivity of 95 %. A threshold current of 64 mA and a differential quantum efficiency of 33 % are obtained. Optical CW output powers exceeding 50 mW are generated at emission wavelengths near 974 nm. A 4 mm long critically phase-matched antireflection-coated (970 and 485 nm) LBO crystal is then inserted for frequency doubling. Here, an external mirror with 20 mm radius of curvature and a reflectivity of 99.96 % at 980 nm wavelength is used. The output characteristics is plotted in Fig. 3 (left). The blue output power is measured after filtering out the remaining infrared light. A maximum CW output power of 1.7 mW at 145 mA

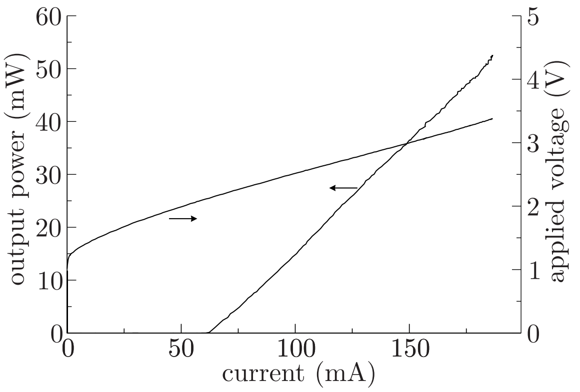

Fig. 2: CW operation characteristics of a 68 μm diameter EP-VECSEL with 10 mm cavity length emitting near 974 nm.

current is achieved, where a heat sink temperature of 10°C has been used to tune the laser wavelength towards higher SHG efficiency. Blue laser emission sets in at about 53 mA. A slight instability is observed around 100 mA and can be attributed to device heating and associated polarization switching [9], which influence the polarization-dependent critically phase-matched frequency conversion. Figure 3 (right) shows the spectrum of the laser, driven at 130 mA current. A narrow peak (0.1 nm spectral resolution) at an emission wavelength of 485 nm is observed with no side-modes.

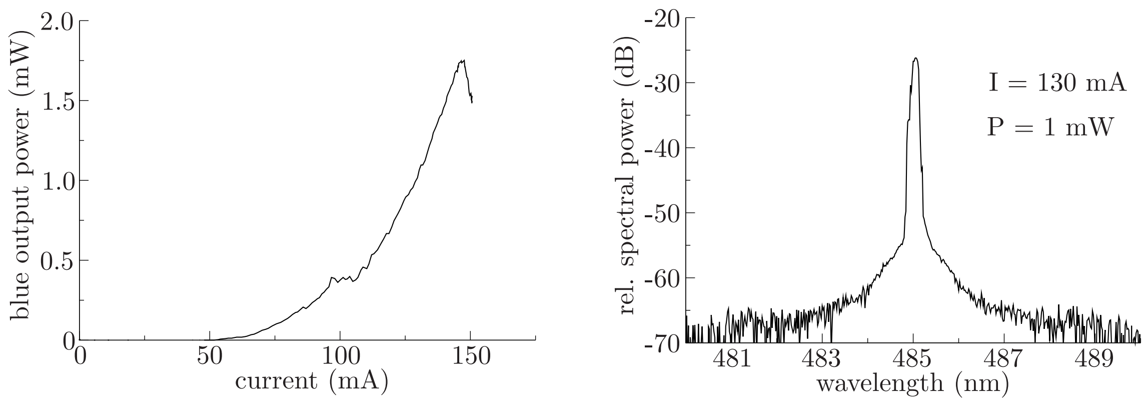

Fig. 3: Second-harmonic output characteristics of the frequency-doubled EP-VECSEL from Fig. 2 with a 20 mm long cavity (left) and the corresponding emission spectrum measured at 130 mA (right).

4. Conclusion

We have fabricated and characterized electrically pumped bottom-emitting InGaAs/GaAs VECSELs. Frequency doubling using a nonlinear optical crystal inside the extended cavity has been successfully performed. Blue light emission at 485 nm has been demonstrated with maximum CW output powers of 1.7 mW. Improvements such as noncritical phase matching and polarization control will lead to more stable and efficient SHG. Also higher performance can be expected using intracavity transparent heat sinks for more efficient cooling.

References

[1] M. Kuznetsov, F. Hakimi, R. Sprague, and A. Mooradian, "Design and characteristics of high-power (>0.5-W CW) diode-pumped vertical-external-cavity surface-emitting semiconductor lasers with circular TEM_{00} beams", *IEEE J. Select. Topics Quantum Electron.*, vol. 5, no. 3, pp. 561–573, 1999.

[2] J. Chilla, S. Butterworth, A. Zeitschel, J. Charles, A. Caprara, M. Reed, and L. Spinelli, "High power optically pumped semiconductor lasers", in *Solid State Lasers XIII: Technology and Devices*, R. Scheps, H.J. Hoffman (Eds.), Proc. SPIE 5332, pp. 143–150, 2004.

[3] S. Cho, G. Kim, J. Kim, K. Kim, S. Lee, J. Yoo, T. Kim, and Y. Park, "Compact and efficient green VECSEL based on novel optical end-pumping scheme", *IEEE Photon. Technol. Lett.*, vol. 19, no. 17, pp. 1325–1327, 2007.

[4] S. Hilbich, W. Seelert, V. Ostroumov, C. Kannengiesser, R. v. Elm, J. Müller, and B. Lübeck, "New wavelengths in the yellow orange range between 545 nm to 580 nm generated by an intracavity frequency-doubled optically pumped semiconductor laser", in *Solid State Lasers XVI: Technology and Devices*, H.J. Hoffman, R.K. Shori, N. Hodgson (Eds.), Proc. SPIE 6451, pp. 64510C-1–7, 2007.

[5] E. Gerster, I. Ecker, S. Lorch, C. Hahn, S. Menzel, and P. Unger, "Orange-emitting frequency-doubled GaAsSb/GaAs semiconductor disk laser", *J. Appl. Phys.*, vol. 94, no. 12, pp. 7397–7401, 2003.

[6] M. Hadley, G. Wilson, K. Lau, and J. Smith, "High single-transverse-mode output from external-cavity surface-emitting laser diodes", *Appl. Phys. Lett.*, vol. 63, no. 12, pp. 1607–1609, 1993.

[7] E. Strzelecka, J. McInerney, A. Mooradian, A. Lewis, A. Shchegrov, D. Lee, J. Watson, K. Kennedy, G. Carey, H. Zhou, W. Ha, B. Cantos, W. Hitchens, D. Heald, V. Doan, and K. Lear, "High power, high brightness 980 nm lasers based on the extended cavity surface emitting lasers concept", in *High-Power Fiber and Semiconductor Lasers*, M. Fallahi, J.V. Moloney (Eds.), Proc. SPIE 4993, pp. 57–67, 2003.

[8] J. McInerney, A. Mooradian, A. Lewis, A. Shchegrov, E. Strzelecka, D. Lee, J. Watson, M. Liebman, G. Carey, A. Umbrasas, C. Amsden, B. Cantos, W. Hitchens, D. Heald, and V. Doan, "Novel 980 nm and 490 nm light sources using vertical cavity lasers with extended coupled cavities", in *Vertical-Cavity Surface-Emitting Lasers VII*, C. Lei, S.P. Kilcoyne (Eds.), Proc. SPIE 4994, pp. 21–31, 2003.

[9] K. Choquette, and D. Richie, "Temperature dependence of gain-guided vertical-cavity surface emitting laser polarization", *Appl. Phys. Lett.*, vol. 64, no. 16, pp. 2062–2064, 1994.

Optical Particle Manipulation by Application-Specific Densely Packed VCSEL Arrays

Andrea Kroner

Densely packed arrays of vertical-cavity surface-emitting lasers (VCSELs) are presented, serving as low-cost and small-sized laser sources in optical particle manipulation systems. A novel, self-aligned fabrication process enables both a pitch in the 20 µm m range and a selective surface etch for enhanced transverse single-mode emission. Homogeneous array performance and single-mode output powers of up to 3.8 mW are observed. By inserting the arrays into an optical tweezers setup with external optics, multiple optical traps are easily created. Non-mechanical particle translation by switching between individually addressable devices as well as continuous particle deflection in a one-dimensional optical lattice are demonstrated.

1. Introduction

Optical particle manipulation by focused laser beams has become a key technology in biophotonics due to the possibility of damage- and contamination-free handling of microscopic biological material, such as living cells [1]. Here, the use of VCSELs as light sources has gained increasing interest owing to their high beam quality, low cost and small device dimensions [2–4]. Furthermore, VCSELs offer the unique possibility of a straightforward creation of multiple optical traps by using two-dimensional, monolithic laser arrays. Other methods, like holographic optical tweezers, are based on interference or splitting of a single laser beam and require expensive optics and critical adjustment [5]. With VCSEL-based multiple optical tweezers, simultaneous trapping of several cells was demonstrated [2], as well as stacking and non-mechanical translation of DNA bound to microbeads [3]. However, mainly standard VCSEL arrays designed for data communication have been applied so far, which have a large pitch of typically 250 µm and necessitate the use of additional microlens arrays. A different approach targets the drastic miniaturisation of the trapping setup by integrating a microlens directly on the VCSEL output facet, abandoning any external optics [4]. However, for this so-called integrated optical trap, the typical multimode output beam profile of VCSELs is inappropriate. The layout of densely packed VCSEL arrays for optical manipulation should therefore enhance transverse single-mode emission. This is efficiently achieved with the inverted surface relief technique, which uses a shallow, selective surface etch [4].

2. Fabrication

We have fabricated different two-dimensional arrangements of GaAs/AlGaAs-based top-emitting VCSELs with emission wavelengths in the 850 nm range. The inverted surface relief technique requires the upper p-doped mirror of the VCSEL structure to be terminated with an additional $\lambda/4$-antiphase layer. By removing the layer selectively only in the centre of the output facet, the threshold gain of the transverse fundamental mode can be preferentially reduced, leading to enhanced single-mode emission. However, an exact overlap of the shallow relief and the active laser aperture is mandatory. Furthermore, aspired array pitches of about 20 µm and gaps of only 2 µm between the devices require steep, dry etched mesa sidewalls. Therefore, a novel fabrication process has been developed, based on multiple resist layers (Fig. 1). To achieve self-alignment, relief and p-contact ring are both structured within the first exposure step and are contained as openings in an otherwise closed layer of PMGI (polymethylglutarimide) resist (Fig. 1a). During wet etching of the surface relief, the p-contact area is protected by a novolak-based resist, requiring only low alignment accuracy (Fig. 1b). Afterwards, this layer can be selectively removed by acetone, thus restoring the initial resist structure(Fig. 1c). For p-contact metallisation, the relief is protected likewise and the subsequent lift-off step removes all resist layers (Fig. 1d-f). Finally, the VCSEL output facet is protected by resist and the p-contact metal serves as stable hard mask for reactive ion etching of the mesa (Fig. 1g–h), such that the following oxidation step leads to a self-aligned oxide aperture. On the left side of Fig. 2, a scanning electron microscope (SEM) image of an array with 24 µm pitch and 3.4 µm surface relief diameter is presented, showing almost vertical mesa edges and exact alignment of mesa, p-contact ring and surface relief. The process is completed by surface passivation and bondpad metallisation. The right side of Fig. 2 shows an optical microscope image of a finished array of standard top-emitting devices. Here, no relief is etched but the antiphase-layer is completely removed.

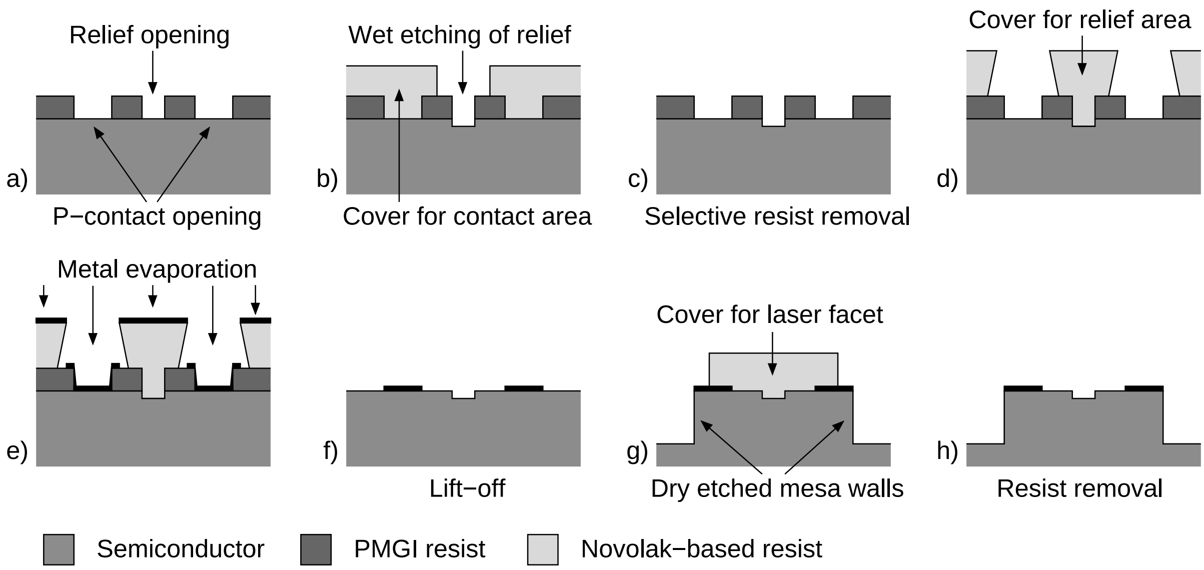

Fig. 1: Novel fabrication process to achieve self-alignment of relief, p-contact ring and mesa.

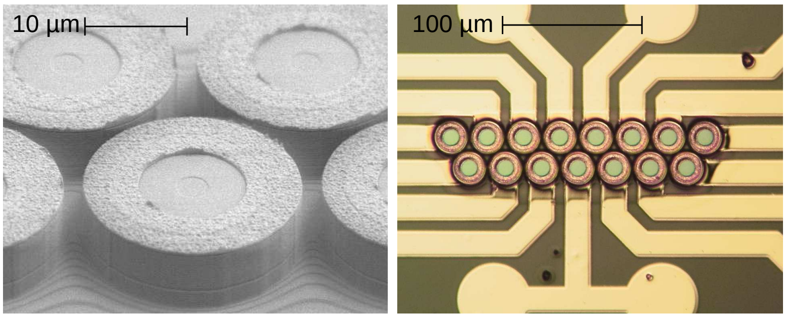

Fig. 2: SEM image (left) and optical microscope image (right) of densely packed VCSEL arrays with 2 µm mesa gap.

3. Experimental Results

Figure 3 presents the operation characteristics of 15 individually addressable devices from a VCSEL array with 8 µm diameter oxide apertures according to Fig. 2 (right). Threshold currents of around 1.6 mA and maximum multimode output powers of about 8 mW with only minor variations are observed. In the optical tweezers setup [4], the output beams of the lasers are tightly focused by an immersion objective with a high numerical aperture of 1.25, creating an individually addressable tweezers array in the sample stage with a pitch of about 5.5 µm. Figure 4 shows sequences of the experiment as top views on the sample stage, which contains polystyrene particles with a diameter of 10 µm solved in water. A partial image of the VCSEL array can be seen, indicating the position of the optical tweezers. In Fig. 3a, the VCSEL in the lower left corner is emitting, trapping a particle in its beam with an optical power of about 2.1 mW at the sample stage. When switching to an adjacent device, the sphere follows the maximum of light intensity (Figs. 4a–d). After 1.5 s, the particle is moved non-mechanically by about 16 µm to the upper right trap of the array (Fig. 4d). Obviously, this scheme can be extended to laser arrays with a much higher number of elements.

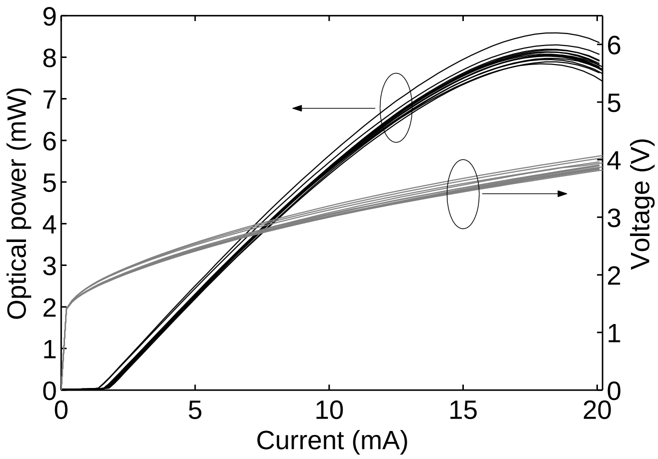

Fig. 3: Operation characteristics of an array containing 15 individual VCSELs without relief and an active diameter of 8 µm (according to Fig. 2 (right)).

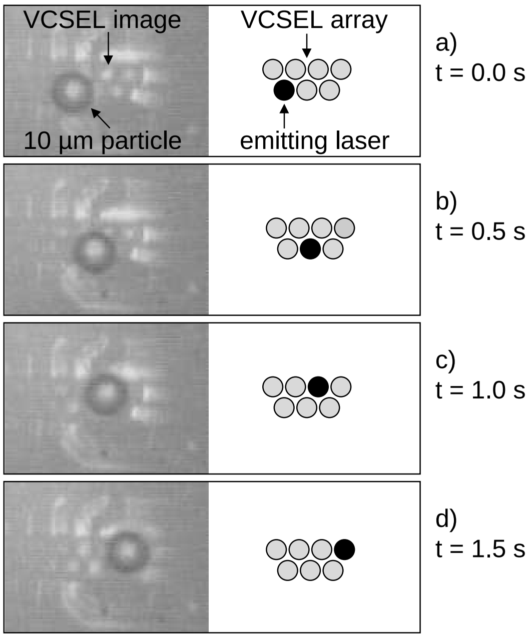

Fig. 4: Non-mechanical translation of a 10 µm particle by switching between adjacent lasers. Sequences of the experiment are shown as top views on the sample stage (left) and schematically to highlight the emitting laser in the array (right).

Furthermore, the high-density arrays are employed for continuous optical particle deflection, which is of particular interest for particle handling and sorting in microfluidics. Here, a linear tweezers array is used to create a one-dimensional optical lattice. A particle passing the tilted lattice will not be stopped by a single trap, but piecewise deflected [6, 7]. Since an individual addressing of lasers is not required in this operation scheme, also arrays with devices connected in parallel were fabricated in order to decrease the number of contacts significantly. Figure 5 shows the light versus current curve of three jointly lasing devices, which have a 6 µm wide oxide aperture and 3.4 µm relief diameter. A mean threshold current of 1.7 mA and a high maximum output power of 3.8 mW per device can be deduced. Figure 6 presents the three optical spectra at thermal rollover, revealing single-mode emission with a side-mode suppression ratio above 30 dB owing to the mode-selective effect of the surface relief. In Fig. 7, optical particle deflection using a similar array with six simultaneously emitting devices and an optical power of 6.4 mW in the sample plane is demonstrated. For this purpose, the laser chip is again inserted as laser source into the optical tweezers setup and by tightly focusing the output beams with external optics, an optical lattice is created in the sample plane. A 10 µm polystyrene microsphere is moved from left to right with a velocity of 25 µm/s by a computer-controlled positioning system connected to the sample stage (Figs. 7a–b). While passing the optical lattice, the particle follows the 21° tilt of the array (Figs. 7b–e) and is eventually deflected by a total distance of about 18 µm orthogonal to its initial flow direction (Fig. 7f). Beyond a certain maximum tilt of about 30°, which also depends on the particle velocity, deflection was no longer possible.

4. Conclusion

By using densely packed VCSEL arrangements, multiple optical tweezers are easily created in a straightforward manner. A novel fabrication process does overcome the limitations

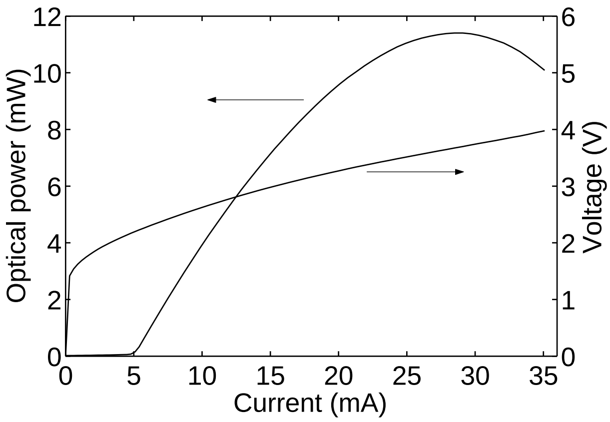

Fig. 5: Operation characteristics of three relief VCSELs driven in parallel with a 6 µm wide oxide aperture and 3.4 µm relief diameter.

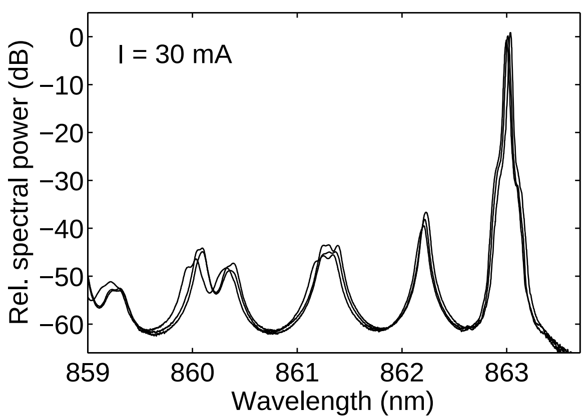

Fig. 6: Optical spectra of the three relief VCSELs presented in Fig. 5 at 30 mA driving current.

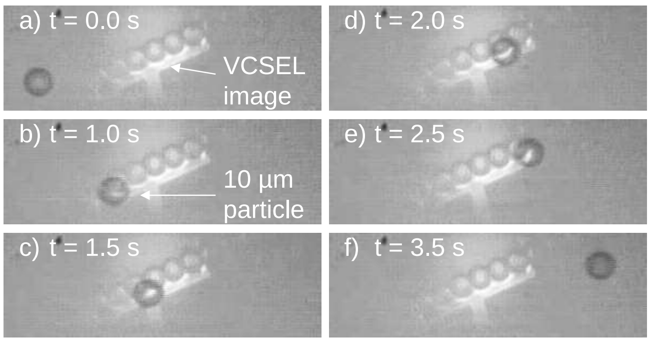

Fig. 7: Continuous deflection of a passing particle by a tilted VCSEL array. The 10 µm polystyrene microsphere is moved from left to right with a velocity of 25 µm/s and is eventually deflected by a total distance of about 18 µm orthogonal to its initial flow direction.

of standard VCSEL arrays and seamlessly integrates the surface relief technique for enhancement of single-mode emission. Non-mechanical translation as well as continuous particle deflection are demonstrated, where for the latter, a dependence on the geometric and material properties of the particle is to be expected [6, 7]. Therefore, applications in microfluidic particle sorting are intended as well as a further miniaturisation towards the integrated optical trap, where the laser array will be in direct contact to the sample plane [4].

5. Acknowledgement

We wish to thank the German Research Foundation (DFG) for financial support.

References

[1] K. Dholakia, P. Reece, and M. Gu, "Optical micromanipulation", *Chem. Soc. Reviews*, vol. 37, pp. 42–55, 2008.

[2] R.A. Flynn, M. Birkbeck, M. Gross, M. Ozkan, B. Shao, M.M. Wang, and S.C. Esener, "Parallel transport of biological cells using individually addressable VCSEL arrays as optical tweezers", *Sensors and Actuators B*, vol. 87, pp. 239–243, 2002.

[3] Y. Ogura, T. Beppu, F. Sumiyama, and J. Tanida, "Toward photonic DNA computing: developing optical techniques for parallel manipulation of DNA", in *Photonics for Space Environments X*, E.W. Taylor (Ed.), Proc. SPIE 5897, pp. 34–43, 2005.

[4] A. Kroner, J.F. May, I. Kardosh, F. Rinaldi, H. Roscher, and R. Michalzik, "Novel concepts of vertical-cavity laser-based optical traps for biomedical applications", in *Biophotonics and New Therapy Frontiers*, R. Grzymala, O. Haeberlé (Eds.), Proc. SPIE 6191, pp. 269–280, 2006.

[5] J.E. Curtis, B.A. Koss, and D.G. Grier, "Dynamic holographic optical tweezers", *Optics Communications*, vol. 207, pp. 169–175, 2002.

[6] M.P. MacDonald, G.C. Spalding, and K. Dholakia, "Microfluidic sorting in an optical lattice", *Nature*, vol. 4, pp. 421–424, 2003.

[7] M. Pelton, K. Ladavac, and D.G. Grier, "Transport and fractionation in periodic potential-energy landscapes", *Phys. Rev. E*, vol. 70, pp. 031108-1–10, 2004.

Si-doped GaN by Hydride-Vapour-Phase-Epitaxy Using a Ga:Si-Solution as Doping Source

Frank Lipski

The Si-doping of GaN by hydride vapour phase epitaxy (HVPE) has been analyzed. To this end, a Ga:Si-solution was employed as Si source. Doping concentrations of up to $9 \cdot 10^{18}\,cm^{-3}$ could be achieved. By using a second pure Ga-source, a systematic variation of the doping level was possible. Although there is a high tendency to cracking in Si-doped GaN, a layer-thickness of more than $10\,\mu m$ could be achieved by the insertion of a SiN-interlayer in the MOVPE-grown templates.

1. Introduction

Currently the epitaxy of GaN-based devices has to be done on foreign substrates, such as sapphire or SiC. A high defect density arises in these devices, because of the high lattice mismatch of the foreign materials compared to GaN, which limits the overall device performance regarding efficiency and lifetime [1]. Although there are a lot of efforts using techniques like ELO or SiN-interlayer [2] to reduce the defect density during the heteroepitaxy, only homoepitaxial growth can overcome this problem and improves the defect situation drastically. For the production of the finally needed free-standing GaN-substrates the hydride vapour phase epitaxy seems to be the most promising way besides other approaches like growth from solution or supercritical ammonia. Additionally, for the production of optoelectronic devices like LEDs and laser-diodes, n-doped GaN-substrates are desired, in order to realize backside-contacts. Therefore we investigated the Si-doping during the HVPE process for future free-standing n-doped GaN-substrates.

There are a lot of possibilities for the choice of the Si doping source in HVPE. First, like commonly used in MOVPE, gaseous sources such as SiH_4 may be considered. However, SiH_4 exhibits a strong thermal instability and decays rapidly in the HVPE process before arriving at the substrate. Therefore it has to be discarded. Alternatively, chlorosilanes may be used, because of their higher thermal stability. Doping of GaN with HVPE and SiH_2Cl_2 was achieved with good material quality [3]. Another approach, which makes the additional gas-channel dispensable, is the use of solid Si, which forms $SiHCl_3$ when exposed to the HCl stream. At high temperatures, it decays into $SiCl_2$ which is then transported to the growth zone. Due to changes in the morphology of the used Si-piece, this method is difficult in controllability and reproducibility [3] [4]. To avoid this problem, we solved a piece of Si in a Ga bath and used it as Ga and Si source simultaneously.

2. Experimental

All growth experiments were done in a commercial Aixtron single-wafer HVPE system with a horizontal quartz-tube, heated in a furnace with five zones. Nitrogen was used as carrier-gas while H_2 was also added into the reactor for the reduction of cracking [5]. As nitrogen precursor, ammonia was applied, while for the group-III element a liquid Ga-bath was arranged in a HCl-stream, so that the formation of GaCl occurred and was directly injected above the substrate. In our system, two identical channels of this type were available. The substrate temperature was adjusted to 1050° C while the Ga-sources were kept at 850° C. The reactor-pressure was set to 900 mbar during these experiments.

In one of the two available source channels, 1 g Si was solved in 200 g Ga, corresponding to a molar fraction of 2.4 %. The second source channel contained a pure Ga source. Growth could be done with either one of the channels or both in combination.

The doping concentration was measured by secondary ion mass spectroscopy (SIMS) for the highest doped samples and by room-temperature Hall measurements. The crystal quality was analyzed by high-resolution x-ray diffraction (HRXRD) and by low temperature ($T = 4\,\mathrm{K}$) photoluminescence (PL).

For these studies, we used GaN templates grown in an Aixtron 200/4 RF-S system on (0001) sapphire substrates with a slight misorientation to the a-plane [6]. For the growth of the templates, an AlN nucleation layer was deposited at a temperature of 900° C and covered with a GaN-layer of about 1.6 µm. In some templates, a SiN-interlayer was deposited after the nucleation and a thin GaN-buffer.

3. Results and Discussion

First attempts where the HVPE growth was only done with the Ga:Si solution channel led to a partly passivated template due to the unintentional deposition of a thin SiN layer obviously blocking the further GaN-growth. Only the growth of some GaN islands happened, but no closed layer could be achieved (Fig. 1).

We suppose that the Ga:Si solution develops a very high Si concentration on the surface during heat-up of the reactor. When switching on the HCl gas flow, mainly SiCl is formed instead of otherwise dominating GaCl which then leads to the strong SiN deposition on the wafer. After short time (about one minute), the high Si concentration is removed from the source surface by the flowing HCl. However, owing to the partial masking of the surface by SiN only GaN islands can develop. Unfortunately, a prerun of HCl over the source without insertion of the formed SiCl into the reactor is not possible in our system.

By starting the growth with the second pure Ga source channel and then ramping over to the other channel, this problem could be solved allowing the growth of closed GaN layers.

Using only the doping channel for the main growth, samples with a doping concentration up to $9 \cdot 10^{18}\,\mathrm{cm}^{-3}$, as measured by SIMS, could be achieved. Room-temperature Hall-measurements showed also carrier-concentrations of $9 \cdot 10^{18}\,\mathrm{cm}^{-3}$ with a mobility of $167\,\mathrm{cm}^2/\mathrm{Vs}$. Obviously complete electrical activation of the incorporated Si could be achieved.

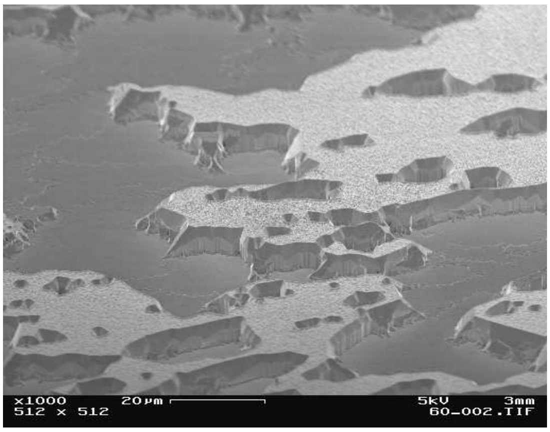

Fig. 1: SEM picture of the partly passivated surface, if growth is started directly with the doping channel.

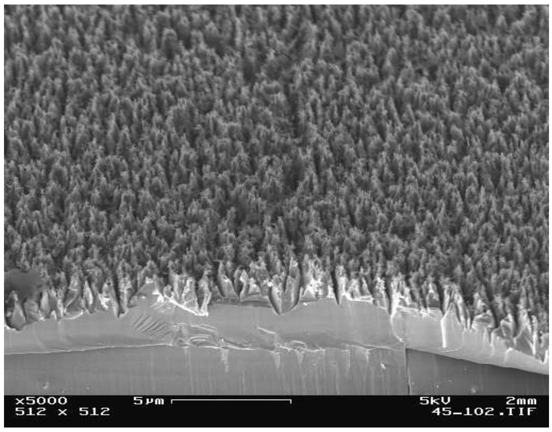

Fig. 2: SEM picture of the etched surface due to the reduction of the V/III-ratio at the growth end.

In these experiments, we discovered a decrease of the growth-rate by a factor of about 5 as compared to undoped growth. Although this reduction may be partly caused by the slightly different position of our doping shower head with respect to the substrate, we suppose that at least a factor of 4 is caused by a reduced efficiency of the GaCl formation on the Ga:Si solution.

The x-ray rocking curve of the (0002) reflection exhibits only a comparably small broadening from 217 arcsec to 277 arcsec from undoped to the doped sample (Fig. 3). Similarly, the low temperature donour-bound exciton PL peak broadened from 1.6 meV to 6.3 meV (Fig. 4). On our standard templates, the sample thickness was limited to about 10 μm, because for higher thicknesses the appearance of cracks was discovered with increasing density. Such behaviour is typical for highly Si-doped layers [7]. Such cracking could be drastically reduced by using MOVPE-templates containing a SiN-interlayer, as described in section 2.. These templates have stronger compressive strain on the surface reducing the probability of crack-formation substantially, not only for undoped growth, but also in the case of Si-doping.

3.1 Surface morphology

For optimization of the surface morphology, we have developed a 2-step growth procedure for undoped layers [8]. This process is mainly characterized by a reduction of the V/III-ratio and the pressure for the growth of the last few micrometers. Adopting this to the growth with the Ga:Si solution yielded in a rough, etched surface, as it is shown in Fig. 2. Therefore this procedure had to be skipped for the Si-doped growth.

3.2 Variable doping concentration

In order to vary the doping concentration, the HCl-flow was split between the two growth-channels with a variable ratio, while the total HCl flow was kept constant. This method

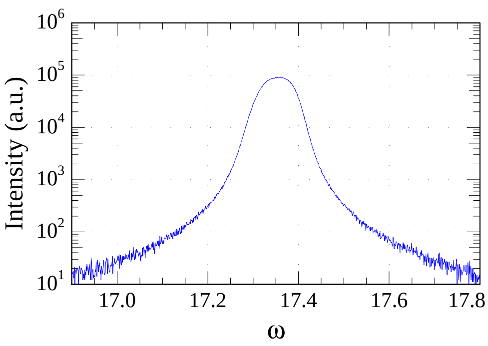

Fig. 3: HRXRD-measurement of (0002) reflection of the highly doped sample.

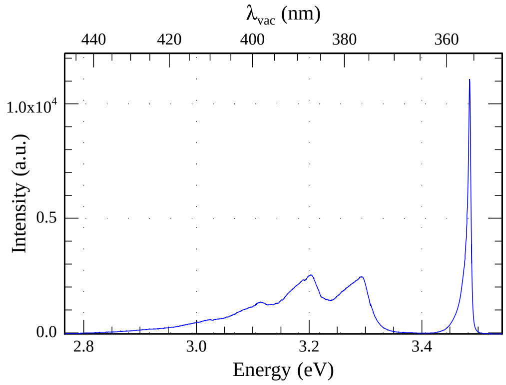

Fig. 4: Low-temperature PL-spectrum of the highly doped sample with a carrier density of $9 \cdot 10^{18}\,\mathrm{cm}^{-3}$

allowed the adjustment of the doping level from $5 \cdot 10^{16}\,\mathrm{cm}^{-3}$ to $9 \cdot 10^{18}\,\mathrm{cm}^{-3}$, while the mobility decreased from 600 to $180\,\mathrm{cm}^2/\mathrm{Vs}$. Moreover a continuous decrease in the growth rate with increasing doping concentration was found. Figure 5 shows the doping concentration and the mobility as a function of the fraction of the HCl flow in the doping channel. Low temperature PL-measurements showed a broadening of the FWHM of the D^0X-peak and a shift of its energy with increasing doping-concentration, see Fig. 6 confirming the increasing tensile strain induced by the Si doping.

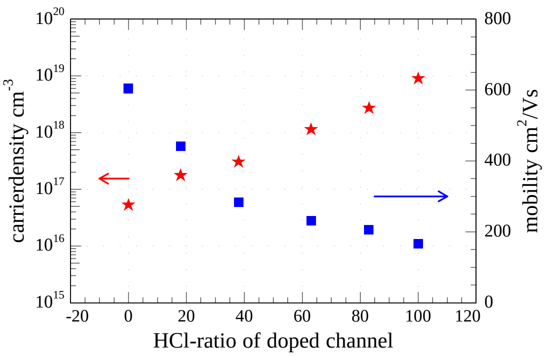

Fig. 5: Carrier-concentration (stars) and mobility vs. ratio of HCl-flow in percent through doped and undoped showerhead.

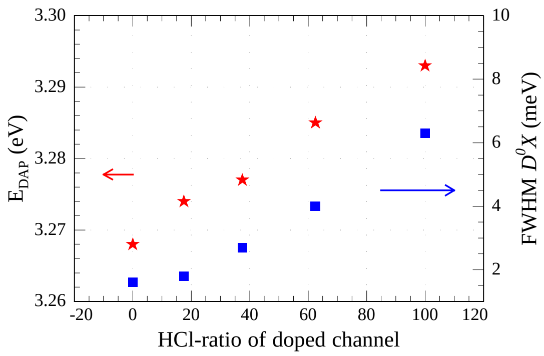

Fig. 6: Low-temperature (4 K) PL-measurements. Position of the donor-bound-exciton peak (stars) and its FWHM.

3.3 Homogeneity

The experiments with variable doping concentrations also revealed a specific problem of the used reactor geometry: Owing to the slightly different alignment of the two source channels, an inhomogenous radial doping profile develops. Furthermore, as a consequence of the high growth rate in HVPE and the comparably low rotation speed of the substrate, the samples end up with a doping modulation profile in growth direction due to the locally periodic supply of undoped and doped source gases. These difficulties must be taken into account, if growth with varied doping level and only one Ga:Si source with constant Si fraction is desired.

3.4 Stability of the source

While the doping-source was stable during the executed growth experiments, it showed a slow decomposition with high Si-concentrations on the surface. This required already, that the growth start had to be down with the undoped channel and then ramped to the other. The possibility of further decomposition can not be neglected.

4. Conclusion

We have investigated a new doping-source for Si-doping in the HVPE. The use of a Ga:Si solution is a simple approach and we achieved doping concentrations up to $9 \cdot 10^{18}\,\mathrm{cm}^{-3}$. The samples showed fairly good quality with a FWHM of the (0002)-reflection in HRXRD of 277 arcsec and of the D^0X-peak in PL of 6.3 meV. The stability of the source was acceptable for the experimental series of some weeks, but showed already a small decomposition. The behaviour with longer operation time with many heat-up and cool-down cycles is still questionable. With the presented source-type, a variation of the doping-concentration is also possible, requiring however a well adjusted reactor geometry for a homogeneous doping profile.

Acknowledgement

We would like to thank M. Feneberg of the Institute of Semiconductor Physics of Ulm University for PL-measurements and “Fraunhofer-Institut für Angewandte Festkörperphysik” in Freiburg for SIMS-measurements. We also gratefully acknowledge financial support by Freiberger Compound Materials GmbH and “Sächsisches Ministerium für Wirtschaft und Arbeit (SMWA)” (contract 10603).

References

[1] T. Sugahara, H. Sato, M. Hao, Y. Naoi, S. Kurai, S. Tottori K. Yamashita, K. Nishino, L.T. Romano, S. Sakai, "Direct Evidence that Dislocations are Non-Radiative Recombination Center in GaN", *Jap. J. Appl. Phys.*, vol. 37, pp. L398–L400, 1998

[2] M.J. Kappers, R. Datta, R.A. Oliver, F.D.G. Rayment, M.E. Vickers, C.J. Humphreys, "Threading dislocation reduction in (0001) GaN thin films using SiN_x interlayers", *J. Crystal Growth*, vol. 300, pp. 70–74, 2007

[3] E. Richter, Ch. Henning, U. Zeimer, L. Wang, M. Weyers, and G. Tränkle, "N-type doping of HVPE-grown GaN using dichlorsilane", *phys. stat. sol. (a)*, vol 203, pp. 1658–1662, 2006.

[4] A.V. Fomin, A.E. Nikolaev, I.P. Nikitina, A.S. Zubrilov, M.G. Mynbaeva, N.I. Kuznetsov, A.P. Kovarsky, B.Ja. Ber, and V. Tsvetkov, "Properties of Si-Doped GaN Layers Grown by HVPE", *phys. stat. sol. (a)*, vol 188, pp. 433–437, 2001.

[5] E. Richter, Ch. Henning, M. Weyers, F. Habel, J.-D. Tsay, W.-Y. Liu, P. Brückner, F. Scholz, Yu. Makarov, A. Segal, J. Kaeppeler, "Reactor and growth process optimization for growth of thick GaN layers on sapphire substrates by HVPE", *J. Crystal Growth*, vol. 277, pp. 6–12, 2005

[6] F. Scholz, P. Brückner, F. Habel, M. Peter, K. Köhler, "Improved GaN layer morphology by hydride vapor phase epitaxy on misoriented Al_2O_3 wafers", *Appl. Phys. Lett.*, vol. 87, p. 181902, 2005

[7] L.T. Romano, C.G. Van de Walle, B.S. Krusor, R. Lau, J. Ho, T. Schmidt, J.W. Ager III, W. Göetz, R.S. Kern, "Effect of Si doping on the strain and defect structure of GaN thin films", *Physica B*, vol 273, pp. 50–53, 1999.

[8] P. Brückner, F. Habel, F. Scholz, "HVPE growth of high quality GaN layers", *phys. stat. sol. (c)*, vol. 3, pp. 1471–1474, 2006

[9] A. Cremades, L. Görgens, O. Ambacher, M. Stutzmann, F. Scholz, "Structural and optical properties of Si-doped GaN", *Phys. Rev. B*, vol. 61, pp 2812–2818, 2000.

[10] G. Valente, C. Cavallotti, M. Masi, S. Carra, "Reduced order model for the CVD of epitaxial silicon from silane and chlorosilanes", *J. Crystal Growth*, vol. 230, pp. 247–257, 2001.

[11] R.N. Linnebach "Anomaly in the Ga-Si phase diagram: Nonretrograde solubility of Ga in Si layers grown by liquid epitaxy", *J. Appl. Phys.*, vol. 67, pp. 6794–6797, 1990.

Highly Conductive Modulation-Doped Graded p-AlGaN/(AlN)/GaN Multi-Heterostructures

Joachim Hertkorn and Zhihao Wu†

In this study we present theoretical and experimental results regarding modulation doped p-AlGaN/(AlN)/GaN multi-heterostructures. As the heterostructures should yield both, higher lateral and better vertical conductivity than p-doped GaN, band structure simulations have been performed prior to growth experiments. Based on the simulation results several samples were grown by metalorganic vapor phase epitaxy (MOVPE). High resolution X-ray diffraction was used to determine the effective Al-concentration as well as the period length of the multi-heterostructures. The electrical properties of the samples were investigated by measuring the lateral (σ_L) and vertical (σ_V) conductivity. Moreover electron holography measurements were performed to determine the profile of the valence band. The free hole concentration of a sample optimized in terms of lateral conductivity was measured to be $5.5\times10^{18}\,cm^{-3}$ (295 K) with a mobility of $12\,cm^2/Vs$, yielding a σ_L of $10\,(\Omega cm)^{-1}$. Low temperature Hall measurements (77 K) proved the existence of a 2DHG at the AlN/GaN interface, as the lateral conductivity could be increased to $25\,(\Omega cm)^{-1}$. By substituting the p-GaN layer in a light emitting diode (LED) with an AlGaN/GaN multi-heterostructure optimized in terms of vertical conductivity, the overall voltage drop could be reduced by more than 100 mV ($j = 65\,A/cm^2$), clearly demonstrating that p-type heterostructures are a candidate to increase the efficiency of high brightness LEDs.

1. Introduction

The research on the III-nitride based technology has developed tremendously during the last few years, yielding a commercialization of many AlGaInN-based devices in several areas. Although the performance of many of those devices is already very impressive, one limiting factor remains the low conductivity of p-type GaN. Due to the relatively high ionization energy of Mg in GaN (170 meV), one has to incorporate very high densities of Mg ($10^{19}\,\mathrm{cm}^{-3}$) to achieve reasonable hole concentrations of $\geq 10^{17}\,\mathrm{cm}^{-3}$ (295 K). This low hole concentration leads to poor Ohmic contact resistances and a high series resistance of GaN based laser diodes and light-emitting diodes. The high resistivity increases the operating voltage and prevents high driving currents finally limiting the efficacy of the brightest LEDs. At meantime the current spreading in p-GaN layers is limited by the low conductivity also influencing the extraction efficiency of high brightness LEDs. To overcome such problems, the growth of modulation doped p-AlGaN/(AlN)/GaN superlattices

†Z. Wu is with the Dept. of Physics, Arizona State University, Tempe, Arizona 85287-1504, USA

is of interest, as high effective hole concentrations of $\geq 10^{18}\,\mathrm{cm}^{-3}$ are achievable in such heterostructures [1–4]. Hereby the strong polarization along the c axis of the GaN crystal and its alloys yields the formation of two-dimensional hole gases at the AlGaN/GaN interface. As the discontinuities of the valence band play an important role regarding this mechanism, the ionization of the Mg atoms is expected to be pushed further by implementing a thin AlN (E_g=6.1 eV) layer at the AlGaN/GaN interface. However the vertical resistivity of such superlattices cannot be neglected, as the use of AlN yields a strong potential barrier for the holes regarding the valence band profile.

2. Band Structure Simulation

To get a better understanding how the AlN might influence the vertical conductivity, we performed band structure calculations by using a classical Schrödinger-Poisson-solver [9] also calculating the local carrier distribution in AlGaN/AlN/GaN heterostructures taking into account the polarization field of the nitride based semiconductors. To keep the influence of the AlGaN on the vertical conductivity as small as possible, we performed simulations with graded Al composition in the AlGaN layer, as proposed by Heikman and Kauser et al. [10, 11]. For all simulations the AlGaN region was assumed to be Mg doped with an atom concentration of $1 \times 10^{19}\,\mathrm{cm}^{-3}$, whereas a background Mg concentration of $5 \times 10^{18}\,\mathrm{cm}^{-3}$ was applied for the nominally undoped GaN.

Based on the results obtained for n-type heterostructures [12] we first carried out simulations without an AlN interlayer at the AlGaN/GaN interface (Fig. 1, left). In such simulations the AlGaN layer was separated into one part with constant Al concentration (AlGaN-barrier) and a second part (20 nm) with a varying Al composition from 0 % near the GaN to 20 % near the AlGaN-barrier. Keeping the period length stable, the GaN and AlGaN-barrier dimensions were varied from 5 nm to 10 nm and 5 nm to 0 nm, respectively.

As the polarization charges are distributed homogeneously over the composition graded region the smooth valence band profile was found to be independent of the AlGaN-barrier thickness (Fig. 1, left). Neglecting this layer it was possible to reduce the period length and the effective Al concentration of the multi-heterostructure, yielding a higher specific

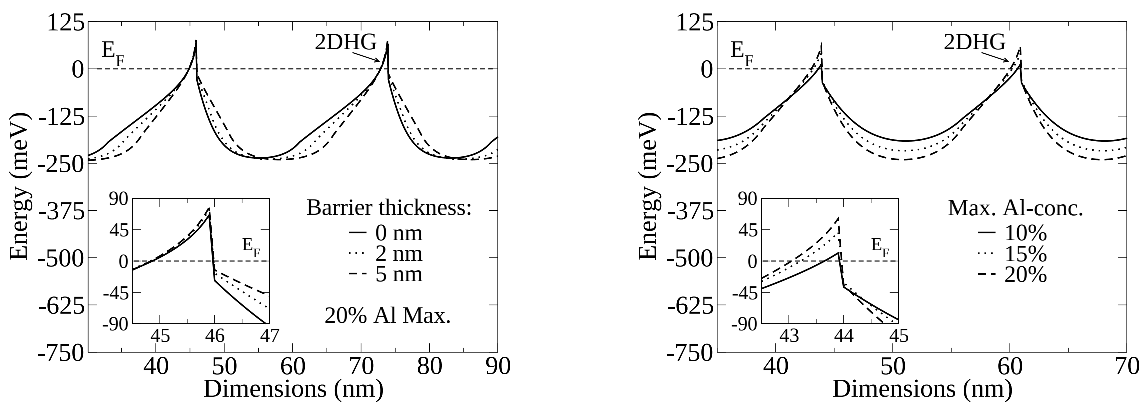

Fig. 1: Influence of the AlGaN-barrier width (left) and the overall Al concentration (right) on the potential profile of the valence band.

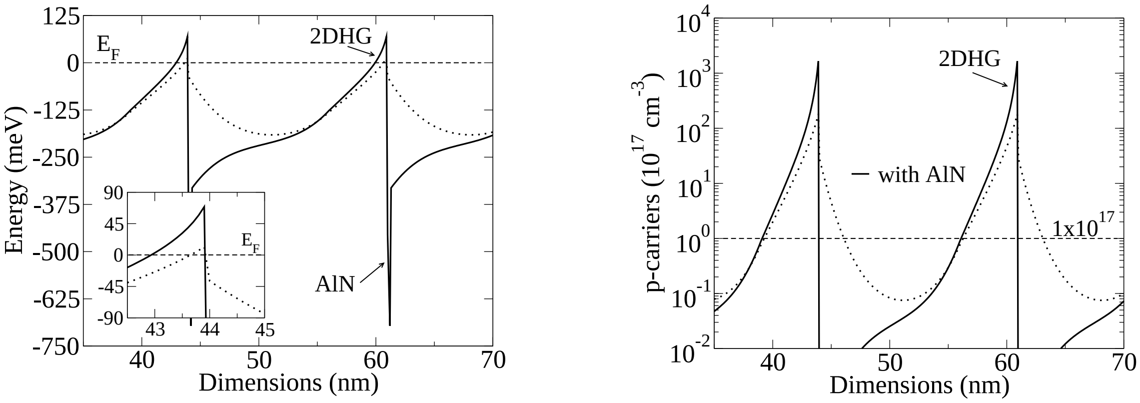

Fig. 2: Band diagram of a structure optimized in terms of lateral conductivity (solid line) and vertical conductivity, respectively.

lateral conductivity and improved strain situation, respectively. The potential barrier of $\approx$ 250 meV in such structures with 20 % Al is expected to have only suboptimal properties in terms of vertical conductivity [10–12]. Therefore simulations were carried out with a reduced Al concentration in the composition graded AlGaN (Fig. 1, right). If the maximum aluminum concentration at the AlGAN/GaN interface was set to 10 % the barrier height was reduced to values of $\approx$ 175 meV (Fig. 1, right, solid line) what should influence the vertical conductivity positively. For the later on performed growth experiments we finally defined such a structure of 12 nm composition graded AlGaN (0 % to 10 %) and 5 nm nominally undoped GaN as the so called "best-vertical" multi-heterostructure.

As the 2DHG carrier concentration is supposed to be negatively influenced by the reduced Al concentration (Fig. 1, right, magnified part) we continued the band structure simulations on "best-vertical" structures including an AlN interlayer ($\approx$ 3 Å) at the AlGaN/GaN interface (Fig. 2, left) finally yielding the so called "best-lateral" structure. The thin interlayer is compensating the disadvantages of the "best-vertical" sample in terms of lateral conductivity, as it can be easily seen in the magnified part in Fig. 2 (left). Using AlN as interlayer, the band discontinuities in the 2DHG region are much stronger (solid line), yielding a higher ionization of acceptors. Thus the carrier concentrations in structures with AlN can be calculated (Fig. 2, right) as high as $5 \times 10^{18}\,\mathrm{cm}^{-3}$ (295 K) whereas the "best-vertical" structure only yields values of $1 \times 10^{18}\,\mathrm{cm}^{-3}$ (295 K). Unfortunately the AlN is expected to be strongly negative for the vertical current flow, as the maximum barrier height is reaching values of about 700 meV.

3. Experimental

Based on the simulation results we worked on optimizing the growth of such low Al containing ($x_{Al} \approx 10\,\%$) and Al graded modulation doped heterostructures with periods of 17 nm by MOVPE. The growth experiments were performed in an AIXTRON 200/RF-S horizontal flow system. The layers were grown on 2" c-plane (0001) epi-ready sapphire wafers slightly miscut by about 0.3° towards the a-plane using an oxygen doped AlN nucleation layer (NL) [5,6]. The process temperature was controlled with a fiber coupled pyrometer faced to the backside of our rotation tray. All growth temperatures mentioned below are not the real substrate temperatures but the read-out of this pyrometer. Before deposition, the substrates went through in-situ annealing [7] at 1150 °C for 10 min in a hydrogen atmosphere. After the deposition of the NL (≈ 20 nm) and a buffer of around 750 nm undoped GaN, the p-type multi-heterostructures have been grown at a temperature of 1045 °C and a total thickness of around 200 nm. The growth of all layers was performed at a reduced reactor pressure of 100 mbar with the standard precursors trimethyl-aluminum (TMAl), trimethyl-gallium (TMGa), and high purity ammonia (NH_3). As p-type dopant source biscyclopentadienylmagnesium (Cp_2Mg) was applied. The carrier gas was Pd-diffused hydrogen.

The lateral conductivity of the samples was investigated using temperature dependent Van-der-Pauw Hall measurements. To get informations about the implemented amount of Mg atoms, secondary ion mass spectroscopy (SIMS) measurements have been performed. Hence a clear answer could be given how efficient the acceptor ionization in different structures was. To get a feeling for the vertical conductivity of the multi-heterostructures, we grew LEDs with p-type heterostructures in stead of conventional p-GaN and investigated the voltage drop at certain current densities.

The crystallographic properties of the layers were investigated using high resolution X-ray diffraction (HRXRD) and transmission electron microscopy (TEM). To get further informations about the resulting electrostatic potential energy profile of our grown heterostructures we also performed electron holography studies similarly as on our n-type heterostructures [8].

4. Electron Holography

Electron holography is a powerful technique based on TEM to determine the spatial distribution of electrostatic potential with sub-nanometer resolution. For the investigation, performed at the Arizona State University (USA), cross-sectional samples were prepared for electron microscopy using standard mechanical polishing and argon-ion milling techniques. We used a field-effect transmission electron microscope equipped with an electrostatic biprism and operated with incident electron beam energy of 200 keV. Figure 3 (left) shows the phase and amplitude images extracted from a high resolution electron hologram. Due to the limitations in the experimental setup, only the top three periods adjacent to the surface of the heterostructure could be sampled. The electrostatic potential energy profile derived from the phase image is shown on the right hand side of Fig. 3 assuming an electron free mean path of 61 nm for GaN. The boundaries of different regions are carefully determined by a close match with the contrast in the phase image. The 2DHG region occurs at the immediate right of the AlN layer, with a positive curvature and energy rise of ≈ 0.3 eV. In the graded AlGaN layer, the potential energy has an overall negative curvature that may be due to the nonlinear grading of the Al composition in the AlGaN layer and/or to a net negative charge density. The charge density in the AlGaN is a sum of two components: the negative (ionized) acceptor density N_A^- in the AlGaN and the polarization charge density, due to the gradient in polarization associated with the Al compositional grading. In addition, many tiny bumps with negative

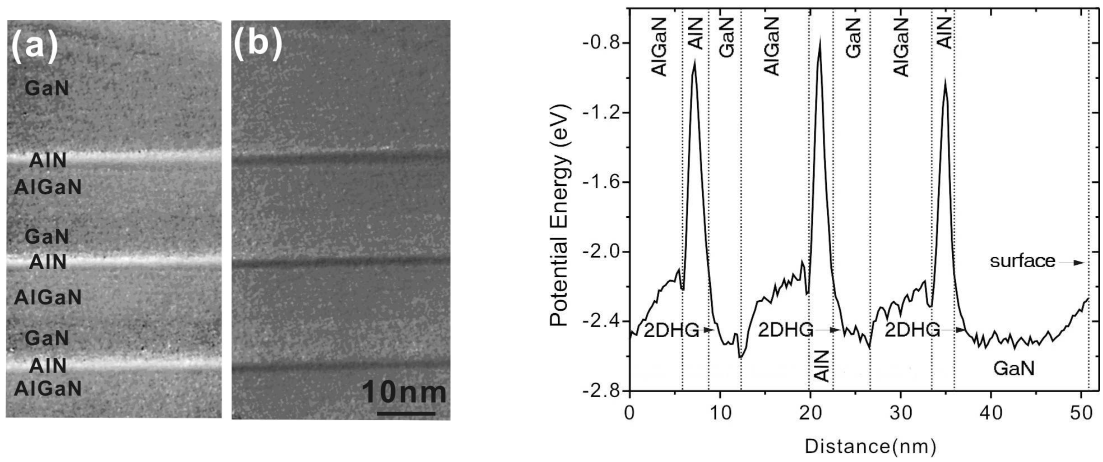

Fig. 3: Phase (a) and amplitude image (b) of a "best-lateral" heterostructure extracted from an electron hologram (left). Potential energy profile across the multi-heterostructure (right), derived from (a) and (b), assuming an inelastic mean-free path of 61 nm for GaN.

curvature have been observed in AlGaN, which could be due to the uneven doping of Mg, assuming the Al composition is smoothly varied. In order to compare the obtained potential energy profile with the valence band diagram, it is necessary to clarify the difference and relationship between these two profiles. For a material with constant composition like GaN, the electrostatic potential variation is identical to the energy band variation; but for a compositionally graded material like $Al_xGa_{1-x}N$, the measured mean inner potential (MIP) difference with reference to GaN varies as $\Delta MIP(x) = 2.59\,x$, while the conduction band offset varies as $\Delta E_c(x) = 1.78\,x$ and the valence band profile varies as $\Delta E_v(x) = -0.89\,x$. Therefore, in the electrostatic potential energy the AlN layer is visible as a spike with abrupt energy steps at the interfaces. Regions with higher Al composition in the graded AlGaN exhibit higher potential energy value. From Fig. 3 (right) the MIP difference between GaN and the highest Al composition AlGaN in graded AlGaN is about 0.4 eV, indicating the highest Al composition is about 15 %, which will lead to a valence band offset of -0.135 eV. Thus, the energy barrier in the graded AlGaN sensed by the holes will be around 0.135 eV, a value matching the simulation (175 meV) quite well. To get an answer if the free carrier concentration is as well in agreement with the simulation, we investigated the electrical properties of the samples.

5. Electrical Properties

Based on the band structure simulations we have defined two kinds of samples optimized in terms of either good vertical ("best-vertical") or high lateral ("best-lateral") conductivity (see section 2). Although the simulation gave us a clear theoretical indication about the structural design parameters, the Mg memory effect in MOVPE systems is limiting the abruptness of modulation doping, and thus the performance of p-type heterostructures [13]. By an optimization of the growth conditions, we could partly overcome such problems as investigated by SIMS. A homogeneous Mg profile from the first to the last period of the superlattice could be achieved, what is important for a clear interpretation

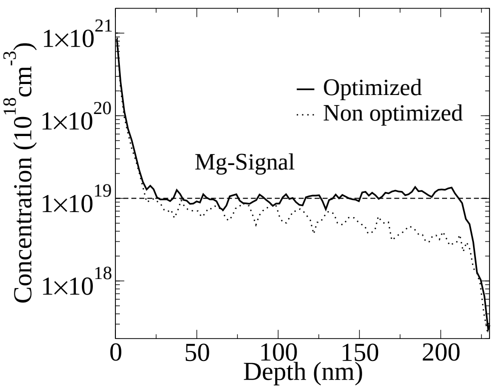

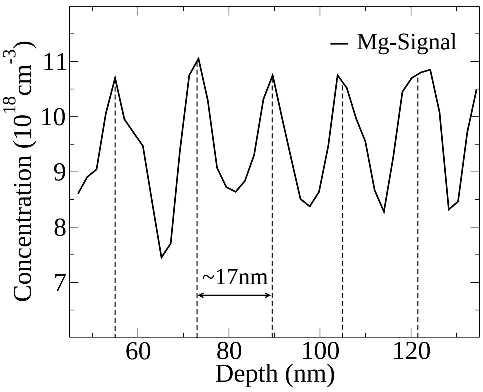

Fig. 4: On the left hand side two SIMS spectra of multi-heterostructures designed for high lateral conductivity (”best-lateral”) are shown. On the right hand side it is indicated on a linear scale that the modulation doping in the multi-heterostructures is limited by the Mg memory effect.

of the later on performed Hall measurements. On the left hand side of Fig. 4 it is clearly visible, that the averaged Mg concentration is stable at a value of about $1 \times 10^{19}\,\mathrm{cm}^{-3}$ over the whole layer of heterostructures whereas the modulation doping is limited by the Mg memory effect (Fig. 4, right). Prior to the Hall measurements the p-carriers were activated for 60 sec by an annealing step reaching a maximum temperature of about 750 °C. As contacts we used In bumps annealed at around 500 °C for 20 sec yielding ohmic behavior. The activation as well as the contact annealing were performed in air. The free hole concentrations of a ”best-lateral” structure was measured to be $5.5 \times 10^{18}\,\mathrm{cm}^{-3}$ (295 K) with a mobility of $12\,\mathrm{cm}^2/\mathrm{Vs}$, yielding a lateral conductivity of $10\,(\Omega\mathrm{cm})^{-1}$. Thus the experimentally determined values fitted quite well to the simulation results. Low temperature Hall measurements (77 K) proved the existence of a 2DHG at the AlN/GaN interface, as the conductivity could be increased to $25\,(\Omega\mathrm{cm})^{-1}$. Here the carrier concentration remained almost constant ($4.8 \times 10^{18}\,\mathrm{cm}^{-3}$) and the mobility increased to values of about $30\,\mathrm{cm}^2/\mathrm{Vs}$. The result of a temperature dependent Hall-measurement of the ”best-lateral” sample can be seen in Fig. 5. With higher temperatures the ionization of all acceptor occurs and the free hole concentration is reaching values of $1 \times 10^{19}\,\mathrm{cm}^{-3}$ as expected from SIMS measurement.

In ”best-vertical” samples we could only achieve lateral conductivities of $2.5\,(\Omega\mathrm{cm})^{-1}$ (295 K), as the ionization was remarkably lower due to the missing AlN interlayer. The carrier concentration dropped dramatically to values of about $2.4 \times 10^{18}\,\mathrm{cm}^{-3}$. Moreover the alloy disorder scattering of the holes reduced the mobility to values of about $6\,\mathrm{cm}^2/\mathrm{Vs}$.

Another proof of the perfect abruptness of the AlN/GaN-interface is given by HRXRD. The omega-2-theta scan (Fig. 6) clearly resolves the 10 fringes of the multi-heterostructure (12 periods, ”best-lateral”) at the low and high-angle side of the main GaN peak. Assuming completely strained growth the effective Al concentration was evaluated to be in the range of 7 %. As the theoretically calculated value is 5.5 % we can conclude, that the Al concentration is somewhat higher than expected and/or the linear grading of the Al flow during epitaxial growth yields a parabolic composition grading, as already observed in our n-type heterostructures [8] and indications from TEM holography (sec. 4).

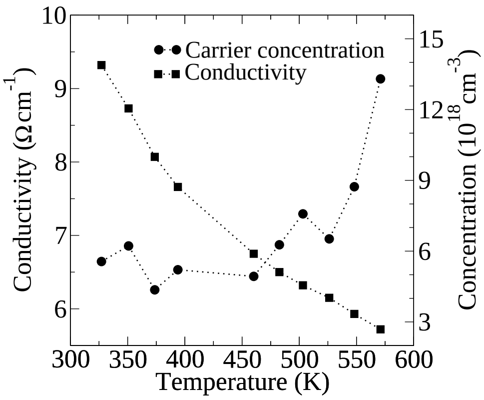

Fig. 5: Temperature dependent Hall measurement of the "best-lateral" sample.

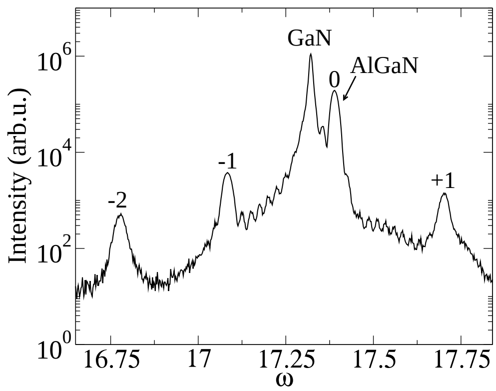

Fig. 6: X-ray diffraction (ω-2Θ) profile of an AlGaN/AlN/GaN multi-heterostructure.

In order to investigate the performance in terms of vertical conductivity, we grew three types of LEDs, one with a conventional p-GaN layer and two where the p-GaN layer was substituted by a "best-lateral" or a "best-vertical" structure, respectively. Regarding σ_V we just concentrated on the absolute voltage drop at current densities of 65 A/cm^2. The layer thickness of the p-side was either 170 nm for the LEDs with multi-heterostructures or 110nm for normal p-GaN. The lowest voltage drop was observed in the LED with "best-vertical" structure, whereas the LED with p-GaN and "best-lateral" structure showed a 4.5 % or 6 % higher power dissipation, respectively. Thus p-type AlGaN/(AlN)/GaN superlattices seem to be a candidate to increase the efficiency of high brightness LEDs.

6. Conclusion

In this study we demonstrated the experimental realization of p-type AlGaN/GaN heterostructures yielding improved vertical and lateral conductivities compared to conventional p-GaN. Such heterostructures seem to be an ideal candidate to increase the efficiency of high brightness LEDs. Prior to growth experiments band structure simulations have been performed yielding the layer profile of the heterostructure. Electron holography measurements yielded results in good agreement to the simulations.

7. Acknowledgment

This research was financially supported by Osram Opto Semiconductors and the Bundesministerium für Bildung und Forschung (BMBF). The sample characterization by K. Forghani, A. Grob, H. Kaim and S. Galichin, MicroGaN GmbH (Hall-Data) and IAF-Freiburg (SIMS) is gratefully acknowledged.

References

[1] E. F. Schubert, W. Grieshaber and I. D. Goepfert, *Appl. Phys. Lett.*, vol. 69, no. 24, pp. 3737-3739, 1996.

[2] L. Hsu and W. Walukiewicz, *Appl. Phys. Lett.*, vol. 74, no. 17, pp. 2405-2407, 1999.

[3] P. Kozodoy, Y. P. Smorchkova, M. Hansen, H. Xing, S. P. DenBaars, U. K. Mishra, A. W. Saxler, R. Perrin and W. C. Mitchel, *Appl. Phys. Lett.*, vol. 75, no. 16, pp. 2444-2446, 1999.

[4] A. Y. Polyakov, N. B. Smirnov, A. V. Govorkov, A. V. Osinsky, P. E. Norris, S. J. Pearton, J. Van Hove, A. M. Wowchack and P. P. Chow , *J. Appl. Phys.*, vol. 90, no. 8, pp. 4032-4038, 2001.

[5] B. Kuhn, F. Scholz, *phys. stat. sol. (a)*, vol. 188, no. 2, pp. 629-633, 2001.

[6] J. Hertkorn, P. Brückner, S.B. Thapa, T. Wunderer, F. Scholz, M. Feneberg, K. Thonke, R. Sauer, M. Beer, J. Zweck, *J. Crystal Growth*, vol. 308, pp. 30-36, 2007.

[7] J.-H. Kim, S.C. Choi, K.S. Kim, G.M. Yang, C.-H. Hong, K.Y. Lim, H.J. Lee, *Jpn. J. Appl. Phys.*, vol. 38, no. 5A, pp. 2721-2724, 1999.

[8] Z. H. Wu, F. A. Ponce, J. Hertkorn, F. Scholz, *Appl. Phys. Lett.*, vol. 91, no. 14, pp. 142121-1 - 142121-3, 2007.

[9] M. Grundmann, University of California, Santa Barbara, (http://my.ece.ucsb.edu/mgrundmann/bandeng.htm).

[10] S. Heikman, S. Keller, D. S. Green, S. P. DenBaars and U. K. Mishra, *J. Appl. Phys.*, vol. 94, no. 8, pp. 5321-5325, 2003.

[11] M. Z. Kauser, A. Osinsky, A. M. Dabiran, P. P. Chow, *Appl. Phys. Lett.*, vol. 85, no. 22, pp. 5275-5277, 2004.

[12] J. Hertkorn, P. Brückner, C. Gao, F. Scholz, A. Chuvilin, U. Kaiser, U. Wurstbauer, W. Wegscheider, *phys. stat. sol. (c)*, vol. 5, no. 6, pp. 1950-1952, 2008.

[13] E. L. Waldron, J. W. Graff, E. F. Schubert, *Appl. Phys. Lett.*, vol. 79, no. 17, pp. 2737-2739, 2001.

Optimization of Semipolar GaInN/GaN Blue/Green Light Emitting Diodes on $\{1\bar{1}01\}$ GaN Side Facets

Thomas Wunderer

Bluish-green semipolar GaInN/GaN light emitting diodes (LEDs) were investigated as possible candidates for high-brightness devices even in the long wavelength visible regime. To combine the high material quality known from c-GaN and the advantages of a reduced piezoelectric field, the LED structures were realized on the $\{1\bar{1}01\}$ *side facets of selectively grown GaN stripes with triangular cross section. Structural investigations using transmission electron microscopy, scanning electron microscopy, high resolution x-ray diffraction, and atomic force microscopy have been performed and could be related to the luminescence properties in photoluminescence and cathodoluminescence. The defect-related luminescence peaks at 3.3 eV and 3.42 eV typically observed in planar non- and semipolar GaN structures as fingerprints of prismatic and basal plane stacking faults, respectively, could be eliminated in our facet LED structures by optimized growth conditions.*

Furthermore, indium incorporation efficiency for these $\{1\bar{1}01\}$ *facets is found to be about 50% higher as compared to c-plane growth, what helps significantly to achieve longer wavelength emission in spite of the reduced quantum confined Stark effect in such non- and semipolar materials.*

Combining these findings, we could realize a bluish-green semipolar light emitting diode on the side facets of our GaN stripes. Continuous wave on-wafer optical output powers as high as 240 µW @ 20 mA could be achieved for about 500 nm emission wavelength in electroluminescence measurements.

1. Introduction

The optical efficiency of current commercially available (Al,Ga,In)N light emitting diodes (LEDs) is found to decrease with increasing operation wavelength [1]. This is in large part caused by the local separation of electrons and holes in the quantum wells (QWs) as a consequence of strong internal piezoelectric fields in the biaxially compressively strained GaInN QWs. Besides the reduced recombination probability and the increased recombination time, this phenomenon, also known as the Quantum Confined Stark Effect (QCSE), leads to a red-shift of the effective emission wavelength.

To circumvent the negative effects of the high piezoelectric fields on the luminescence efficiency, it is highly desirable to grow GaInN/GaN heterostructures with reduced or vanishing internal piezoelectric fields. This can be achieved by rearranging the biaxial strain to planes other than the commonly used (0001) crystal plane [2]. Several groups are currently dealing with this subject by using the *r*-plane of sapphire, for instance, on which *a*-plane GaN can be grown [3, 4]. Other approaches make use of more exotic substrates like $LiAlO_2$ [5], on which pure *m*-plane GaN growth has been achieved. However, up to now the crystal quality of layers grown on such substrates cannot compete with that obtained on the more commonly used *c*-plane sapphire or SiC wafers, which still limits the optical performance of LEDs by using those substrates [6].

More recent investigations showed that also high brightness LEDs can be obtained on non- or semipolar GaN wafers [7–9]. But those results are based on only small GaN pieces in the size of 3 x (15-25) mm^2 which were sliced from high quality *c*-plane GaN grown by HVPE [8]. Those substrates provide a very low threading dislocation and stacking fault density [9], but their costs are forbiddingly high for any commercial application [10].

With the possibility for large-scale production, these problems may be overcome by starting the epitaxial growth in the conventionally used *c*-direction, and then forming GaN stripes with less polar side facets by selective epitaxy. QWs and even complete LED structures can then be grown on these facets [11–14]. Depending on the stripe orientation and growth conditions, different crystal facets can be achieved with reduced or even vanishing polarization fields. This could be verified in different studies [12, 14–16].

In this manuscript, we report on the optimization of the GaN stripe material quality with semipolar side facets. Structural properties using high resolution x-ray diffraction (HRXRD), atomic force microscopy (AFM) and transmission electron microscopy (TEM) can be correlated to characteristics in photo- and cathodoluminescence (PL,CL). The defect-related luminescence peaks at 3.3 eV and 3.42 eV observed in those studies could be eliminated by optimized growth conditions. Furthermore, the optimization of the QW emission in the green spectral range grown by selective epitaxy is another focus. Based on these studies, complete LED structures on the side facets are presented and the results of electroluminescence (EL) measurements are described for a device emitting in the bluish-green spectral range.

2. Experimental

The samples, undoped GaN stripes and complete LED structures, were grown by low pressure metalorganic vapor phase epitaxy (MOVPE). First, about 2 μm thick high quality GaN templates were grown on *c*-plane sapphire substrates including an in-situ SiN interlayer for efficient defect reduction [17]. After the deposition of 200 nm SiO_2 mask material via plasma enhanced chemical vapor deposition (PECVD) a stripe pattern is formed using photolithography and a dry etching step with reactive ion etching (RIE). The stripes are oriented along the $\langle 11\bar{2}0 \rangle$ GaN crystal direction. The parameters of the second epitaxial step have been tailored to grow triangularly shaped GaN stripes in the several μm wide mask openings which have $\{1\bar{1}01\}$ side facets as the most stable surface. Thereafter, for the LED sample, three GaInN quantum wells were grown covered by an AlGaN electron barrier and a GaN:Mg top layer. The nominal thickness of the GaInN QWs and the GaN barriers was determined to be about 4 nm and 8 nm, respectively. Further information on the growth and processing can be found elsewhere [14].

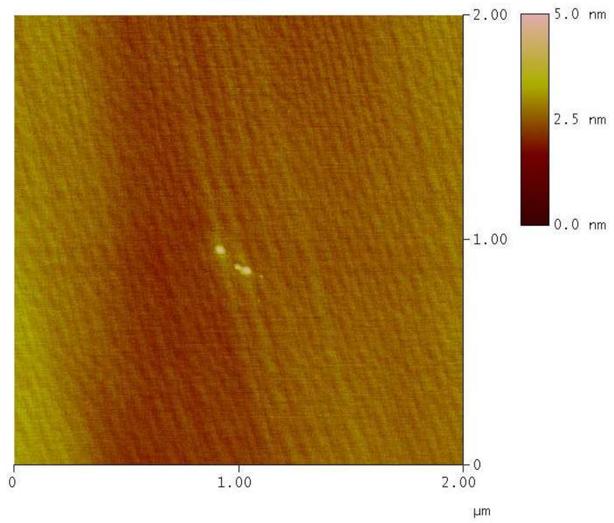

Fig. 1: 2 µm x 2 µm AFM scan of the semipolar $\{1\bar{1}01\}$ side facet of a LED structure using a special sample holder. A rms value as low as 0.25 nm was determined.

For the investigation of the structural properties, different measurement methods like HRXRD, AFM and TEM have been performed. The results could be correlated to luminescence characteristics using PL and CL. Besides, EL measurements were carried out for the LED samples emitting in the bluish-green spectral range.

3. Optimization of GaN Stripe Properties

3.1 HRXRD

First, HRXRD investigations have been performed to determine the crystal material quality of the GaN stripes. A broad beam spot of several mm^2 was used as an excitation source. Thus, the detected signal resulted from an integration over several stripes. However, the rocking curve of the $(1\bar{1}.1)$ reflection showed a relatively narrow full width at half maximum (FWHM) of 185 arcsec, whereby the stripes were oriented parallel to the plane of incidence of the x-ray beam.

3.2 AFM

Furthermore, the good material quality is comfirmed by AFM measurements. Fig. 1 shows an AFM scan of the $\{1\bar{1}01\}$ surface of a representative LED sample. For this purpose, a special holder with an inclined plane of 62° was used to orient the semipolar facet horizontally, exposing the facet to the top. The 2 µm x 2 µm scan shows a smooth surface with a rms value as low as 0.25 nm. Compared to other non- and semipolar GaN growth experiments [18–20] where only relatively rough surfaces could be achieved, this result confirms the advantage of the naturally stable surface and is one reason why the $\{1\bar{1}01\}$ plane is believed to be one of the favorable semipolar GaN planes.

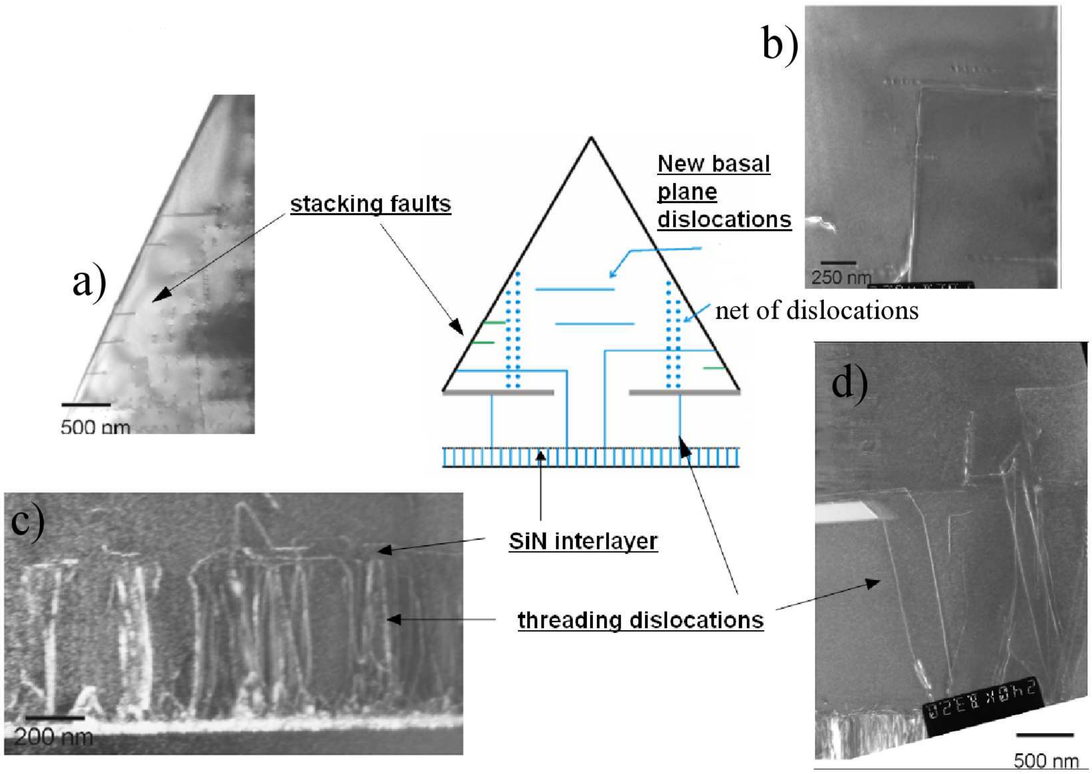

Fig. 2: TEM images from different regions of an undoped GaN stripe grown under not-optimized growth conditions. The dislocation density in the template is about $2\,x\,10^8\,cm^{-2}$.

3.3 TEM

Planar semi- and nonpolar GaN grown on different foreign substrates such as r-plane sapphire, a- and m-plane SiC, $LiAlO_2$ or $MgAl_2O_4$, etc. typically exhibit a high threading dislocation and stacking fault density [19–22]. The negative influence of these imperfections superposes the advantages of the reduction of the piezoelectric field in semi- and nonpolar materials and dominates the optical properties. That is why it is essential for high performance devices to provide good material quality with only few defects besides the reduced fields.

With respect to the defect situation in our samples, TEM investigations have been carried out for samples grown under different growth conditions. In Fig. 2 TEM images from different regions of an undoped sample are depicted. We want to point out that the GaN stripe in this specific sample was grown under unfavorable growth conditions. In Fig. 2 c) and d) one can see clearly how the threading dislocations start at the nucleation layer, propagate in growth direction and are stopped effectively through an in-situ deposited SiN interlayer. With the usage of an oxygen doped AlN nucleation layer most of the threading dislocations are edge type dislocations, whereas screw type dislocations are mostly avoided. As SiN can stop edge type dislocations effectively [23], our templates end up with a low dislocation density (all types) in the order of $2 \times 10^8\,\mathrm{cm}^{-2}$ for a $3\,\mu\mathrm{m}$ thick GaN template [17]. The few remaining dislocations which could penetrate the SiN interlayer are either stopped again by the mask material on top of the template or can proceed into the GaN stripe. It seems that not all dislocations from the template propagate into the GaN stripe, but some defects are annealed via the 2-step growth process. The remaining dislocations in the stripe running first in c-direction are then bent and continue their way in m-direction up to the semipolar surface of the facet (Fig. 2 b)).

Besides the threading dislocations originating from the template an ordered net of dislocations in the overgrown part of the triangle above the SiO_2 mask is visible (Fig. 2 a)). These dislocations are partly edge (or mixed) type and thus create a "wing tilt". The GaN stripe, grown under unfavorable growth conditions, also shows the presence of stacking faults (SF). As already mentioned, this is a serious problem for the fabrication of high quality non- and semipolar GaN-based devices. The formation of the basal plane stacking faults is mainly visible in the outer regions of the triangle in the area above the mask. This formation is believed to come along with prismatic stacking faults at the starting point of a basal plane SF, with the possibility of decoration with defects such as oxygen. The prismatic and basal plane SF show strong luminescence around 3.3 eV and 3.42 eV, respectively, which is a clear fingerprint of such defects [24]. As will be seen in the next sections concerning CL and PL measurements, we are able to suppress the defect related transitions to a negligible value and therefore the SFs under optimized growth conditions.

3.4 CL

The sample grown under not-optimized growth conditions which was used in the TEM investigations was analyzed by cathodoluminescence measurements. The SFs determined by TEM are found in the outer regions of the overgrown GaN stripes above the mask.

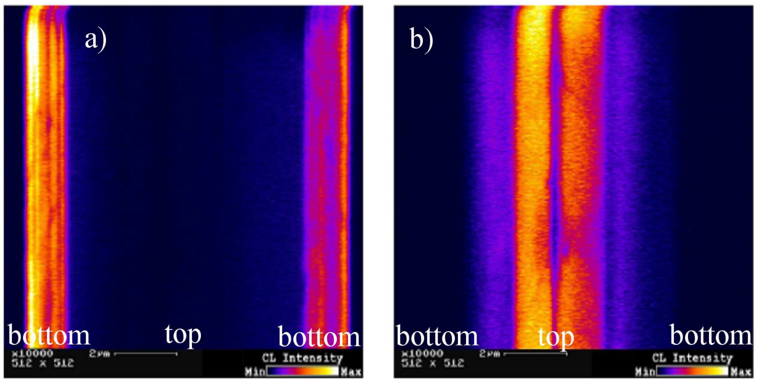

Fig. 3: Monochromatic CL image in top view of a GaN stripe grown under not-optimized growth conditions. a) Image taken from 3.29 eV - 3.33 eV (i.e. defect related). The edges of the image mark the bottom of the triangle. b) Image taken from 3.46 eV - 3.49 eV (i.e. band gap related). The vertical dark line marks the top of the triangle. The highest intensity originates from the area above the mask opening.

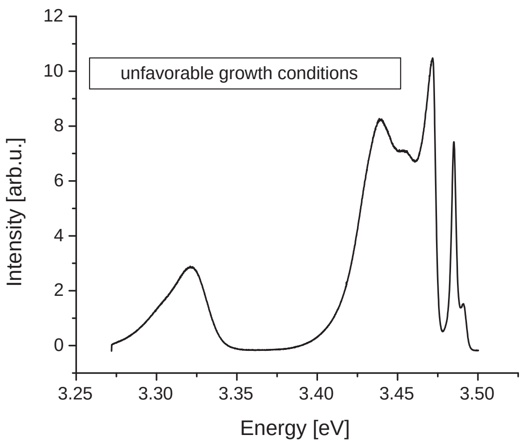

Fig. 4: PL spectrum at 13 K of several GaN stripes grown under unfavorable growth conditions. Defect-related transitions are obvious at 3.3 ev and 3.42 eV.

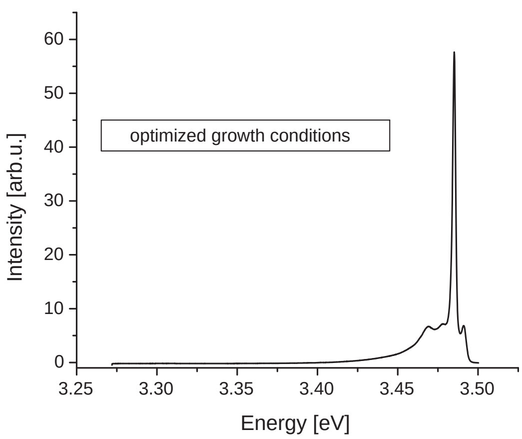

Fig. 5: PL spectrum at 13 K of several GaN stripes grown under optimized growth conditions. No defect-related transitions are obvious.

They can be correlated to strong luminescence peaks around 3.3 eV and 3.42 eV [21, 22]. CL line scans along a triangle facet as well as monochromatic CL images from a top view onto the stripe reveal that the 3.3 eV and 3.42 eV emission (not shown here) originate from the lower part of the triangles, while the band gap related emission is found on the top area (Fig. 3 a) and b)).

3.5 PL

As another tool for the investigation of the material quality photoluminescence measurements have been performed. A He-Cd laser emitting at 325 nm was used as the excitation source with a beam spot diameter of about 100 μm. Therefore several GaN stripes as well as the GaN template are excited at the same time. In Fig. 4 the PL spectrum of the sample described above is shown. This sample, grown under not-optimized growth conditions, shows again strong luminescence peaks around 3.3 eV and 3.42 eV. As already seen in the TEM and CL investigations, these transitions can be ascribed to prismatic and basal plane SF.

The V / III ratio was found to be a critical parameter for the GaN stripe growth. Fig. 5 shows the PL spectrum of a sample grown under optimized growth conditions. As can be seen, the defect-related transitions can be suppressed to a negligible value. I.e. the formation of defects that are responsible for this strong luminescence can be prevented. Thus, it is shown that high quality semipolar GaN can be grown via selective epitaxy and should open the possibility for high performance devices.

4. Optimization of Green QW Emission

The problem of current commercially available (Al,In,Ga)N LEDs is the reduced efficiency for an increasing operation wavelength. Besides the influence of the high internal fields which reduce the recombination propability, the material quality degrades for longer wavelength. It is still a challenge to grow high quality $Ga_{1-x}In_xN$ alloys with a high indium concentration. The differences in the thermodynamic properties of GaN and InN as well as the high strain which is induced due to the different lattice constants lead to the inferior material quality.

With non- and semipolar GaN one can overcome or at least reduce the influence of the high piezoelectric fields in the QWs, but for a long emission wavelength a high indium content is still needed. Due to the reduced QCSE in non- and semipolar materials an even higher In fraction is necessary to achieve the same wavelength compared to c-plane growth. The following sections concentrate on the question whether the semipolar $\{1\bar{1}01\}$ facet is a suitable choice for highly efficient light emitters in the green spectral range.

4.1 In incorporation efficiency

Due to the reduced QCSE on the semipolar facet a nominally similar QW as grown on c-plane GaN yields a blue-shifted emission. To compensate this effect, thicker QWs or a higher In fraction is required. To determine the In incorporation efficiency on our semipolar $\{1\bar{1}01\}$-plane an about 50 nm thick GaInN layer was deposited on the facet sidewalls of the triangles. In the same run a c-plane reference sample was grown. It can bee assumed that the layers are grown pseudomorphically for both samples as the thickness stays below the critical thickness. HRXRD measurements were performed for the determination of the In content. Fig. 6 shows the $\omega/2\theta$ scan of the (0002) reflection of the c-plane reference sample. For the c-plane sample an In concentration of 14.6 % was

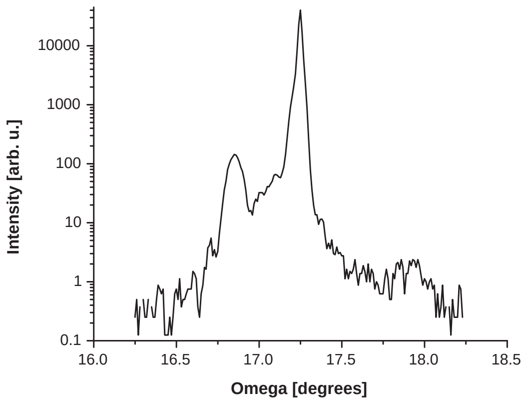

Fig. 6: $\omega/2\theta$-scan of the (0002)-reflection of the polar reference sample

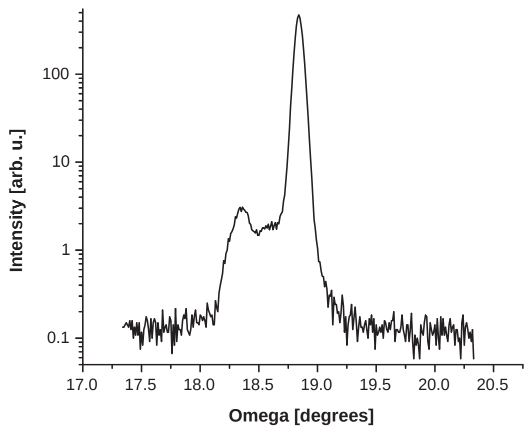

Fig. 7: $\omega/2\theta$-scan of the (1-101)-reflection of the semipolar sample

calculated. In Fig. 7 the $\omega/2\theta$-scan of the (1-101) reflex of the semipolar sample is shown. With respect to the different strain situation on inclined facets an indium concentration as high as 22 % was determined. Although the temperature could be slightly reduced on those side facets compared to *c*-plane growth and therefore increase the indium incorporation, the main reason for the higher In percentage is believed to origin from the different strain situation on the $\{1\bar{1}01\}$-plane. This is another reason why we favor this semipolar GaN plane. The noticeable higher In incorporation should help significantly to achieve longer wavelength emission in spite of the reduced QCSE.

It is worth to mention that the semipolar sample with the thick GaInN layer of about 50 nm shows strong photoluminescence peaking at 2.66 eV at room temperature (not shown). It can be assumed that there is no quantization in such a thick layer. Therefore the transition can be related to the band gap of $In_xGa_{1-x}N$. Thus, the determined In concentration via HRXRD fits well to the luminescence properties of the sample which would predict about 24 % In.

4.2 Optimization of GaInN/GaN MQW growth parameters

For the goal to push the wavelength into the green region, different growth parameters can be changed to achieve a high In incorporation. It is commonly known that low temperature, high In flow and high growth rate are the most promising parameter choices. However, the segregation of the QWs or the formation of metallic indium clusters for QWs containing a high In fraction is a serious problem also for the semipolar $\{1\bar{1}01\}$-plane. Similar to growth experiments for green emission on *c*-plane GaN [25], the best results were achieved with low temperature, high V / III ratio and similar TEGa- und TMIn-precursor flows. Fig. 8 shows the PL spectrum at room temperature for a semipolar GaInN/GaN multiple quantum well (MQW) structure emitting in the green spectral range. For the optimization of the GaInN growth parameters the template as well as the stripes are undoped. The three QWs are capped with an undoped GaN layer with

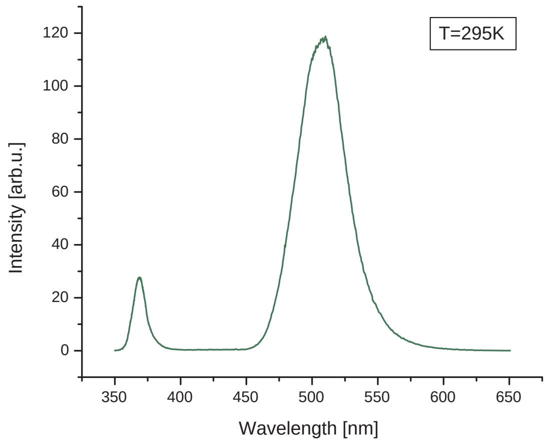

Fig. 8: PL spectrum of a semipolar undoped GaInN/GaN MQW structure showing green emission peaking at 515 nm with a FWHM of 175 meV.

a thickness of about 50 nm. Strong luminescence from the GaInN MQWs can be observed peaking at 515 nm. The relative narrow full width at half maximum (FWHM) of 175 meV @ 295K confirms the good material quality.

4.3 EL characteristics of semipolar LED

In this section EL characteristics of a semipolar LED structure emitting in the bluish-green spectral range are discussed. The growth parameters of this sample are based on an earlier stage of the GaInN/GaN MQW optimization scheme. That's why the emission wavelength is not the same as in the MQW structure described above. For the EL measurements only simple processing steps were applied. There was no mesa etching to define the LED device and for a higher light out coupling efficiency. The p-contacts were defined via standard lithography. Circular In contacts with diameters between 70 μm and 140 μm were used. The EL characteristics were measured on-wafer, collecting the light with an integrating sphere.

Fig. 9 shows the spectrum of such an LED device at a driving current of 100 mA. A FWHM of 215 meV was determined at a wavelength of 495 nm. Optical output powers as high as 240 μW @ 20 mA and 1 mW @ 110 mA have been measured on-wafer. Interestingly, the external efficiency stays nearly constant for the investigated current range (Fig. 10). This is believed to primarily result from the reduction of the piezoelectric field on the semipolar side facets.

5. Conclusion

Semipolar GaInN/GaN LEDs were realized on the $\{1\bar{1}01\}$ side facets of selectively grown GaN stripes with an on-wafer optical output power of 240 μW @ 20 mA and 1 mW @ 110 mA

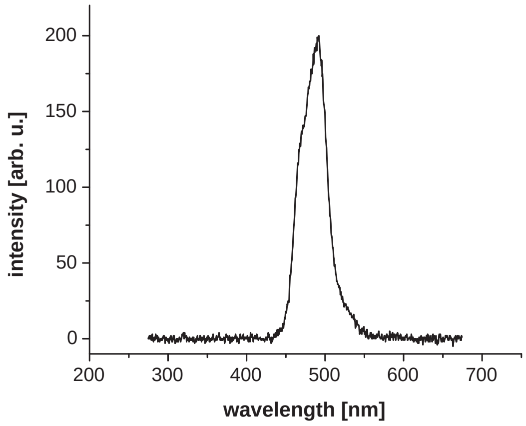

Fig. 9: EL spectrum of a semipolar facet LED at current of 100 mA.

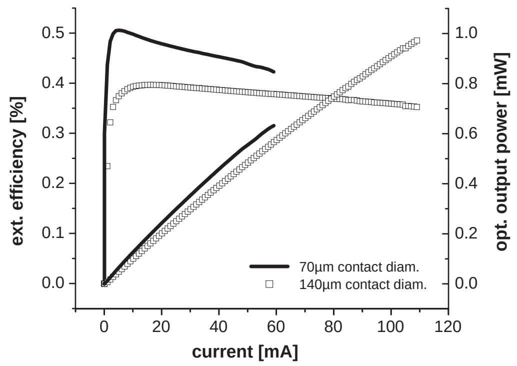

Fig. 10: Optical output power and external efficieny of semipolar facet LED measured at 495 nm emission wavelength for a p-contact diameter of 70 µm and 140 µm.

for about 500 nm. The good material quality was confirmed by a HRXRD rocking curve FWHM for the $(1\bar{1}.1)$ reflection of 185 arcsec and a AFM rms value of 0.25 nm. Defect-related luminescence peaks in CL and PL at 3.3 eV and 3.42 eV could be related to prismatic and basal plane SFs for samples grown under unfavorable growth conditions and could be suppressed completely by optimizing them. Furthermore, a 50 % higher indium incorporation for these $\{1\bar{1}01\}$ facets in comparison to *c*-plane growth is found, what helps significantly to achieve longer wavelength emission in spite of the reduced QCSE.

Acknowledgement

This work was financially supported by the Deutsche Forschungsgemeinschaft (DFG). We would gratefully acknowledge the cooperation with M. Feneberg, M. Schirra and K. Thonke from the Inst. of Semiconductor Physics and A. Chuvilin and U. Kaiser from the Central Facility of Electron Microscopy at the Ulm University and I. Knoke and E. Meissner from the Crystal Growth Laboratory at Fraunhofer IISB, Erlangen.

References

[1] J. Edmond, A. Abare, M. Bergman, J. Bharathan, K. L. Bunker, D. Emerson, K. Haberern, J. Ibbetson, M. Leung, P. Russel, and D. Slater, "High efficiency GaN-based LEDs and lasers on SiC," *J. Cryst. Growth*, vol. 272, pp. 242–250, 2004.

[2] T. Takeuchi, H. Amano, and I. Akasaki, "Theoretical study of orientation dependence of piezoelectric effects in wurtzite strained GaInN/GaN heterostructures and quantum wells," *Jpn. J. Appl. Phys.*, vol. 39, pp. 413–416, 2000.

[3] H. Ng, "Molecular-beam epitaxy of GaN/$Al_xGa_{1x}N$ multiple quantum wells on R-plane $(10\bar{1}2)$ sapphire substrates," *Appl. Phys. Lett.*, vol. 80, pp. 4369–4371, 2002.

[4] M. Craven, P. Waltereit, F. Wu, J. Speck, and S. DenBaars, "Characterization of a-plane GaN/(Al,Ga)N multiple quantum wells grown via metalorganic chemical vapor deposition," *Jpn. J. Appl. Phys.*, vol. 42, pp. L235–238, 2003.

[5] P. Waltereit, O. Brandt, A. Trampert, H. Grahn, J. Menniger, M. Ramsteiner, M. Reiche, and K. Ploog, "Nitride semiconductors free of electrostatic fields for efficient white light-emitting diodes," *Nature*, vol. 406, pp. 865–868, 2000.

[6] A. Chakraborty, B. Haskell, H. Masui, S. Keller, J. Speck, S. DenBaars, S. Nakamura, and U. Mishra, "Nonpolar m-plane blue-light-emitting diode lamps with output power of 23.5 mW under pulsed operation," *Jpn. J. Appl. Phys.*, vol. 45, pp. 739–741, 2006.

[7] M. Schmidt, K.-C. Kim, H. Sato, N. Fellows, H. Masui, S. Nakamura, S. DenBaars, and J. Speck, "High power and high external efficiency m-plane InGaN light emitting diodes," *Jpn. J. Appl. Phys.*, vol. 46, pp. L126–128, 2007.

[8] K.-C. Kim, M. Schmidt, H. Sato, F. Wu, N. Fellows, M. Saito, K. Fujito, J. Speck, S. Nakamura, and S. DenBaars, "Improved electroluminescence on nonpolar m-plane InGaN/GaN quantum wells LEDs," *phys. stat. sol. (RRL)*, vol. 1, pp. 125–127, 2007.

[9] A. Tyagi, H. Zhong, N. Fellows, M. Iza, J. Speck, S. DenBaars, and S. Nakamura, "High brightness violet InGaN/GaN light emitting diodes on semipolar $(10\bar{1}\bar{1})$ bulk GaN substrates," *Jpn. J. Appl. Phys.*, vol. 46, pp. L129–131, 2007.

[10] U. Schwarz and M. Kneissel, "Nitride emitters go nonpolar," *phys. stat. sol. (RRL)*, vol. 1, pp. A44–46, 2007.

[11] T. Takeuchi, S. Lester, D. Basile, G. Girolami, R. Twist, F. Mertz, M. Wong, R. Schneider, H. Amano, and I. Akasaki, "Polarization control in nitride-based semiconductor," in *IPAP Conf. Series*, *Proc. Int. Workshop on Nitride Semiconductors*, vol. 1, p. 137, 2000.

[12] K. Nishizuka, M. Funato, Y. Kawakami, S. Fujita, Y. Narukawa, and T. Mukai, "Efficient radiative recombination from $< 11\bar{2}2 >$-oriented $In_xGa_{1-x}N$ multiple quantum wells fabricated by the regrowth technique," *Appl. Phys. Lett.*, vol. 85, pp. 3122–3124, 2004.

[13] S. Khatsevich, D. H. Rich, X. Zhang, W. Zhou, and P. D. Dapkus, "Temperature dependence of excitonic recombination in lateral epitaxially overgrown InGaN/GaN quantum wells studied with cathodoluminescence," *J. Appl. Phys.*, vol. 95, pp. 1832–1842, 2004.

[14] T. Wunderer, P. Brückner, B. Neubert, F. Scholz, M. Feneberg, F. Lipski, M. Schirra, and K. Thonke, "Bright semipolar GaInN/GaN blue light emitting diode on side

facets of selectively grown GaN stripes," *Appl. Phys. Lett.*, vol. 89, pp. 041121–1–3, 2006.

[15] M. Feneberg, F. Lipski, R. Sauer, K. Thonke, T. Wunderer, B. Neubert, P. Brückner, and F. Scholz, "Piezoelectric fields in GaInN/GaN quantum wells on different crystal facets," *Appl. Phys. Lett.*, vol. 89, pp. 242112–1–3, 2006.

[16] T. Wunderer, P. Brückner, J. Hertkorn, F. Scholz, G. Beirne, M. Jetter, P. Michler, M. Feneberg, and K. Thonke, "Time- and locally resolved photoluminescence of semipolar GaInN/GaN facet light emitting diodes," *Appl. Phys. Lett.*, vol. 90, pp. 171123–1–3, 2007.

[17] J. Hertkorn, P. Brückner, S. Thapa, T. Wunderer, F. Scholz, M. Feneberg, K. Thonke, R. Sauer, M. Beer, and J. Zweck, "Optimization of nucleation and buffer layer growth for improved GaN quality," *J. Cryst. Growth*, vol. 308, pp. 30–36, 2007.

[18] M. D. Craven, S. H. Lim, F. Wu, J. S. Speck, and S. P. DenBaars, "Structural characterization of nonpolar (11-20) a-plane GaN thin films grown on (1-102) r-plane sapphire," *Appl. Phys. Lett.*, vol. 81, pp. 469–471, 2002.

[19] A. Chakraborty, K. C. Kim, F. Wu, J. S. Speck, S. P. DenBaars, and U. K. Mishra, "Defect reduction in nonpolar a-plane GaN films using in situ SiN_x nanomask," *Appl. Phys. Lett.*, vol. 89, pp. 041903–1–3, 2006.

[20] T. J. Baker, B. A. Haskell, F. Wu, J. S. Speck, and S. Nakamura, "Characterization of Planar Semipolar Gallium Nitride Films on Sapphire Substrates," *Jpn. J. Appl. Phys.*, vol. 45, pp. L154–L157, 2006.

[21] P. P. Paskov, R. Schifano, B. Monemar, T. Paskova, S. Figge, and D. Hommel, "Emission properties of a-plane GaN grown by metal-organic chemical-vapor deposition," *J. Appl. Phys.*, vol. 98, pp. 093519–1–3, 2007.

[22] T. Gühne, Z. Bougrioua, P. Vennéguès, M. Leroux, and M. Albrecht, "Cathodoluminescence spectroscopy of epitaxial-lateral-overgrown nonpolar (11-20) and semipolar (11-22) GaN in relation to microstructural characterization," *J. Appl. Phys.*, vol. 101, pp. 113101–1–6, 2007.

[23] K. Engl, M. Beer, N. Gmeinwieser, U. T. Schwarz, J. Zweck, W. Wegscheider, S. Miller, A. Miler, H.-J. Lugauer, G. Brüderl, A. Lell, and V. Härle, "Influence of an in situ-deposited SiN_x intermediate layer inside GaN and AlGaN layers on SiC substrates," *J. Cryst. Growth*, vol. 289, pp. 6–13, 2006.

[24] J. Mei, S. Srinivasan, R. Liu, F. A. Ponce, Y. Narukawa, and T. Mukai, "Prismatic stacking faults in epitaxially laterally overgrown GaN," *Appl. Phys. Lett.*, vol. 88, pp. 141912–1–3, 2006.

[25] D. Fuhrmann, U. Rossow, C. Netzel, H. Bremers, G. Ade, P. Hinze, and A. Hangleiter, "Optimizing the internal quantum efficiency of GaInN SQW structures for green light emitters," *phys. stat. sol. (c)*, vol. 3, pp. 1966–1969, 2006.

Heteroepitaxial Growth of GaN on ZnO by MOVPE

Sarad Bahadur Thapa

In order to establish the growth of GaN on ZnO, we studied different procedures to overcome the detrimental influence of normal GaN growth conditions on the naked ZnO surface. With a two-layer process, only poor GaN quality could be obtained. This could be remarkably improved by optimizing the growth procedure and implementing additional annealing steps. However, the finally obtained material quality is still limited due to the maximum applicable growth temperature about 150°C below the best conditions for GaN on other substrates.

1. Introduction

In recent years, the growth of GaN–ZnO heterostructures has attracted much attention due to the similar material properties of GaN (III–V type) and ZnO (II–VI type), especially a very small lattice mismatch of approximately 1.9 % of the a lattice constant and almost similar thermal expansion coefficients. This may be in particular helpful to realize a pn-junction in planar or coaxial form [1] for nano-photonics and nano-electronics applications because of the much better p-doping properties of GaN as compared to ZnO. The heterostructure of GaN on ZnO could be also used as a template for the Hydride Vapor Phase Epitaxy (HVPE) growth of a free standing GaN bulk layer by utilizing the ZnO layer as a separation layer [2]. There are several reports on heteroepitaxial growth of ZnO on GaN [3], but few are found for GaN on ZnO growth. Although some groups have successfully grown GaN on ZnO by molecular beam epitaxy (MBE) [4] or pulsed laser deposition (PLD) [5, 6] techniques, only a few groups have reported the growth of GaN on ZnO by metalorganic vapour phase epitaxy (MOVPE), and the material quality is still not on par with the device level [7, 8]. There are, basically, two major problems in the MOVPE growth of GaN on ZnO, namely, the instability of ZnO itself at high temperatures and the decomposition of ZnO after exposure to NH_3 and H_2 at temperatures in excess of 650°C. In this study, we present some approaches to cope with the above mentioned problems for growing GaN epitaxial layers on ZnO in a low pressure (LP) MOVPE system. We report here the physical and optical properties of the GaN layers grown under different growth conditions. Finally, we have determined a quite effective growth process to deal with the inherent detrimental properties of ZnO when subjected to a MOVPE system.

2. Experimental

Undoped layers of GaN were grown on c-plane ZnO layers in an AIXTRON AIX 200 RF LP-MOVPE system by using trimethylgallium (TMGa) and NH_3 as precursors. Both,

H_2 and N_2 gases were used as carrier gas and the ambient gas was H_2+N_2 and N_2, respectively. All growth temperatures indicated in this report are thermocouple read-outs in the susceptor main body. The ZnO layers used in this study were grown by pulsed laser deposition (PLD), and chemical vapor deposition (CVD) techniques. In PLD technique, undoped ZnO thin films were grown on 2-inch diameter a-plane sapphire substrates using a KrF excimer laser with 248 nm wavelength. The source target was pressed and sintered at 1150°C from commercial 5N5 ZnO powder (Alfa Aesar). A laterally homogeneous film thickness of about 600 nm on the 2-inch substrate was achieved by an offset distance between substrate center and direction of plasma plume propagation, as demonstrated in [9]. The growth temperature was about 650°C and the oxygen partial pressure during growth was 0.01 mbar. In CVD technique, a buffer layer of Zn about 150 nm thick, using zinc acetate (Zn[Ac]2) as a source, was grown on a MOVPE grown GaN template at a temperature between 300°C and 400°C followed by annealing for 1 hour at 800°C to 900°C. Then a 1 to 3 µm thick bulk ZnO layer was grown, using zinc powder (Alpha Aesar, 5N5) as a source, in an O/Ar gas atmosphere at a temperature between 700°C and 820°C. Scanning electron microscopy (SEM), and high resolution x-ray diffraction (HRXRD) measurements (with 0.6/0.2 mm slits) were carried out to observe the physical properties of GaN and ZnO layers. The optical properties were investigated by low temperature (20 K) photoluminescence (PL) measurements.

3. Results and Discussions

In preliminary studies, we observed the malignant effect of H_2 and NH_3 with a rise in temperature on the ZnO layer. We carried out several experiments of the growth of a single layer of GaN of about 500 nm thickness on a ZnO layer at different temperatures by using H_2 as a carrier gas. The detrimental effect of H_2 and NH_3 was observed at the growth temperature of 675°C and above. In optical microscopy, a number of cracks and many bubble like structures were distinctly visible. The SEM analysis showed a very random 3D growth of GaN. On the cross sectional view, a void between the GaN and ZnO layers was clearly visible at many parts of the sample. At a temperature above 600°C, the dissociation of NH_3 takes place rapidly and contributes more H_2. The etching of ZnO by these H_2 molecules at the onset of the growth process becomes very aggressive at temperatures above 675°C. However, the cross sectional observation of SEM shows that the interfaces between the GaN and ZnO layers were quite smooth in the samples grown at 600°C and below. Unfortunately, there were no indications of GaN related peaks in HRXRD and low temperature PL measurements in all samples grown below 700°C.

In the following experiments we implemented a two-layer growth process by using either H_2 or N_2 as a carrier gas. An initial buffer layer of GaN with varying thickness was deposited at 550°C. The buffer layer should be thick enough to closely cover the ZnO layer to protect it from etching by H_2 during the high temperature of the final layer growth. The thickness also depends upon the surface quality of the ZnO layer. Then the buffer layer was annealed in NH_3 or N_2 ambient up to the maximum corresponding temperature of 950°C or 1050°C. Since the edges of the samples are normally not fully covered by the buffer layer, NH_3 etches the ZnO very rapidly through these edges at higher annealing temperature. A final GaN layer of about 1µm thickness was grown at 1000°C and 950°C in case of N_2 and H_2 as a carrier gas, respectively. The precursor flow rates of both layers were kept constant. In SEM analysis, we observed a GaN surface containing densely arranged hexagonal crystallites with different sizes oriented in random directions (Fig. 1).

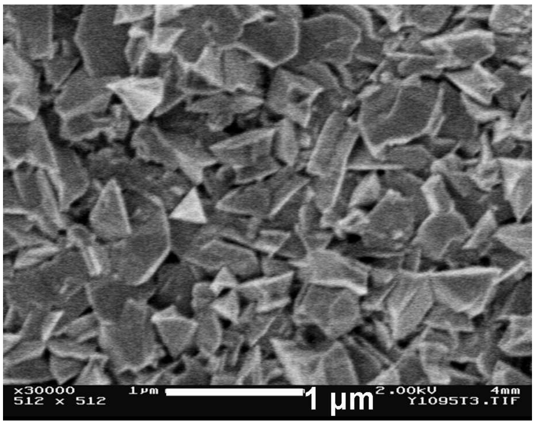

Fig. 1: SEM image illustrating a large number of crystallites of GaN having random size grown by using a two layer growth process.

This was even more pronounced in case of N_2 as carrier gas. The comparatively larger size of the crystallites in the samples grown with H_2 as a carrier gas indicates the stronger occurrences of coalescence of small 3D islands during the final layer growth of GaN. It shows that H_2 helps to enhance the lateral growth of GaN. Low temperature PL measurements show a broad GaN peak having very low intensity. There is always a high probability of etching ZnO at any instance either from the edges of the sample or down through the trenches of 3D islands of GaN by diffusion during the growth or annealing period in NH_3 ambient. This may cause the incorporation of Zn or O elements into GaN during the growth process. The resulting very high defect density along with the observed structural defects which certainly act as non-radiative centers and the possibility of further absorption in the ZnO layer explain the observed weak and broad GaN PL spectra [7]. We could not detect a distinct GaN peak in HRXRD measurement in this growth process. From these observations, it is clear that a perfect coverage of the ZnO layer by a low temperature GaN buffer layer is the most important issue. However, we also observed that a very thick buffer layer consequently deteriorates both the surface and the crystal quality. Hence, we implemented a multilayer growth process to overcome the limitations of the buffer layer thickness. In this process, we deposited a GaN buffer layer of about 150 nm thickness at 550°C. Since the quality of the subsequently grown layers was not much dependent on the usage of N_2 or H_2 as a carrier gas in the underlying first buffer layer growth, we used N_2 as a carrier gas here to minimize the risk of etching ZnO at the onset of the growth process. For the growth of the subsequent layers, we used H_2 as a carrier gas. The buffer layer was heated under NH_3 up to 700°C and then annealed in N_2 ambient up to 1050°C to re-crystallize it. An intermediate GaN layer of about 50 to 100 nm was grown at 800°C with the same precursor flows as used for the first buffer layer. The insertion of such an intermediate layer could also minimize the further diffusion of Zn and O elements into the subsequently grown layers. Moreover, this layer produced a substantial change on the surface quality of the final GaN layer. The intermediate

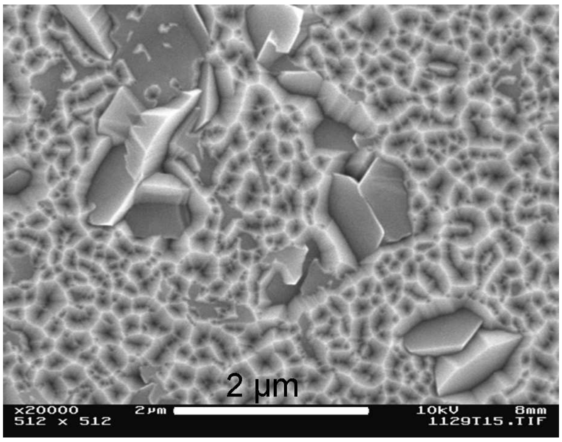

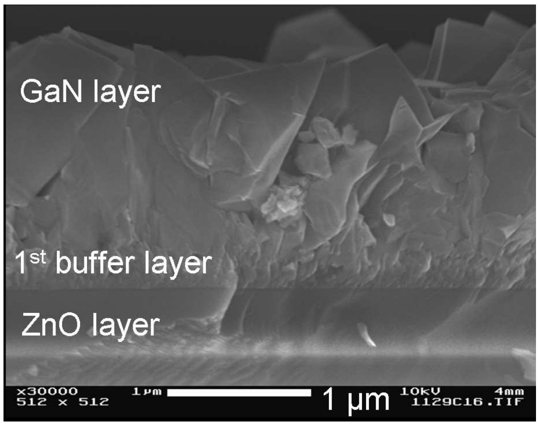

Fig. 2: SEM images of GaN grown by using a multi layer growth process. Top view (left) showing a reduced number of crystallites. A large number of hexagonal pits are visible in between the large crystallites. Cross sectional view (right) illustrating GaN and ZnO layers.

layer was heated in NH_3 ambient up to 950°C and then annealed in N_2 ambient up to 1050°C. Then, a final layer of GaN at a temperature of 950°C was grown with a reduced flow of NH_3 because of the higher cracking efficiency of NH_3 at high temperature. After about 150 nm, we stopped the growth and annealed up to 1000°C in NH_3 ambient for a short period of 30 seconds and again started growing at 950°C. Such an annealing step enhances the coalescence of the GaN islands and we observed significant improvement of the surface flatness (Fig. 2).

Although the growth mode was not 2D, we observed a well ordered crystalline structure in many areas of the sample. Thus, the decrease in the density of crystallites and emergence of fairly flat areas demonstrate the effectiveness of our growth process. Figure 3 shows the ω-2θ scan of the (002) reflection of HRXRD measurement.

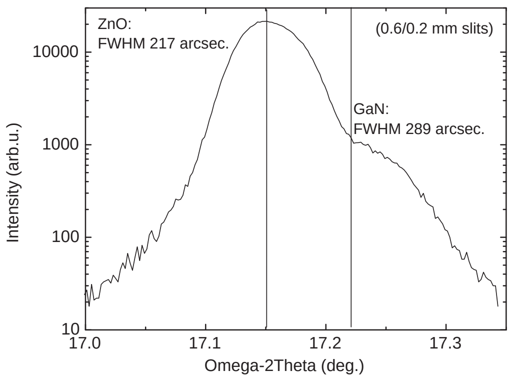

Fig. 3: ω-2θ scan for (002) reflection of HRXRD measurement. A separation of $\approx 0.07°$ between the peaks of ZnO and GaN fits the lattice mismatch.

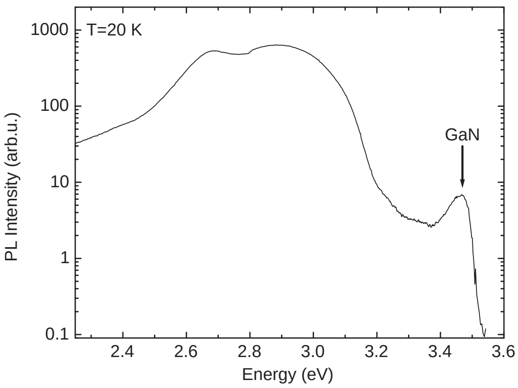

Fig. 4: Low temperature PL spectra illustrating the GaN related peak .

The reflection from the GaN layer is distinctively visible at the right shoulder of the

ZnO peak. Due to the broadening of the ZnO peak, we do not see two separate peaks of ZnO and GaN. However, the FWHM of GaN is estimated to be about 290 arcsec. The separation between the two peaks of GaN and ZnO is approximately 0.07° which fits with the approximate lattice mismatch. In PL measurements (Fig. 4), we observe a clear signal from GaN, although with low intensity and fairly broad linewidth. The broad luminescence at the lower energy region peaking at about 2.9 eV is attributed to an excessive incorporation of impurities in the GaN layer due to the diffusion of Zn and O. Moreover, we also grew the final GaN layer at 1000°C by using N_2 as a carrier gas and annealed up to 1050°C in N_2 ambient. Although the low temperature PL spectra were similar to Fig. 4, the surface quality in SEM observation and the HRXRD spectra were relatively inferior.

4. Conclusion

The major issue of successful MOVPE growth of GaN on ZnO is how to protect the underlying ZnO layer from the etching effect of H_2. The presence of H_2 during the growth period is an unavoidable fact in MOVPE technology. However, by implementing our multilayer growth process, we are successfull to some extent to address this issue. We demonstrated the successful growth of GaN by using H_2 as a carrier gas at 950°C. In our MOVPE system, a high quality GaN layer is normally grown at a temperature above 1100°C. At such high temperatures, even a pinhole in the covering layer could be sufficient to dissociate the underlying ZnO due to the strong reactivity of H_2 with ZnO. Thus, a complete covering of ZnO is an indispensable requirement before growing the GaN at such a high temperature. Hence, it is still a great challenge to successfully grow device level quality of GaN on ZnO in MOVPE.

5. Acknowledgement

I am grateful to C. Kirchner, former postdoc of the Institute, for the MOVPE growth of ZnO samples, A. Reiser, K. Thonke, and R. Sauer of the Institute of Semiconductor Physics of University of Ulm for CVD growth of ZnO samples, H. Hochmuth, M. Lorenz, and M. Grundmann of Semiconductor Physics Group, Institute for Experimental Physics II of University of Leipzig for PLD growth of ZnO samples used for our studies, H. Schils, H. Paul, and C.E. Krill of the Institute of Micro and Nanomaterials of University of Ulm for X-ray texture measurement. I acknowledge E. Angelopoulos for his masters thesis on this topic and L. Xianming for SEM measurements. I would like to thank J. Hertkorn, P. Brückner, T. Wunderer, F. Lipski, R. Blood for the discussions on epitaxy and system maintenances. Fruitful discussions with A. Ougazzaden and coworkers (Georgiatech Lorraine, Metz, France) are gratefully acknowledged. This work was partly financially supported by the Landesstiftung Baden-Württemberg within the competence network "Functional Nanostructures" and by Freiberger Compound Materials GmbH, Freiberg.

References

[1] S. Jin An, W. II Park, G.-C. Yi, Y.-J. Kim, H.-B. Kang, and M. Kim, "Heteroepitaxal fabrication and structural characterizations of ultrafine GaN/ZnO coaxial nanorod heterostructures", *Appl. Phys. Lett.*, vol. 84, no. 18, pp. 3612–3614, 2004.

[2] S.W. Lee, T. Minegishi, W.H. Lee, H. Goto, H.J. Lee, S.H. Lee, H.-J. Lee, J.S. Ha, T. Goto, T. Hanada, M.W. Cho and T. Yao, "Strain-free GaN thick films grown on single crystalline ZnO buffer layer with in situ lift-off technique", *Appl. Phys. Lett.*, vol. 90, pp. 061907–061909, 2007.

[3] C. Kirchner, T. Gruber, F. Reuss, K. Thonke, A. Waag, C. Giessen and M. Heuken, "MOVPE growth of ZnO using various oxygen precursors", *J. Cryst. Growth*, vol. 248, pp. 20–24, 2003.

[4] T. Ohgaki, S. Sugimura, N. Ohashi, I. Sakaguchi, T. Sekiguchi, and H. Haneda, "Structure and properties of GaN films grown on single crystalline ZnO substrates by molecular beam epitaxy", *J. Cryst. Growth*, vol. 275, pp. e1143–e1148, 2005.

[5] A. Kobayashi, S. Kawano, Y. Kawaguchi, J. Ohta, and H. Fujioka, "Room temperature epitaxial growth of m-plane GaN on lattice-matched ZnO substrates", *Appl. Phys. Lett.*, vol. 90, pp. 041908-1–3, 2007.

[6] C. Yang, B. Man, H. Zhuang, X. Wei, M. Liu, and C. Xue, "Annealing of GaN/ZnO/Si Films Deposited by Pulsed Laser Deposition", *Jpn. J. Appl. Phys.*, vol. 46, no. 2, pp. 526–529, 2007.

[7] N. Li, E.-H. Park, Y. Huang, S. Wang, A. Valencia, B. Nemeth, J. Nause, and I. Ferguson, "Growth of GaN on ZnO for Solid State Lighting Applications", Proc. SPIE 6337, pp. 63370Z-1–6, 2006.

[8] R. Paszkiewicz, B. Paszkiewicz, R. Korbutowicz, J. Kozlowski, M. Tlaczala, L. Bryja, R. Kudrawiec, and J. Misiewicz, "MOVPE GaN Grown on Alternative Substrates", *Cryst. Res. Technol.*, vol. 36, pp. 971–977, 2001.

[9] M. Lorenz, H. Hochmuth, D. Natusch, H. Bürner, K. Kreher, and W. Schmitz, "Large-area double-side pulsed laser deposition of $YBa_2Cu_3O_{7-x}$ thin films on 3-in. sapphire wafers", *Appl. Phys. Lett.*, vol. 68, no. 23, pp. 3332–3334, 1996.

Studies of Si Doped AlN Layers for n-type Electrical Conductivity

Sarad Bahadur Thapa

We have grown high quality AlN layers on c-plane sapphire substrates in our LP MOVPE system. We doped the AlN layers with Si to obtain n-type electrical conductivity. We observe that the Si incorporation leads to the degradation of surface and crystal quality as well as in-plane tensile stress of the AlN layer. Finally, we have obtained a fair electrical conductivity for a Si doped AlN layer which has a Si concentration of $1.5 \cdot 10^{18}$ cm^{-3}. By room temperature Van der Pauw Hall measurements, we have found: electron carrier concentration of $4 \cdot 10^{14}$ cm^{-3}, carrier mobility of 30 cm^2 V^{-1} s^{-1}, and resistivity of 530 Ω cm. By varying the temperature, an activation energy of about 200 meV could be estimated. Meantime, we observe that the electrical conductivity is correlated with the intensity ratio between the deep level transition at 3 eV and the near-band-edge luminescence of low temperature CL spectrum.

1. Introduction

Recently, aluminum nitride (AlN) has attracted much attention due to its extremely large direct bandgap (approx. 6.0 eV) and outstanding thermal and chemical stability. AlN and $Al_xGa_{1-x}N$ ternary alloys have a wide application perspective especially in the area of high-power high-temperature electronic and UV region optoelectronic devices [1–3]. For such device applications, intentional doping is essential to achieve sufficient electrical conductivity and control carrier concentrations. However, very limited reports have been so far published on the transport phenomena and properties of intentionally doped pure AlN and high Al content $Al_xGa_{1-x}N$ ternary alloys compared to GaN or InGaN, due primarily to the difficulties on the epitaxial growth of high quality layers of these materials [4–7]. Especially the effective and efficient doping of such materials to obtain the required electrical conductivity for practical AlN based devices remains a key issue for the nitride researchers. The major issues associated with poor electrical conductivity of AlN are the high ionization energy of dopants, solubility, and compensation by native defects and unintentionally incorporated background impurities. In this report, we present the results of a high quality undoped AlN bulk layer and the effect of Si doping on structural and spectroscopic properties. We also report the effect of [Si] on the intensity of deep level transitions in low temperature (10 K) cathodoluminescence (CL) spectra, which are presumably due to Al vacancies and/or of related complexes [7], and the electrical conductivity of the corresponding sample.

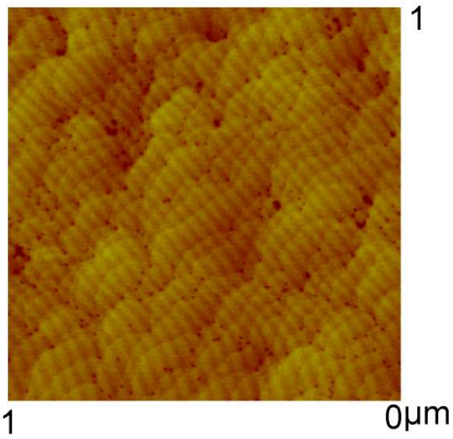

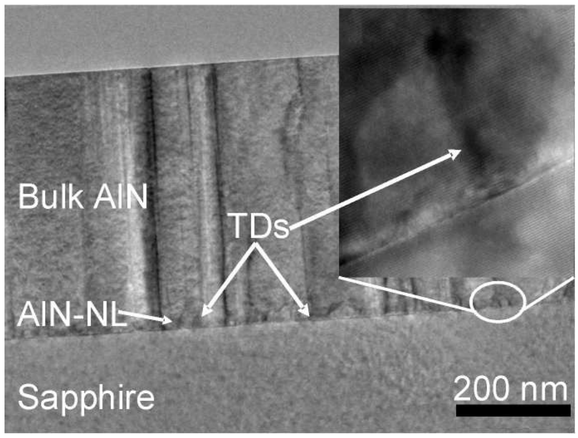

Fig. 1: AFM image of the optimized AlN layer grown at 1190 °C (left). Cross sectional bright field TEM image illustrating threading dislocations (TDs) (right).

2. Experimental

We deposited approx. 500 nm to 1 μm thick AlN layers on *c*-plane sapphire substrates in an AIXTRON AIX 200 RF LP–MOVPE system at a growth temperature of 1190°C and a pressure of 35 mbar in N_2 and H_2 ambient. Trimethylaluminum (TMAl) and NH_3 were used as group III and V precursors, respectively and H_2 was used as a carrier gas. The details of the growth process are described elsewhere [8, 9].

Si doping, by using silane (SiH_4), was performed by typically depositing a 350 nm thick Si-doped AlN layer on a 250 nm thick optimized undoped AlN buffer layer. The basic growth conditions of the Si-doped layers were similar to those of the undoped buffer layers.

The surface quality was analyzed by using atomic force microscopy (AFM). High-resolution X-ray diffraction (HRXRD) rocking curve measurements (ω scan with open detector) were carried out to examine the crystal quality of AlN epitaxial layers. Low temperature (T=10 K) CL provided information about the spectroscopic properties. Varying temperature two and four point I–V, and room temperature Van der Pauw Hall measurements were carried out to measure electrical properties. The Si concentration [Si] was extrapolated from our growth parameters using other AlN samples as reference which had been measured by secondary ion mass spectroscopy (SIMS) [10].

3. Results and Discussion

We obtained an atomically flat surface of the undoped AlN layer with a measured rms surface roughness of 0.2 nm as shown in Fig. 1 (left). A large number of networks of small pits is also visible on the surface which can be related with the threading dislocations as seen on the cross sectional TEM image (Fig. 1 (right)). The density of such small pits is approximately $1 \cdot 10^{10}\,\mathrm{cm}^{-2}$. These small pits may reflect the contribution of all types of threading dislocations present in the layer as confirmed by plan-view TEM. However, the density of large hexagonal pits (diameter more than 50 nm) on the surface was significantly reduced to less than $10^4\,\mathrm{cm}^{-2}$. The FWHM of the X-ray rocking curve for symmetric (002)

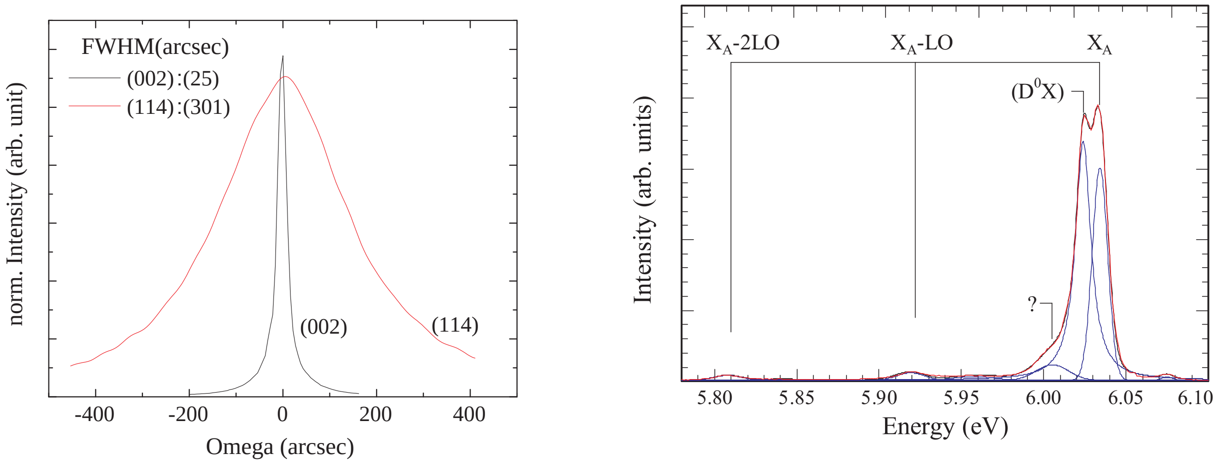

Fig. 2: HRXRD rocking curve measurements of an 1 µm thick undoped AlN layer illustrating FWHM of symmetric (002) and asymmetric (114) reflections (left). Low temperature (10 K) CL spectra of the undoped AlN layer (right) illustrating the FWHM of the near band-edge CL peaks to be 10 meV.

and asymmetric (114) reflections are 37 and 338 arcsec, respectively. Similar as described by others [11], we observed a further improvement of our undoped AlN layer by growing a thicker layer of about 1 µm. The FWHM of the X-ray rocking curve for (002) and (114) reflections of this sample is 25 arcsec and 300 arcsec, respectively (Fig. 2 (left)). The high quality of our AlN layer was further confirmed by the observation of a very narrow near band-edge excitonic emission. The two main contributions exhibit only a FWHM of about 10 meV determined from a lineshape analysis of the emission peak shown in Fig. 2 (right). The two lines at 6.024 and 6.034 eV are assigned to a donor bound (D_0X) and the A free exciton (X_A) transition, respectively. This assignment was proven by analysing temperature dependent CL measurements as shown for similar samples in [12]. The position of the A free exciton transition (X_A) indicates that our AlN layer is almost unstrained.

We studied the effect of Si doping on the structural and spectroscopic properties of the AlN layer. Similar to our previous report [9], we again found an adverse effect of Si doping on the surface and crystal quality of our lastly optimized AlN layers. The degradation of the surface and crystal quality may be related to the evolution of new defect networks in the Si doped area. TEM investigations show the emergence of pure screw and/or mixed type threading dislocations with Si introduction. However, the edge type threading dislocations, which run throughout the layer thickness, are indifferent to the Si incorporation. Figure 3 (left) shows a narrow near band-edge excitonic emission having a FWHM of about 20 meV of a Si doped sample having [Si] of $1.5 \cdot 10^{18}$ cm^{-3} by low temperature (10 K) CL measurement. The luminescence peak is resolved into two transitions at 5.962 eV and 5.986 eV for a donor bound exciton, (D_0X), due to Si donors and the A free exciton (X_A), respectively. The position of the A free exciton transition (X_A) indicates that our AlN layer is strained. Furthermore, as reported in [9], the HRXRD evaluations and the red shift of the near band-edge CL peaks of samples having different [Si] show an in-plane tensile strain up to [Si] of $2 \cdot 10^{19}\,\mathrm{cm^{-3}}$. The appearance of tensile strain in these samples was also observed in Raman studies of the E_2- mode, which showed a shift towards lower wavenumbers (see e.g. [13]). Hence, it is confirmed that Si doping up to the concentration of approx. $2 \cdot 10^{19}\,\mathrm{cm^{-3}}$ leads to tensile strain within the AlN layer. Additionally, in CL measurements, we observe deep level transitions at about 3 eV and 3.5 eV which presumably are due to Al vacancies and of respective complexes [7, 14]. The intensity ratio between the deep level transition at 3 eV and the near band-edge luminescence is changing with [Si] as shown in Fig. 3 (right). We observe a minimum intensity ratio for the sample having a Si concentration of $1.5 \cdot 10^{18}\,\mathrm{cm^{-3}}$. By room temperature Van der Pauw Hall measurements, we have found fair electrical conductivity for this sample: electron carrier concentration of $4 \cdot 10^{14}\,\mathrm{cm^{-3}}$, carrier mobility of $30\,\mathrm{cm^2V^{-1}s^{-1}}$, and resistivity of $530\,\Omega\,\mathrm{cm}$. By varying the temperature, an activation energy of about 200 meV could be estimated. Therefore, we observed that best electrical conductivity is correlated with a minimum intensity ratio between the deep level transition at 3 eV and the near band-edge luminescence. Higher Si doped samples having a larger intensity ratio are highly resistive. This is basically due to the acceptor-like type of the Al vacancies which are compensating the Si donors. Hence, it is imperative to reduce Al vacancies and the respective complexes to obtain desirable electrical conductivity in AlN. Reducing, especially, the edge type threading dislocations could help to improve the lateral conductivity.

4. Conclusion

We obtained high quality AlN layers having rms surface roughness of 0.2 nm, FWHM of HRXRD for (002) and (114) reflections of 25 and 300 arcsec, respectively. This excellent quality is further confirmed by low temperature CL spectra with a FWHM of the donor bound exciton peak of 10 meV. We found that the surface and the crystal quality is degraded by Si doping. HRXRD and low temperature CL measurements show increasing in-plane tensile stress up to Si concentrations of approx. $2 \cdot 10^{19}\,\mathrm{cm^{-3}}$. From low temperature CL measurements, we observe that the intensity ratio between the deep level transition at 3 eV and near-band-edge luminescence is changing with [Si] and it is minimum for the sample having [Si] of $1.5 \cdot 10^{18}\,\mathrm{cm^{-3}}$. This sample shows a fair n-type conductivity at room temperature: electron carrier concentration of $4 \cdot 10^{14}\,\mathrm{cm^{-3}}$, carrier mobility of $30\,\mathrm{cm^2V^{-1}s^{-1}}$, resistivity of $530\,\Omega\mathrm{cm}$, and activation energy of about 200 meV for increasing temperature.

5. Acknowledgement

I would like to thank G.M. Prinz, M. Schirra, M. Feneberg, K. Thonke, and R. Sauer of the Institute of Semiconductor Physics for CL and Raman measurements; O. Klein, J. Biskupek and U. Kaiser of Central Facility of Electron Microscopy for TEM analysis; H. Yin, and P. Ziemann of Department of Solid State Physics for high temp. I–V measurements; L. Kirste, T. Fuchs, and M. Grimm of Fraunhofer–Institut für Angewandte Festkörperphysik, Freiburg and M. Trapp, P. Helm, and M. Gericke of RTG Mikroanalyse GmbH, Berlin for SIMS measurements; C. Kirchner of Mattson Thermal Products GmbH,

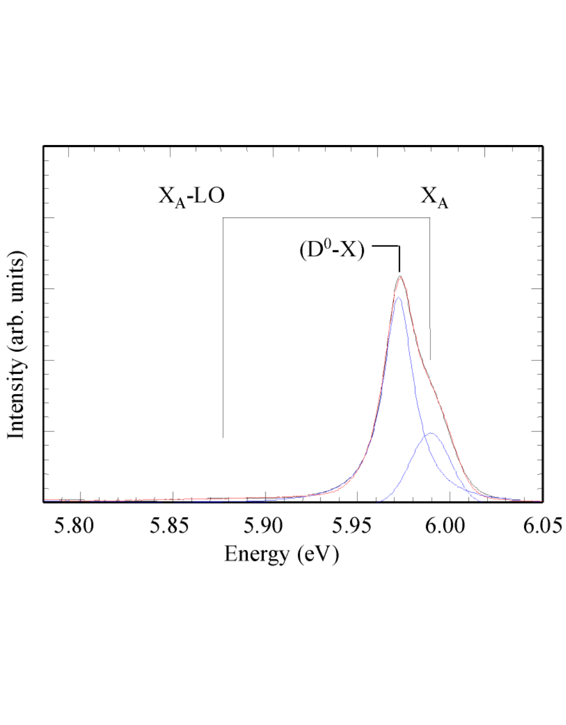

Fig. 3: Low temperature (10 K) CL spectra of a Si doped layer illustrating the FWHM of the CL peak approx. to be 20 meV (left). Overview of low temperature (10 K) CL spectra for the Si doped and the undoped samples (right). The peak at 3 eV increases in intensity for higher doped samples. The intensity ratio between the peaks at 3 eV and near band-edge luminescence is minimum for [Si] $1.5 \cdot 10^{18}\,\mathrm{cm}^{-3}$

Dornstadt for high temp. RTA; X. Lu for master thesis work; and R. Blood and R. Rösch for RIE. This work was financially supported by the Deutsche Forschungsgemeinschaft.

References

[1] Y. Taniyasu, M. Kasu, and T. Makimoto, "An aluminium nitride light-emitting diode with a wavelength of 210 nanometers", *Nature (London)*, vol. 441, no. 18, pp. 325–328, 2006.

[2] T.M. Katona, T. Margalith, C. Moe, M.C. Schmidt, C. Matt, S. Nakamura, J.S. Speck, S.P. DenBaars, and P. Steven, "Growth and fabrication of short-wavelength UV LEDs", in *Third International Conference on Solid State Lighting*, I.T. Ferguson, N. Narendran, S.P. DenBaars, J.C. Carano (Eds.), Proc. SPIE 5187, pp. 250–259, 2004.

[3] M. Shatalov, Z. Gong, M. Gaevski, S. Wu, W. Sun, V. Adivarahan, and M.A. Khan, "Reliability of AlGaN-based deep UV LEDs on sapphire", *Light-Emitting Diodes: Research, Manufacturing, and Applications*, K.P. Streubel, H.W. Yao, E.F. Schubert (Eds.), Proc. SPIE 6134, pp. 61340P-1–11, 2006.

[4] T. Ive, O. Brandt, H. Kostial, K.J. Friedland, L. Däweritz, and K.H. Ploog "Controlled n-type doping of AlN:Si films grown on 6H-SiC(0001) by plasma-assisted molecular beam epitaxy", *Appl. Phys. Lett.*, vol. 86, pp. 024106-1–3, 2005.

[5] B. Borisov, V. Kuryatkov, Yu. Kudryavtsev, R. Asomoza, S. Nikishin, D.Y. Song, M. Holtz, and H. Temkin, "Si–doped $Al_xGa_{1-x}N$ ($0.56 \leq x \leq 1$) layers grown by molecular beam epitaxy with ammonia", *Appl. Phys. Lett.*, vol. 87, pp. 132106-1–3, 2005.

[6] Y. Taniyasu, M. Kasu, and T. Makimoto, "Increased electron mobility in n–type Si–doped AlN by reducing dislocation density", *Appl. Phys. Lett.*, vol. 89, pp. 182112-1–3, 2006.

[7] Z. Y. Fan, J. Y. Lin, and H. X. Jiang, "Achieving conductive high Al-content AlGaN alloys for deep UV photonics", Proc. SPIE 6479, pp. 64791l-1–11, 2007.

[8] S.B. Thapa, "Structural and Spectroscopic Properties of AlN Layers Grown by MOVPE", *Annual Report 2005*, pp. 9–14. Ulm University, Institute of Optoelectronics.

[9] S.B. Thapa, "MOVPE Growth of High Quality AlN Layers and Effects of Si-doping", *Annual Report 2006*, pp. 95–102. Ulm University, Institute of Optoelectronics.

[10] L. Kirste, T. Fuchs, and M. Grimm; Fraunhofer–Institut für Angewandte Festkörperphysik, Freiburg, Samples Y1159, and Y1160.

[11] B. N. Pantha, R. Dahal, M. L. Nakarmi, N. Nepal, J. Li, J.Y. Lin, H. X. Jiang, Q. S. Paduano, and D. Weyburne "Correlation between optoelectronic and structural properties and epilayer thickness of AlN", *Appl. Phys. Lett.*, vol. 90, pp. 241101-1–3 (2007).

[12] G.M. Prinz, A. Ladenburger, M. Feneberg, M. Schirra, S.B. Thapa, M. Bickermann, B.M. Epelbaum, F. Scholz, K. Thonke, R. Sauer, "Photoluminescence, cathodoluminescence, and reflectance study of AlN layers and AlN single crystals," *Superlattices and Microstructures*, vol. 40, pp. 513–518 (2006).

[13] G.M Prinz, A. Ladenburger, M. Schirra, M. Feneberg, K. Thonke, R. Sauer, Y. Taniyasu, M. Kasu, and T. Makimoto,"Cathodoluminescence, photoluminescence, and reflectance of an aluminum nitride layer grown on silicon carbide substrate," *J. Appl. Phys.*, vol. 101, pp. 023511-1–5 (2007).

[14] T. Mattila and R.M. Nieminen, "Point-defect complexes and broadband luminescence in GaN and AlN," *Phys. Rev. B*, vol. 55, pp. 9571–9576 (1997).

Optically-Pumped Semicoductor Disk Lasers with Intracavity Second-Harmonic Generation

Frank Demaria and Alexander Kern

In this contribution, we present experimental results of our research on frequency-doubled semiconductor lasers emitting in the visible spectral range. These lasers include a laser-diode pumped semiconductor laser chip in an extended resonator configuration with a critically phase-matched lithium triborate crystal. The use of a single-plate Lyot filter within the cavity leads to single-peak emission with a bandwith of 1 nm at a 20 dB clip-level. The achieved second-harmonic power emission of 407 mW at a wavelength of 485 nm is still limited by the incident pump power.

1. Introduction

Second harmonic generation (SHG) drastically expands the spectral range that can be accessed by semiconductor lasers. For most visible wavelengths, the optical output powers and similarly the luminous fluxes exceed the values which can be achieved by semiconductor lasers directly, provided they exist at all. Hence, the utilization of this technique enables suitable light sources for projection displays. Multi-Watt optical output powers in the yellow-orange [1], green [2,3], and blue [4] spectral range have already been published by different research groups.

Although electrically-pumped surface emitting lasers with extended cavity may be considered as the more straightforward approach for intracavity frequency doubling [6], a few drawbacks arise with that. Unlike optically pumped structures, even the best luminous fluxes that have been demonstrated with intracavity frequency-doubling of laser diodes do not exhibit a potential that is required in projection displays using single emitters for each color. This is due to some fundamental requirements which can poorly be fulfilled that way. In vertical emitting lasers, the only way to establish excitation in a volume which is necessary to provide gain for several watts of optical power emission is to pump an area with diameters of some hundreds of micrometers. For such large areas, high conversion efficiencies become crucial because otherwise, the reduced heat spreading in the immediate vicinity of the active area leads to a fatal temperature increase. Current injection goes ahead with ohmic losses, also homogeneous or Gaussian distributed carrier injection over the required large areas is not possible. Although elaborated doping techniques like modulation doping are used, an optical absorption which is at least one order of magnitude higher is inevitably introduced. On the other hand, optical pumping allows homogeneous carrier generation in large areas without any ohmic losses and the absence of any intentional doping in optically pumped structures leads to low optical absorption losses and much higher outcoupling efficiencies. For these reasons it is possible to achieve optical output powers of more than 13 W, where the emitted power significantly exceeds the dissipated power in the structure [11].

2. Experimental Setup and Results

2.1 Experimental setup for intracavity second-harmonic generation

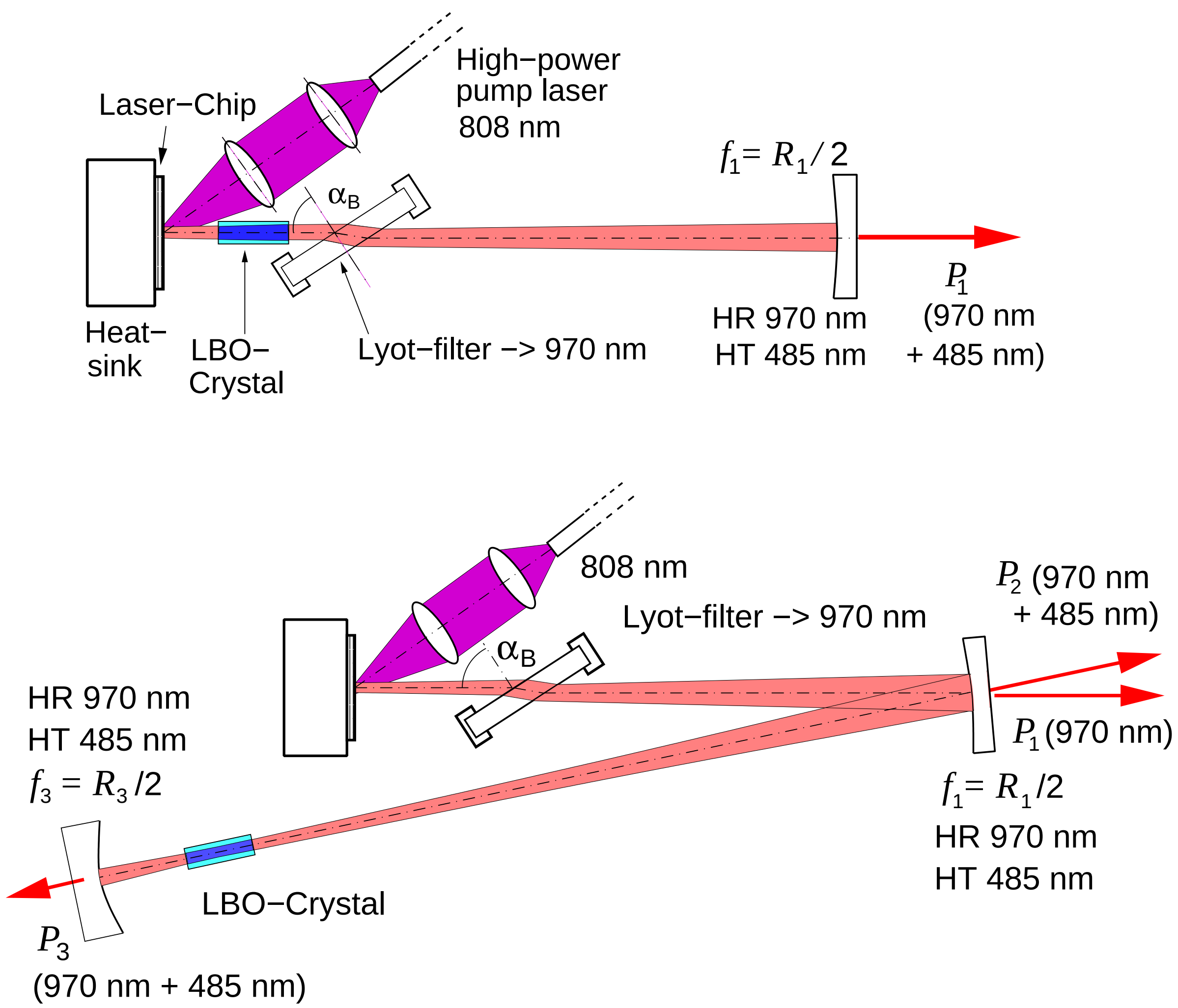

Fig. 1: Setup for intracavity second-harmonic generation with a hemispherical resonator (top) and a folded resonator (bottom).

Figure 1 is a schematic representation of the experimental setups. A simple hemispherical and a single-folded resonator configuration are used. The semiconductor laser chip is designed and fabricated for a pumping wavelength of 808 nm and an emission wavelength of 970 nm. It includes six strain compensated $In_{0.15}Ga_{0.85}As$ quantum wells and a double-band Bragg mirror [12]. The chip is mounted on a copper heat sink whose temperature is stabilized at a value of 0 °C by a Peltier cooler. Optical pumping is realized by a fiber-coupled diode laser. The collimated output from a fiber with 200 μm core-diameter is focused by a 6 mm-diameter plano-convex lens with 12 mm focal length what results in a pump-spot diameter of approximately 110 μm. The inclination angle is 25 ° with respect to the surface normal.

Second harmonic generation is achieved by a 8 mm-long, 3 ×3 mm^2 cross-section lithium triborate crystal (LiB_3O_5, LBO) in a critically phase-matched configuration. The walk-off angle is 0.6 ° and the spectral acceptance 1 nm · cm. Spectral stability and small-banded single-peak emission is provided by a 2 mm-thick single-plate Lyot filter. The functionality of birefringent filters and their application in intracavity second-harmonic generation setups is extensively described in literature [7–10]. Here the most simple form consists of a plane-parallel plate made out of positive uniaxial crystal quartz with its optical axis parallel to the surface. The surface is oriented under the Brewster angle of approximately 57 °, hence TE-polarized radiation will partially be reflected. Accordingly, stimulated emission with that polarization is suppressed, whereas simultaneously the gain contribution to TM-polarization is strengthened. That way, a stable polarization is established, which is essential for efficient and stable critically phase-matched frequency doubling. Inside the quartz crystal, the radiation splits of into an ordinary and an extraordinary beam. The refractive index for the extraordinary beam is determined by the angle between the optical axis and the direction of polarization, which can be tuned by axial rotation of the filter. Thus, the phase shift between the ordinary and extraordinary beam is adjustable and simultaneously the resonance wavelength. In other words, the quartz plate acts as a tunable frequency filter.

2.2 Spectral behavior

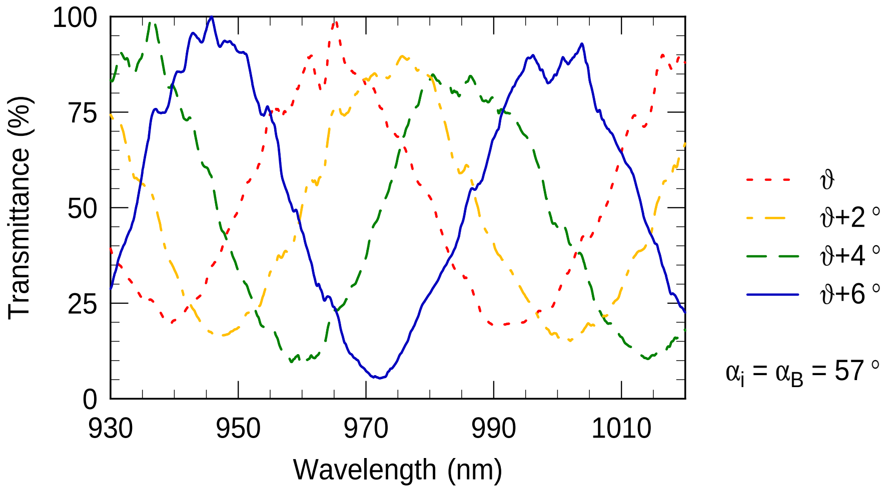

Fig. 2: Transmission spectra of a 2 mm-thick Lyot filter for an incident angle α_i of 57 ° (Brewster angle α_B). For the different spectra, the filter has been turned along its axial direction with a step size of 2 ° in the angle θ.

Figure 2 shows the measured transmission spectra of the 2 mm-thick Lyot filter. In this measurement, it is located between two polarizers under the Brewster angle of 57° and transmitted by light from a thermal light source. Turning the filter along its axial direction results in a spectral shift of approximately 5.8 nm per angle-degree. The filter reveals a free spectral range of 52 nm between the transmission maxima. This is sufficient to assure single peak emission under all circumstances. This is not the case for a 4 mm-thick Lyot filter, as for certain pump intensities and angular orientations two discrete peaks with a distance of 25 nm can be observed.

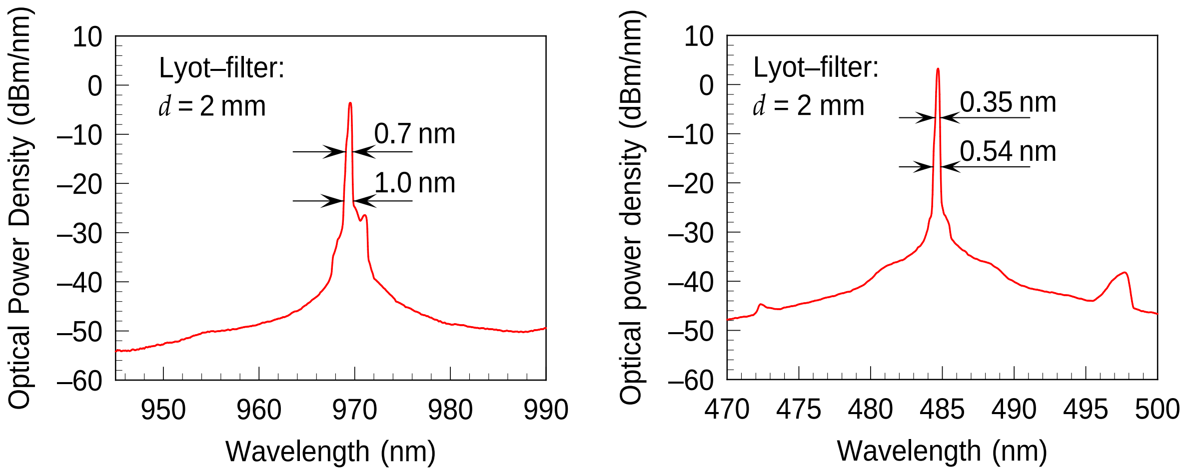

Fig. 3: Emission spectra from a laser configuration with a 2 mm-thick intra-cavity Lyot filter according to the top representation of Fig. 1. The left spectrum of fundamental emission reveals a width of 0.70 nm and 1.0 nm at a 10 dB and 20 dB-clip level. For the second harmonic spectrum on the left, the spectral widths are halved, together with the wavelength, so the relative width remains nearly unchanged.

In Fig. 3, the emission spectra from a linear resonator setup according to the top representation of Fig. 1 are shown. The spectrum of fundamental emission reveals a width of 0.70 nm at a 10 dB clip level and 1.0 nm at a 20 dB clip level. In the spectrum of the second harmonic, the relative width remains unchanged.

2.3 Output characteristics with a simple hemispherical resonator

In the single hemispherical resonator, an external mirror with 0.08 % transmittivity and a focal length of 50 mm is utilized. The resonator length is 92 mm. The output characteristics for the second harmonic and the fundamental optical output power is shown in Fig. 4. The spectral contribution to the output power is observed by the application of band-edge filters. The fundamental output power is also measured after removal of the LBO crystal. At an absorbed optical pump power of 7.5 W, the measurement was stopped to avoid the risk of a damage of the laser chip and to preserve it for further measurements. At this value, a second-harmonic optical output power of 260 mW is emitted, which corresponds to a conversion efficiency of 3.5 %. For each measurement point the LBO-crystal had to be re-adjusted. For discrete measurement points also the diffraction number M^2 of the second harmonic and also the fundamental emission is measured. Generally, the beam quality of the second harmonic exceeds the fundamental emission. This is because the

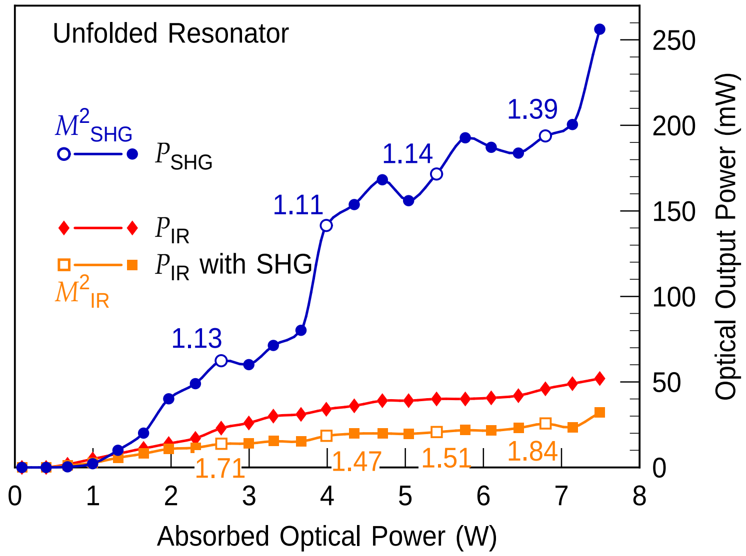

Fig. 4: Second harmonic optical output power and fundamental optical output power with and without SHG crystal. The 92 mm-long resonator with a single external mirror of 50 mm focal length and a transmittivity of 0.08 % includes a 2 mm-thick Lyot filter and a 8 mm-long LBO crystal. For individual measurement points the diffraction numbers M^2 which have also been determined are plotted.

fundamental TEM_{00}-mode and low order modes contribute more to the second harmonic generation due to their higher radiance.

2.4 Output characteristics with a folded resonator

All setups with a single folded resonator include a folding mirror with a focal length of $f_1 = 50$ mm and a transmittivity of 0.08 % at 970 nm. The chip-sided leg has a length of $L_1 \approx 91$ mm. The different end-mirrors with focal lengths of 15 mm and 50 mm have approximately a similar transmission characteristics as the folding mirror. Optical power emission is given by the sum of the different output powers P_1, P_2 and P_3, which refer to emission directions labeled in Fig. 1. In a more application-oriented setup, an end mirror with a high reflectivity for the second harmonic is recommended to assure that the second harmonic emission is predominantly coupled out of the folding mirror. In this case, the overall optical emission is approximately given by P_2. For each measurement point, the orientation of the LBO-crystal was adjusted.

The upper diagram of Fig. 5 refers to a 15 mm focal-length end mirror. A second harmonic output power of 220 mW and a conversion efficiency of 2.6 % is achieved at a maximum pump power of 8.3 W. The lower diagram of Fig. 5 refers to a 50 mm focal-length end mirror. There, at 6.8 W of absorbed optical power, a second harmonic power of 240 mW and a conversion efficiency of 3.5 % is achieved. At high pump powers, the slope of the second harmonic is increasing significantly. Comparison of the measured beam-quality shows that for the given pump-spot size, much better values are achieved for the resonator

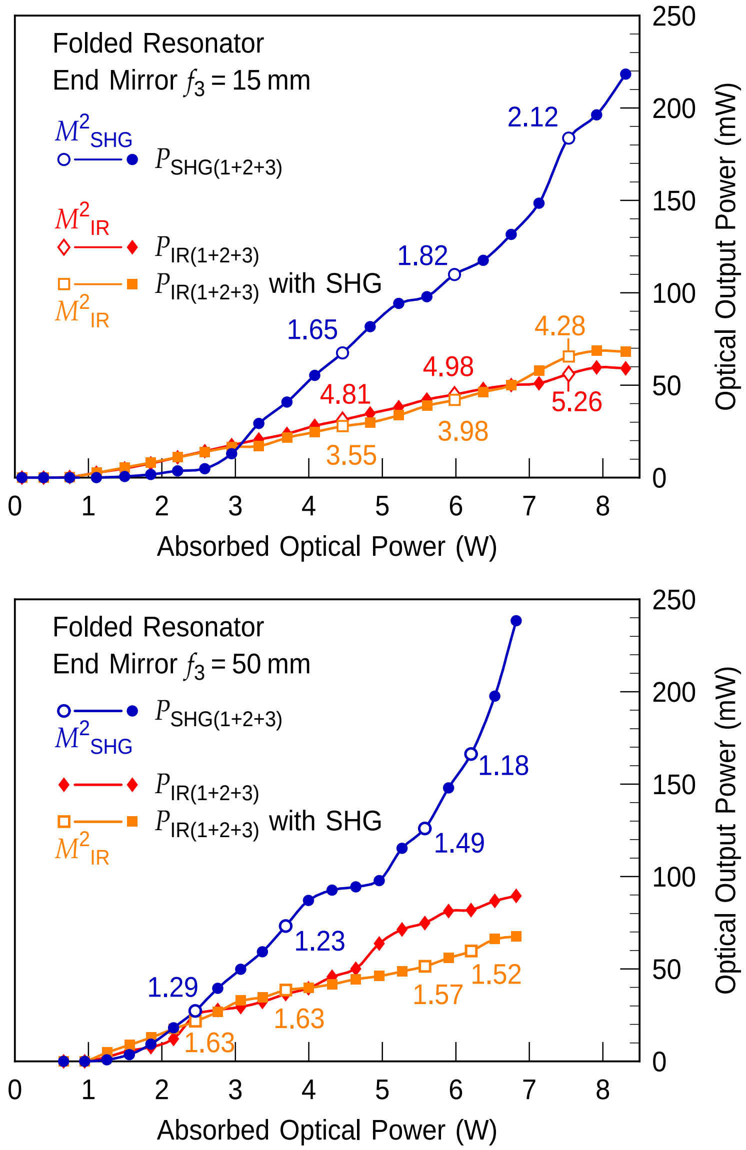

Fig. 5: Output characteristics of the second harmonic and the fundamental emission which is detected with and without the crystal. The upper diagram is based on a end-mirror with 15 mm focal length, in the lower diagram the end mirrors focal length is 50 mm.

geometry with the longer focal length. This is consistend with theoretical predictions [13].

With the described configuration, containing an end-mirror with 50 mm focal-length, an even better performance has been achieved in an independent measurement which is shown in Fig. 6. A maximum SHG output power of 407 mW is achieved, which was measured by the emission from the folded leg $P_2 + P_3$ at a pump power of 8.3 W. This results in a conversion efficiency of 4.9 %.

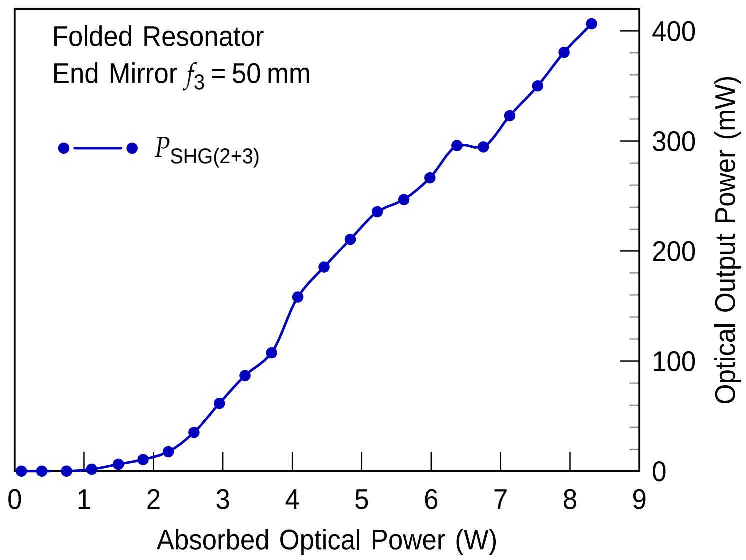

Fig. 6: Second harmonic output characteristics from a single folded resonator configuration. The emitted second harmonic output power $P_2 + P_3$ is 407 mW at an absorbed pump power of 8.3 W what results in a conversion efficiency of 4.9 %.

3. Conclusion and Outlook

We have demonstrated the capability to generate second harmonic output powers of several hundreds of milliwatts from semiconductor disk lasers which have been fabricated by our group. The optical output power was only limited by the applied pumping power. In the spectrum of the second harmonic, the relative spectral width of the fundamental emission peak remains nearly unchanged within a 20 dB level which indicates, that the SHG conversion efficiency is barely limited by the spectral width. Although on a laboratory scale, the setup size appears quite large, a reduction to much shorter dimensions is practicable. This can be done by applying a free-space pump scheme and a short cavity configuration with a nevertheless large mode volume within the gain medium [5]. Thus the described approach is particularly suitable for pocket-size projector displays and so called "pico projector displays".

References

[1] S. Hilbich, W. Seelert, V. Ostroumov, C. Kannengiesser, R. von Elm, J. Mueller, E. Weiss, H. Zhou, and J. Chilla, "New wavelengths in the yellow orange range between 545 nm to 580 nm generated by an intracavity frequency doubled optically pumped semiconductor laser," *Proc. SPIE*, vol. 6451, no. 64510C, 2007.

[2] S. Cho, G.B. Kim, J.-Y. Kim, K.-S. Kim, S.-M. Lee, J. Yoo, T. Kim, and Y. Park, "Compact and efficient green VECSEL based on novel optical end-pumping scheme," *IEEE Photon. Technol. Lett.*, vol. 19, no. 17, pp. 1325–1327, 2007.

[3] L. E. Hunziker, Q. Z. Shu, D. Bauer, C. Ilhi, G. J. Mahnke, M. Rebut, J. R. Chilla, A. L. Caphara, H. Zhu, E. S. Weiss, and M. K. Reed, "Power-scaling of optically-pumped semiconductor lasers," *Proc. SPIE*, vol. 6451, no. 64510A, pp. 1–6, 2007.

[4] G. Bum Kim, J.-Y. Kim, J. Lee, J. Yoo, K.-S. Kim, S.-M. Lee, S. Cho, S.-J. Lim, T. Kim, and Y. Park, "End-pumped green and blue vertical external cavity surface emitting laser devices," *Appl. Phys. Lett.*, vol. 89, no. 18, 181106, 2006.

[5] M. Schulze and A. Masters, "Optically pumped semiconductor lasers expand the scope of potential applications," *Laser Focus World*, vol. 42, no. 21, pp. 77–80, 2006.

[6] E.U. Rafailov, W. Sibbett, A. Mooradian, J.G. McInerney, H. Karlsson, S. Wang, and F. Laurell, "Efficient frequency doubling of a vertical-extended-cavity surface-emitting laser diode by use of a periodically poled KTP crystal," *Opt. Lett.*, vol. 28, no. 21, pp. 2091–2093, 2003.

[7] J.W. Evans, "The birefringent filter," *J. Opt. Soc. Am.*, vol. 39, no. 3, p. 229, 1949.

[8] M. Jacquemet, M. Domenech, G. Lucas-Leclin, P. Georges, J. Dion, M. Strassner, I. Sagnes, and A. Garnache, "Single-frequency cw vertical external cavity surface emitting semiconductor laser at 1003 nm and 501 nm by intracavity frequency doubling," *Appl. Phys. B*, vol. 86, pp. 503–510, 2007.

[9] R. Hartke, E. Heumann, G. Huber, M. Kühnelt, and U. Steegmüller, "Efficient green generation by intracavity frequency doubling of an optically pumped semiconductor disk laser," *Appl. Phys. B*, vol. 87, pp. 95–99, 2007.

[10] J. Lee, S.-M. Lee, T. Kim, and Y. Park, "7 W high-efficiency continuous-wave green light generation by intracavity frequency doubling of an end-pumped vertical external-cavity surface emitting semiconductor laser," *Appl. Phys. Lett.*, vol. 89, no. 241107, 2006.

[11] F. Demaria and M. Riedl, "High-radiance optically pumped semiconductor disk lasers," *Annual Report 2006, Institute of Optoelectronics, Ulm University*, pp. 3–9.

[12] E. Gerster, I. Ecker, S. Lorch, C. Hahn, S. Menzel, and P. Unger, "Orange-emitting frequency-doubled GaAsSb/GaAs semiconductor disk laser," *J. Appl. Phys.*, vol. 94, no. 12, pp. 7397–7401, 2003.

[13] F. Demaria, *Schicht- und Resonatordesign von Halbleiterscheibenlasern*. Ph.D. Thesis, Ulm University, 2008.

Ph.D. Theses

1. Tony Albrecht,
   Optisch gepumpte Halbleiter–Scheibenlaser
   mit monolitisch integriertem Pumplaser,
   January 2007.

2. Philipp Hennig Gerlach,
   Monolithisch integrierte absorptionsmodulierte
   Laserdioden mit Metallgittern,
   January 2007.

3. Michael Furitsch,
   Untersuchung von Degradationsmechanismen
   an (Al/In)GaN-basierenden Laserdioden,
   July 2007.

4. Johannes Michael Ostermann,
   Diffractive Optics for Polarization Control
   of Vertical-Cavity Surface-Emitting Lasers,
   July 2007.

Diploma and Master Theses

1. Gao Chong,
   Transport Properties in AlGaN/GaN Heterostructures,
   Master Thesis, February 2007.

2. Evangelos Angelopoulos,
   Heteroepitaxial Growth of GaN on ZnO by MOVPE,
   Master Thesis, May 2007.

3. Xu Hongcheng,
   Investigations of RIE Processing for the Controlled Characterization of Optoelectronic Properties of Nitride Based Devices,
   Master Thesis, July 2007.

4. Carolin Schneck,
   Optische Manipulation von Partikeln in mikrofluidischen Kanälen mit Hilfe VCSEL-basierter optischer Pinzetten,
   Diploma Thesis, September 2007.

5. Lu Xianming,
   The Studies of AlN/AlGaN Heterostructure Grown by MOVPE,
   Master Thesis, November 2007.

6. Christoph Przeszlakowski,
   Experimentelle Untersuchung von Resonatorkonfigurationen eines optisch gepumpten Halbleiterscheibenlasers zur Frequenzverdopplung,
   Diploma Thesis, November 2007.

7. Wenjie Hu,
   Optimization of Reactive Ion Etching Processes for GaAs and Si,
   Master Thesis, October 2007.

8. Wolfgang Tress,
   Elektrische Modellierung organischer Solarzellen,
   Diploma Thesis, November 2007.

9. Alexander Kern,
   Optimierung der Frequenzverdopplung an optisch gepumpten Halbleiter-Scheibenlasern,
   Diploma Thesis, December 2007.

10. Shunyi Li,
    MBE Growth and Structural Characterization of Optically Active Semiconductors and Laser Devices,
    Master Thesis, December 2007.

Semester Projects

1. Markus Schmid,
   Erstellung einer Heizungsregelung für Lebensdauertests von Vertikallaserdioden,
   January 2007.

2. Jochen Scharpf,
   Erweiterte dynamische Charakterisierung von Metall-Halbleiter-Metall (MSM)-Photodioden und Untersuchung ihres Datenübertragungsverhaltens unter Verwendung eines Transimpedanzverstärkers,
   February 2007.

3. Christian Schirling,
   Vergleich und Optimierung unterschiedlicher Ansteuerschemata für cholesterische Flüssigkristalldisplays,
   August 2007.

4. Dieter Rimpf,
   Prozessierung und Charakterisierung neuer Generationen monolithisch integrierter Transceiver-Chips,
   August 2007.

5. Daniel Steffen Setz,
   Untersuchungen zur Frequenzverdopplung eines optisch gepumpten Halbleiterscheibenlasers,
   September 2007.

6. Anna Bergmann,
   Untersuchungen an Vertikallaserdioden mit optimierter Schichtstruktur,
   September 2007.

7. Alexander Hein,
   Optisch-spektroskopische Charakterisierung von optisch gepumpten Halbleiter-Scheibenlasern,
   October 2007.

8. Frank Hesmer,
   Entwicklung eines Prozesses zur zuverlässigen Bedrahtung von oberseitig emittierenden Vertikallaserdioden,
   October 2007.

Talks and Conference Contributions

[1] K.J. Ebeling and R. Michalzik, "VCSEL research at Ulm revisited", *International Symposium on VCSELs and Integrated Photonics — Celebrating the 30th Anniversary of VCSEL*. Tokyo, Japan, Dec. 2007.

[2] J. Hertkorn, P. Brückner, S. B. Thapa, T. Wunderer, F. Scholz, M. Feneberg, K. Thonke, R. Sauer, M. Beer, and J. Zweck, "Optimization of nucleation and buffer layer growth for improved GaN quality and device performance", poster at *12th European Workshop on MOVPE*, Bratislava, Slovakia, June 2007.

[3] J. Hertkorn, P. Brückner, C. Gao, and F. Scholz, "Transport properties in n-type AlGaN/AlN/GaN-superlattices", poster at *7th Int. Conf. on Nitride Semiconductors*, Las Vegas, Nevada, USA, Sept. 2007.

[4] J. Hertkorn, "Modulation doped AlGaN/(AlN)/GaN heterostructures for high brightness LEDs", New Jersey Institute of Technology, Newark, NJ, USA, Oct. 2007.

[5] J. Hertkorn, "Modulation doped n- and p-type AlGaN/(AlN)/GaN heterostructures for improved current spreading in high power LEDs", *Söllerhaus-Seminar*, Riezlern, Austria, Oct. 2007.

[6] J. Hertkorn, "Modulation doped AlGaN/(AlN)/GaN heterostructures for high brightness LEDs", Seminar *"Neue Materialien"*, Universitt Magdeburg, Nov. 2007.

[7] A. Kroner, F. Rinaldi, R. Rösch, and R. Michalzik, "Densely packed VCSEL arrays tailored for optical particle manipulation", *Conf. on Lasers and Electro-Optics Europe, CLEO/Europe 2007*, paper CB4-1-TUE. Munich, Germany, June 2007.

[8] F. Lipski, "Freestanding GaN by HVPE", *Söllerhaus-Seminar*, Riezlern, Austria, Oct. 2007.

[9] F. Lipski, P. Brückner, and F. Scholz, "Si-Dotierung von GaN-Schichten bei der Hydrid-Gasphasen-Epitaxie", *DGKK-Workshop III-V-Epitaxie*, Marburg, Germany, Dec. 2007.

[10] R. Michalzik, "Vertical-cavity surface-emitting lasers for optical interconnection" (in German), *Electrical Engineering Colloquium*, Ulm University, Faculty of Engineering and Computer Sciences, Ulm, Germany, July 2007.

[11] R. Michalzik, M. Stach, F. Rinaldi, and S. Lorch, "Novel VCSEL-based transceiver chips for bidirectional optical interconnects using butt-coupled multimode fibers", in Proc. 5. ITG-Workshop *Photonische Aufbau- und Verbindungstechnik*, pp. 33–37. Berlin, Germany, Mar. 2007.

[12] R. Michalzik, M. Stach, F. Rinaldi, and S. Lorch, "Monolithic integration of VCSELs and MSM photodiodes for bidirectional multimode fiber communications" (invited), *SPIE Photonics West 2007*, Conf. on *Vertical-Cavity Surface-Emitting Lasers XI*. San Jose, CA, USA, Jan. 2007.

[13] J.M. Ostermann, P. Debernardi, and R. Michalzik, "Polarization stability of surface grating VCSELs under strong optical feedback", *Conf. on Lasers and Electro-Optics Europe, CLEO/Europe 2007*, paper CB7-1-WED. Munich, Germany, June 2007.

[14] F. Rinaldi and D. Wahl, "MBE technology II", *Söllerhaus-Seminar*, Riezlern, Austria, Oct. 2007.

[15] F. Rinaldi, S. Li, S. Menzel, and D. Wahl, "Characterization of MBE grown VCSELs", *Deutscher MBE Workshop 2007*, Jülich, Germany, Oct. 2007.

[16] H. Roscher, F. Rinaldi, A. Weigl, and R. Michalzik, "Record-low thermal resistance, 12.5 Gbit/s capable flip-chip bonded 850 nm wavelength 2-D VCSEL arrays", *Conf. on Lasers and Electro-Optics Europe, CLEO/Europe 2007*, paper CB4-4-TUE. Munich, Germany, June 2007.

[17] S. Schwaiger, "Influence of strain on magnetic anisotropy in GaMnAs", *Söllerhaus-Seminar*, Riezlern, Austria, Oct. 2007.

[18] F. Scholz, "LEDs: Basic concepts and state of the art", Lumitronix, Hechingen, Germany, Apr. 2007.

[19] F. Scholz, S. B. Thapa, and E. Angelopoulos, "Heteroepitaxial growth of GaN on ZnO by MOVPE", *Söllerhaus-Seminar*, Riezlern, Austria, Oct. 2007.

[20] W. Schwarz, "Approaches for vertical extended cavity lasers", *Söllerhaus-Seminar*, Riezlern, Austria, Oct. 2007.

[21] M. Stach, F. Rinaldi, J. Scharpf, S. Lorch, and R. Michalzik, "1 Gbit/s bidirectional optical data transmission over 50 m semi-GI PCS fiber with monolithically integrated transceiver chips", *EOS Conf. on Trends in Optoelectronics, Sub-conf. on Information and Communication*. Munich, Germany, June 2007.

[22] M. Stach, F. Rinaldi, D. Wahl, D. Rimpf, S. Lorch, and R. Michalzik, "1 Gbit/s full-duplex bidirectional optical data transmission over 500 m of 50 μm-core graded-index multimode fiber with novel monolithically integrated transceiver chips", *33rd Europ. Conf. on Opt. Commun., ECOC 2007*. Berlin, Germany, Sept. 2007.

[23] M. Stach, F. Rinaldi, D. Wahl, D. Rimpf, S. Lorch, and R. Michalzik, "Monolithically integrated miniaturized transceiver chips for bidirectional graded-index fiber systems" (in German: "Monolithisch integrierte miniaturisierte Transceiver-Chips für bidirektionale Gradientenindexfaser-Systeme"), *14th ITG Symposium on Communication Cable Networks*, Köln, Germany, Dec. 2007.

[24] S.B. Thapa, and F. Scholz, "AlN Growth by MOVPE", *Georgia Tech Lorraine*, Metz, France, Feb. 2007.

[25] S.B. Thapa, J. Hertkorn, F. Scholz, G.M. Prinz, M. Feneberg, K. Thonke, and R. Sauer, "MOVPE Growth of High Quality AlN Layers and Effects of Si doping", poster at *12th European Workshop on MOVPE*, Bratislava, Slovakia, June 2007.

[26] S.B. Thapa, E. Angelopoulos, J. Hertkorn, F. Scholz, A. Reiser, K. Thonke, R. Sauer, H. Hochmuth, M. Lorenz, and M. Grundmann, "Heteroepitaxial Growth of GaN on ZnO by MOVPE" poster at *12th European Workshop on MOVPE*, Bratislava, Slovakia, June 2007.

[27] S.B. Thapa, F. Scholz, J. Hertkorn, G.M. Prinz, M. Feneberg, K. Thonke, and R. Sauer, "MOVPE Growth of High Quality AlN Layers and Effects of Si doping", *7th Int. Conf. on Nitride Semiconductors*, Las Vegas, Nevada, USA, Sept. 2007.

[28] S.B. Thapa, "MOVPE Growth of High Quality AlN Layers and Effects of Si doping", *Söllerhaus-Seminar*, Riezlern, Austria, Oct. 2007.

[29] D. Wahl and F. Rinaldi, "MBE technology I", *Söllerhaus-Seminar*, Riezlern, Austria, Oct. 2007.

[30] T. Wunderer, F. Lipski, J. Hertkorn, P. Brückner, F. Scholz, M. Feneberg, M. Schirra, K. Thonke, A. Chuvilin, and U. Kaiser, "Bluish-green semipolar GaInN/GaN light emitting diode on $\{1\bar{1}01\}$ GaN side facets", poster at *7th Int. Conf. on Nitride Semiconductors*, Las Vegas, Nevada, USA, Sept. 2007.

[31] T. Wunderer, "Steps to the green LED", *Söllerhaus-Seminar*, Riezlern, Austria, Oct. 2007.

[32] T. Wunderer, "High-brightness GaN-based light emitting diodes", Physical Institute at Lomonosov Moscow State University, Moscow, Russia, Nov. 2007.

[33] T. Wunderer, F. Lipski, J. Hertkorn, P. Brückner, F. Scholz, M. Feneberg, M. Schirra, K. Thonke, A. Chuvilin, U. Kaiser, I. Knoke, and E. Meissner, "Blau-grüne semipolare GaInN/GaN LEDs auf $\{1\bar{1}01\}$ GaN-Seitenfacetten", *DGKK-Workshop III-V-Epitaxie*, Marburg, Germany, Dec. 2007.

[34] M.V. Klymenko, I.M. Safonov, O.V. Shulika, I.A. Sukhoivanov, and R. Michalzik, "Effective-mass superlattice as an injector in quantum cascade lasers", *International Workshop on PHysics & Applications of SEmiconductor Lasers, PHASE 2007*. Supélec, Campus de Metz, Metz, France, March 2007.

[35] B. Scherer, J. Wöllenstein, M. Weidemüller, W. Salzmann, J.M. Ostermann, F. Rinaldi, and R. Michalzik, "Oxygen measurements at high pressures using a low cost, polarization stabilized, widely tunable vertical-cavity surface-emitting laser", *SPIE Europe, Microtechnologies for the New Millennium*, Conf. on *Smart Sensors, Actuators and MEMS III*. Maspalomas, Gran Canaria, Spain, May 2007.

Publications

[1] K.J. Ebeling and R. Michalzik, "VCSEL research at Ulm revisited", in Digest *International Symposium on VCSELs and Integrated Photonics — Celebrating the 30th Anniversary of VCSEL*, pp. 16–18. Tokyo, Japan, Dec. 2007.

[2] J. Hertkorn, P. Brückner, S.B. Thapa, T. Wunderer, F. Scholz, M. Feneberg, K. Thonke, R. Sauer, M. Beer, and J. Zweck, "Optimitazion of nucleation and buffer layer growth for improved GaN quality", *J. Crystal Growth*, vol. 308, pp. 30–36, 2007.

[3] J. Hertkorn, P. Brückner, S.B. Thapa, T. Wunderer, F. Scholz, M. Feneberg, K. Thonke, R. Sauer, M. Beer, and J. Zweck, "Optimization of Nucleation and Buffer Layer Growth for improved GaN Quality and Device Performance", in Proc. *12^{th} European Workshop on MOVPE*, pp. 33–36. Bratislava, Slovakia, 2007.

[4] A. Kroner, F. Rinaldi, R. Rösch, and R. Michalzik, "Densely packed VCSEL arrays tailored for optical particle manipulation", in Proc. (CD ROM) *Conf. on Lasers and Electro-Optics Europe, CLEO/Europe 2007*, paper CB4-1-TUE, one page. Munich, Germany, June 2007.

[5] A. Kroner, F. Rinaldi, J.M. Ostermann, and R. Michalzik, "High-performance single fundamental mode AlGaAs VCSELs with mode-selective mirror reflectivities", *Optics Communications*, vol. 270, pp. 332–335, 2007.

[6] R. Michalzik, M. Stach, F. Rinaldi, and S. Lorch, "Novel VCSEL-based transceiver chips for bidirectional optical interconnects using butt-coupled multimode fibers", in Proc. 5. *ITG-Workshop Photonische Aufbau- und Verbindungstechnik*, pp. 33–37. Berlin, Germany, March 2007.

[7] R. Michalzik, M. Stach, F. Rinaldi, and S. Lorch, "Monolithic integration of VCSELs and MSM photodiodes for bidirectional multimode fiber communications" (invited), in *Vertical-Cavity Surface-Emitting Lasers XI*, K.D. Choquette, J.K. Guenter (Eds.), Proc. SPIE 6484, pp. 648409-1–10, 2007.

[8] B. Neubert, T. Wunderer, P. Brückner, F. Scholz, M. Feneberg, F. Lipski, and K. Thonke, "Semipolar GaN/GaInN LEDs with more than 1mW optical output power", *J. Crystal Growth*, vol. 298, pp. 706–709, 2007.

[9] J.M. Ostermann, P. Debernardi, and R. Michalzik, "Polarization-controlled surface grating VCSELs under unpolarized and polarized optical feedback", *IEEE Photon. Technol. Lett.*, vol. 19, pp. 1359–1361, 2007.

[10] J.M. Ostermann, P. Debernardi, A. Kroner, and R. Michalzik, "Polarization-controlled surface grating VCSELs under externally induced anisotropic strain", *IEEE Photon. Technol. Lett.*, vol. 19, pp. 1301–1303, 2007.

[11] J.M. Ostermann, P. Debernardi, and R. Michalzik, "Polarization stability of surface grating VCSELs under strong optical feedback", in Proc. (CD ROM) *Conf. on Lasers and Electro-Optics Europe, CLEO/Europe 2007*, paper CB7-1-WED, one page. Munich, Germany, June 2007.

[12] F. Rinaldi, J.M. Ostermann, A. Kroner, and R. Michalzik, "High-performance AlGaAs-based VCSELs emitting in the 760 nm wavelength range", *Optics Communications*, vol. 270, pp. 310–313, 2007.

[13] H. Roscher, F. Rinaldi, and R. Michalzik, "Small-pitch flip-chip-bonded VCSEL arrays enabling transmitter redundancy and monitoring in 2-D 10-Gbit/s space-parallel fiber transmission", *IEEE J. Select. Topics Quantum Electron.*, vol. 13, pp. 1279–1289, 2007.

[14] H. Roscher, F. Rinaldi, A. Weigl, and R. Michalzik, "Record-low thermal resistance, 12.5 Gbit/s capable flip-chip bonded 850 nm wavelength 2-D VCSEL arrays", in Proc. (CD ROM) *Conf. on Lasers and Electro-Optics Europe, CLEO/Europe 2007*, paper CB4-4-TUE, one page. Munich, Germany, June 2007.

[15] M. Stach, F. Rinaldi, D. Wahl, D. Rimpf, S. Lorch, and R. Michalzik, "Monolithically integrated miniaturized transceiver chips for bidirectional graded-index fiber systems" (in German: "Monolithisch integrierte miniaturisierte Transceiver-Chips für bidirektionale Gradientenindexfaser-Systeme"), *14th ITG Symposium on Communication Cable Networks*, Köln, Germany, Dec. 2007. In *ITG-Fachbericht Kommunikationskabelnetze*, vol. 204, pp. 115–119, 2007.

[16] M. Stach, F. Rinaldi, D. Wahl, D. Rimpf, S. Lorch, and R. Michalzik, "1 Gbit/s full-duplex bidirectional optical data transmission over 500 m of 50 μm-core graded-index multimode fiber with novel monolithically integrated transceiver chips", in Proc. *33rd Europ. Conf. on Opt. Commun., ECOC 2007*, vol. 5, pp. 127–128. Berlin, Germany, Sept. 2007.

[17] M. Stach, F. Rinaldi, J. Scharpf, S. Lorch, and R. Michalzik, "1 Gbit/s bidirectional optical data transmission over 50 m semi-GI PCS fiber with monolithically integrated transceiver chips", in Proc. *EOS Conf. on Trends in Optoelectronics, Sub-conf. on Information and Communication*, pp. 61–62. Munich, Germany, June 2007.

[18] S.B. Thapa, C. Kirchner, F. Scholz, G.M. Prinz, K. Thonke, R. Sauer, A. Chuvilin, J. Biskupek, U. Kaiser, and D. Hofstetter, "Structural and spectroscopic properties of AlN layers grown by MOVPE", *J. Crystal Growth*, vol. 298, pp. 383–386, 2007.

[19] S.B. Thapa, J. Hertkorn, F. Scholz, G.M. Prinz, M. Feneberg, K. Thonke, and R. Sauer, "MOVPE growth of high quality AlN layers and effects of Si doping", in Proc. *12^{th} European Workshop on MOVPE*, pp. 65–68. Bratislava, Slovakia, June 2007.

[20] S.B. Thapa, E. Angelopoulos, J. Hertkorn, F. Scholz, A. Reiser, K. Thonke, R. Sauer, H. Hochmuth, M. Lorenz, and M. Grundmann, "Heteroepitaxial growth of GaN on ZnO by MOVPE", in Proc. *12^{th} European Workshop on MOVPE*, pp. 135–138. Bratislava, Slovakia, June 2007.

[21] T. Wunderer, P. Brückner, J. Hertkorn, F. Scholz, G. J. Beirne, M. Jetter, P. Michler, M. Feneberg, and K. Thonke, "Time and locally resolved photoluminescence of semipolar GaInN/GaN facet light emitting diodes", *Appl. Phys. Lett.*, vol. 90, pp. 171123-1–3 and *Virtual J. Ultrafast Science*, vol. 6, issue 5, 2007.

[22] S.-S. Beyertt, U. Brauch, F. Demaria, N. Dhidah, A. Giesen, T. Kübler, S. Lorch, F. Rinaldi, and P. Unger, "Efficient gallium-arsenide disk laser", *IEEE J. Quantum Electron.*, vol. 43, pp. 869–875, 2007.

[23] P. Debernardi, J.M. Ostermann, M. Sondermann, T. Ackemann, G.P. Bava, and R. Michalzik, "A theoretical-experimental study of the vectorial modal properties of polarization-stable multimode grating VCSELs", *IEEE J. Select. Topics Quantum Electron.*, vol. 13, pp. 1340–1348, 2007.

[24] M. Feneberg, F. Lipski, R. Sauer, K. Thonke, T. Wunderer, P. Brückner, and F. Scholz, "Piezoelectric fields in tilted GaInN quantum wells", in Proc. *MRS Fall Meeting* Boston Dec. 2007; Mat. Res. Symp. Proc., vol. 955, pp. 0955-I12-02-1–4, 2007.

[25] M. Feneberg, F. Lipski, R. Sauer, K. Thonke, P. Brückner, B. Neubert, T. Wunderer, and F. Scholz, "Polarized light emission from semipolar GaInN quantum wells on {1-101} GaN facets", *J. Appl. Phys.*, vol. 101, pp. 053530-1–6, 2007.

[26] C. Fuchs, T. Gensty, P. Debernardi, G.P. Bava, J.M. Ostermann, R. Michalzik, A. Haglund, A. Larsson, and W. Elsäßer, "Spatiotemporal turn-on dynamics of grating relief VCSELs", *IEEE J. Quantum Electron.*, vol. 43, pp. 1227–1234, 2007.

[27] L. Gu, V. Srot, W. Sigle, C. Koch, P. van Aken, F. Scholz, S.B. Thapa, C. Kirchner, M. Jetter, and M. Rühle, "Band gap measurements of direct and indirect semiconductors using monochromated electrons", *Phys. Rev.*, vol. B 75, pp. 195214-1–8, 2007.

[28] M.V. Klymenko, I.M. Safonov, O.V. Shulika, I.A. Sukhoivanov, and R. Michalzik, "Effective-mass superlattice as an injector in quantum cascade lasers", *Opt. Quantum Electron.*, vol. 39, 2007, in press. Electronic version: DOI 10.1007/s11082-007-9153-x.

[29] M.V. Klymenko, I.M. Safonov, O.V. Shulika, I.A. Sukhoivanov, and R. Michalzik, "Effective-mass superlattice as an injector in quantum cascade lasers", in Proc. *International Workshop on PHysics & Applications of SEmiconductor Lasers, PHASE 2007*, p. 31. Supélec, Campus de Metz, Metz, France, March 2007.

[30] B. Scherer, J. Wöllenstein, M. Weidemüller, W. Salzmann, J.M. Ostermann, F. Rinaldi, and R. Michalzik, "Oxygen measurements at high pressures using a low cost, polarization stabilized, widely tunable vertical-cavity surface-emitting laser", in *Smart Sensors, Actuators, and MEMS III*, T. Becker, C. Cané, N.S. Barker (Eds.), Proc. SPIE 6589, pp. 658908-1–10, 2007.

[31] Z.H. Wu, F.A. Ponce, J. Hertkorn, and F. Scholz, “Determination of the electronic band structure for a graded modulation-doped AlGaN/AlN/GaN superlattice”, *Appl. Phys. Lett.*, vol. 91, pp. 142121-1–3, 2007.

Ulm University | Institute of Optoelectronics | Annual Report 2007

ulm university universität ulm

Ulm University
Institute of Optoelectronics
Albert-Einstein-Allee 45
89081 Ulm | Germany